AHMAD HOSSEINIZADEH

Excited States in $U(1)_{2+1}$ Lattice Gauge Theory

and

Level Spacing Statistics in Classical Chaos

Thèse présentée
à la Faculté des études supérieures de l'Université Laval
dans le cadre du programme de doctorat en physique
pour l'obtention du grade de philosophiae doctor (Ph.D.)

DÉPARTEMENT DE PHYSIQUE, DE GÉNIE PHYSIQUE ET D'OPTIQUE
FACULTÉ DES SCIENCES ET DE GÉNIE
UNIVERSITÉ LAVAL
QUÉBEC

2010

Acknowledgements

I would like to give my special thanks and genuine regards to my supervisor, Professor Helmut Kröger, whose vital encouragements, valuable guidance and support have enabled me to develop an understanding of the subjects.

Also, I would like to express my hearty and sincere appreciations to the following people who have made the work on this thesis possible:

Azam and Arash for their virtual and online helps, and their patience of three years.

My honored friend Gurgen for his insightful discussions and opinions, and his brotherly assistances during the past four years.

Faculty members of the theoretical physics group, in particular Professors Pierre Amiot and Luc Marleau, for their great lectures throughout my graduate career, and also my additional thanks to Prof. Pierre Amiot, who did the pre-reading of my thesis along with his useful suggestions.

The director of our department, Prof. René Roy, and the former and the present presidents of graduate programs, Professors Ermano F. Borra and Louis J. Dubé, for their official collaborations in the period of my studies in the physics department of Laval University.

The staff of our department, particularly Mrs. Marjolaine McFadden, Diane Hallé, Diane Coté, Denise Dugas and Françoise Dubois, for their cooperations in all my official affairs.

Professor Guy Moore from the physics department of McGill University to participate in the arbitration of this thesis.

Finally, I offer my cordial regards and blessings to my family and my other friends, particularly Reza, Jean-François, Mehdi, Yousef and Abbass, for their help in any respect during my residing in Québec City.

To Azam, Arash, my parents and all my teachers with gratitude

Nature is an infinite sphere of which the center is everywhere and the circumference nowhere. Blaise Pascal (1623-1662)

Résumé

Cette thèse est organisé en deux parties. Dans la première partie nous nous adressons à un problème vieux dans la théorie de jauge – le calcul du spectre et des fonctions d'onde. La stratégie que nous proposons est de construire une base d'etats stochastiques de liens de Bargmann, construite à partir d'une distribution physique de densité de probabilité. Par la suite, nous calculons les amplitudes de transition entre ces états par une approche analytique, en utilisant des intégrales de chemin standards ainsi que la théorie des groupes. Également, nous calculons numériquement matrices symétrique et hermitienne des amplitudes de transition, via une méthode Monte Carlo avec *échantillonnage pondéré*. De chaque matrice, nous trouvons les valeurs propres et les vecteurs propres. En appliquant cette méthode á la théorie de jauge U(1) en deux dimensions spatiales, nous essayons d'extraire et de présenter le spectre et les fonctions d'onde de cette théorie pour des grilles de petite taille. En outre, nous essayons de faire quelques ajustement dynamique des fenêtres de spectres d'énergie et les fonctions d'onde. Ces fenêtres sont outiles de vérifier visuellement la validité de l'hamiltonien Monte Carlo, et de calculer observables physiques.

Dans la deuxième partie nous étudions le comportement chaotique de deux systèmes de billard classiques, par la théorie des matrices aléatoires. Nous considérons un gaz périodique de Lorentz à deux dimensions dans des régimes de horizon fini et horizon infini. Nous construisons quelques matrices de longueurs de trajectoires de un particule mobile dans ce système, et réalisons des études des spectres de ces matrices par l'analyse numérique. Par le calcul numérique des distributions d'espacement de niveaux et rigidité spectral, nous constatons la statistique des espacements de niveaux suggère un comportement universel. Nous étudions également un tel comportement pour un système optique chaotique. En tant que quasi-système de potentiel, ses fluctuations dans l'espacement de ses niveaux suivent aussi un comportement GOE, ce qui est une signature d'universalité. Dans cette partie nous étudions également les propriétés de diffusion du gaz de Lorentz, par la longueur des trajectoires. En calculant la variance de ce quantité, nous montrons que dans le cas d'horizons finis, la variance de longueurs est linéaire par rapport au nombre de collisions de la particule dans le billard. Cette linéarité permet de définir un coefficient de diffusion pour le gaz de Lorentz, et dans un schéma général, elle est compatible avec les résultats obtenus par d'autres méthodes.

Abstract

This thesis is organized into two parts. In the first part, we address an old problem in lattice gauge theory – the computation of spectrum and wave functions. The strategy which we propose is to construct a stochastic basis of Bargmann link states, drawn from a physical probability density distribution. At the next step, we calculate transition amplitudes between those states via an analytical approach, using standard path integrals as well as the group theoretical methods. We also numerically compute symmetric and Hermitian matrices of transition amplitudes, via the method of Monte Carlo with importance sampling. From each matrix, we find an effective Hamiltonian, as well as its eigenvalues and eigenvectors. By applying this method to U(1) lattice gauge theory in two spatial dimensions, we attempt to extract and present the spectrum and the wave functions of this theory for some small size lattices. In addition, we try to establish some scaling windows of energy spectra and wave functions. Such windows are a test of the validity of the Monte Carlo Hamiltonian, and the strategy to compute physical observables.

In the second part, we study the chaotic behavior of two classical billiard systems, using random matrix theory. We consider a two-dimensional periodic Lorentz gas in the finite-horizon and infinite-horizon regimes. By constructing some symmetric matrices from the lengths of trajectories of a moving-particle in this system, we perform a numerical analysis of the spectra of those matrices. Through computing the level spacing distributions and the spectral rigidities, we find that the level spacing statistics of the length matrices shows a universal behavior. We also investigate such a behavior for a chaotic optical system. As a quasi-potential system, its level spacing fluctuations also follow GOE-behavior, which is a signature of universality. In this part, we also study the diffusion properties of the Lorentz gas using the length of the particle's trajectory. By computing the variance of this quantity in terms of billiard ball rebound numbers, we show that the length variance behaves linearly in the case of finite-horizon. This linearity establishes a diffusion coefficient for the Lorentz gas. In a general scheme, the results are compatible with the other methods.

Contents

List of Tables

List of Figures

Preface

Part I Lattice gauge theory (LGT), invented by Wilson in 1974 [1], is the most powerful non-perturbative method for the study of gauge theories. In particular, it plays a fundamental role in our understanding of non-perturbative phenomena in QCD, such as the quark confinement[1] [2, 3].

There are two principle methods in LGT, namely the Lagrangian (Euclidean) approach formulated by Wilson and the Hamiltonian formalism introduced by Kogut and Susskind [4]. In the Lagrangian method, the dynamics of a lattice system is identified in terms of the action of the system in question. After the discretization of continuum space-time, the primary step is to do a Wick rotation from Minkowski to the Euclidean space (i.e., $t \rightarrow -it$) [5]. Then, all calculations are performed by means of the Euclidean metric. The Lagrangian technique is presently preferred by the lattice community and, indeed, most progresses in LGT have been achieved through this method. This approach allows one to simulate LGT as a statistical system using well known Monte Carlo techniques. To apply the methods of statistical mechanics, the field action is identified as the energy of a lattice configuration, and the vacuum functional integral becomes the partition function.

The Hamiltonian version of LGT, on the other hand, describes the matter and the gauge degrees of freedom on the spatial part of a (3+1)-dimensional lattice. In this alternative picture of LGT, only space is discretized but time is treated as a continuous variable. Here the theory is considered as a quantum system with many degrees of freedom. An appealing aspect of this approach is that it reduces LGT to a many-body problem. Therefore, a host of analytic techniques from nuclear and condensed matter physics as well as many-body theory, are applicable in this area of LGT.

Since the invention of LGT, it has been customary to compute the Euclidean 2-point correlation functions (and also the n-point correlation functions). It is the expectation value

[1] The quark confinement asserts that the quarks are confined in hadrons through a quark-antiquark potential, which linearly increases with the separation of $q\bar{q}$ pair.

of two field operators between the vacuum states $|\Omega, t = \pm\infty\rangle$, that is

$$\langle \Omega, t = +\infty | \, \Psi(x)\Psi(y) \, | \Omega, t = -\infty \rangle \, . \tag{1}$$

In fact, it should be noted that the ground state wave function Ω is not generally known in LGT. The ground state wave function enters in the above amplitude through the Feynman-Kac limit [2], via projection from an arbitrary state Ξ onto the vacuum state. This occurs in the limit of large Euclidean times. On the other words,

$$\exp[-\mathcal{H}t/\hbar] \, |\Xi\rangle \; \sim \; \lim_{t\to\infty} \exp[-E_0 t/\hbar] \, |\Omega\rangle \, \langle\Omega| \, |\Xi\rangle \; . \tag{2}$$

A physically interesting problem is the construction of the ground state wave function. The first point is that we need more information in addition to the vacuum-to-vacuum transition amplitude. This means that more states are required to be considered here. Let us start out by more general transition amplitudes between initial and final states, taken from a suitable chosen set of states $|\Upsilon_\nu\rangle$, $\nu = 1, 2, ..., N$, that is

$$\left\langle \Upsilon_\nu, t = T \right| \left. \Upsilon_\mu, t = 0 \right\rangle \; = \; \langle \Upsilon_\nu | \exp[-\mathcal{H}T/\hbar] \left| \Upsilon_\mu \right\rangle . \tag{3}$$

Here, the states $|\Upsilon_\nu\rangle$ stand for the time-independent Bargmann link states, i.e., a configuration of link variables U, assigned to any link ij on the whole "spatial" part of a lattice. As a reminder, in the case of massive particles coupled via oscillators, a Bargmann state denotes the ensemble of displacements of the particles from their resting positions. Hence Bargmann states are the analogue of position states in quantum mechanics.

At the second step, it is absolutely crucial to choose the "physical" states $|\Upsilon_\nu\rangle$. In quantum mechanics it is a convention to use basis states obeying mathematical properties, such as being orthogonal functions and forming a complete basis. Examples are Fourier's functions, Hermite functions, and so on. These functions have no relation to the particular physical system, e.g. a hydrogen atom. This is a luxury which one can afford when solving a system with a few degrees of freedom. However, in many-body physics and quantum field theory (with an infinite number of degrees of freedom) one should better choose a basis suited to the particular physical system.

It is an old tradition in many-body nuclear physics, condensed matter and elementary particle physics that one computes wave functions and energy eigenvalues from matrix elements of a Hamilton operator in a suitable basis. This approach has been successful in special cases, e.g., when perturbation theory is applicable (nuclear shell model, Kondo effect [7]), or in situations where a few degrees of freedom describe the physics (Schwinger model in

[2] In general, the time evolution of a quantum system is given by the behavior of $\exp\left[-\frac{\mathcal{H}T}{\hbar}\right]$, when $T \to \infty$ (T is the imaginary time). In the Feynman-Kac limit, one has: $\exp[-\mathcal{H}T/\hbar] \to \lim_{T\to\infty} |\psi_0\rangle \exp[-E_0 T/\hbar] \langle\psi_0|$, where E_0 and ψ_0 are the ground state energy and wave function [5, 6]

(1+1)-dimensions [8], renormalization group Hamiltonian for critical phenomena [7]). However, this method has not led to general remarkable successes. The problem is due to the choice of basis states. This can be understood by the example of the diagonalization of a real symmetric matrix of large but finite rank, which is ill-conditioned (large difference in order of magnitude between the largest and the smallest eigenvalues). Any set of orthogonal basis states yields a few leading order eigenvalues. However, only basis states close to the eigen basis resolve the eigenvalues beyond the leading order.

Considering this lesson in many-body physics and field theory, it is not surprising that perturbatively constructed basis states (e.g. Fock states) in general are not sufficient (i.e. those states do not reflect the physically important degrees of freedom). Besides this difficulty, there is another important question: does any controllable cut-off exist? In the Hamiltonian formulation of field theory, the standard way is to construct a Fock space, parameterized by some high momentum and occupation number cut-offs [9]. However, increasing these parameters causes an exponential growth in the density of states, then the system cannot be controlled. Accordingly, these cut-offs are not reliable. Therefore, the question is: what kind of cut-off is physically meaningful?

We suggest a solution to such problems through a combination of two strategies: (i) Use of stochastic techniques to sample states from a huge variety of possibilities. (ii) Employ physics to guide the sampling. These two principles lead one to do the Monte Carlo with importance sampling, which has been used for most computations of path integrals via generation of equilibrium path configurations, with successful results in LGT. The so-called stochastic basis states (or reduced basis states), discussed in chapter 3, will be related to those equilibrium path configurations. By computation of transition amplitudes between the stochastic basis states, we obtain the spectrum and the wave functions of an effective Hamiltonian - the so called Monte Carlo Hamiltonian (MCH) - valid in a low energy (low-temperature) window.

The idea of the MCH has been suggested by Kröger et al. in 1999 [10]. It has been demonstrated in a number of examples in quantum mechanics and scalar field theory. For the 1-D harmonic oscillator, energy spectrum, wave functions and thermodynamical functions have been found to be in agreement with the exact results [10, 11]. Similar results have been obtained for uncoupled as well as coupled harmonic oscillators in 2-D and 3-D [12, 13]. This has been extended to a variety of other potentials in 1-D such as $V \propto x^2 + x^4$, $V \propto |x|/2$, and $V \propto \theta(x)x$, as well as the $1/r$ Coulomb potential with a singularity at the origin [14, 15, 16]. In addition, the MCH has also been applied to the Yukawa potential $V = -V_0 \exp(-\alpha r)/r$, to search for a critical value of α_c where no bound states exist [17]. Furthermore, this technique has been also applied to the (1+1)-D Klein-Gordon model in field theory, for the computation of the spectrum and thermodynamical functions [18, 19, 20, 21].

The first step towards the MCH in LGT has been made in Ref. [22] by computing transition amplitudes for only one link state in U(1) LGT. In the first part of this thesis, we construct the MCH in U(1) LGT for two-dimensional lattices, and compute the energy spectrum of ground state, a number of excited states and the corresponding wave functions. We also compute the thermodynamical functions, such as the average energy and the specific heat. We generally proceed by the following steps:

Chapter 1 is a brief review of the formulation of the Hamiltonian LGT. It discusses two common procedures for obtaining the Kogut-Susskind (KS) Hamiltonian, which is needed for the calculation of transition amplitudes in lattice systems. The procedures in question are (i) the canonical method where one performs a Legendre transformation on the lattice Lagrangian to obtain the lattice Hamiltonian. (ii) The transfer matrix method, in which one constructs a partition function in terms of a transfer matrix operator [23] as well as the Wilson action [1], for extracting the discretized version of the Hamiltonian on the lattice.

In Chapter 2, we calculate the transition amplitudes under evolution of the KS Hamiltonian for the U(1) gauge group, in (2+1)-dimensions. For this calculation, we use some group theoretical methods, as well as the path integral technique. We obtain a general formula which is employed for the construction of physical stochastic basis states, and the Monte Carlo simulations needed for extracting the spectra and wave functions of the theory.

Chapter 3 deals with stochastic basis states, and presents two methods of constructing such basis states, which are required for the numerical computation of transition amplitudes. The methods are based on the analytic formulae obtained in Chapter 2, as well as the path integral approach.

In Chapter 4 we illustrate the technique of MCH by constructing an effective Hamiltonian using the stochastic basis states and transition amplitudes. We compute the energy spectrum and wave functions for the kinetic part of the KS Hamiltonian, for some lattice sizes in two spatial dimensions. Such spectrum enables us to obtain thermodynamical functions. We will present two of those functions. We also obtain the spectrum of the full Hamiltonian for two small lattices.

There are also two appendices related to this part of the thesis. Appendix A contains some informations about the Peter-Weyl theorem, which is used in Chapter 2, in order to compute transition amplitudes. Appendix B discusses the algorithms which we have employed for our lattice numerical simulations. It contains some basic material about the Monte Carlo and the molecular dynamics methods. It also describes the checkerboard and the linear preconditioning methods, used for updating lattice configurations.

Part II The physics of billiards historically was born in the beginning of 1900's by Lord Kelvin [25]. It was considered in order to demonstrate the ergodic properties of the ideal gas, by studying the motion of a point-particle inside a triangular planar area with rigid walls. Since then, classical billiard systems have attracted wide attentions in mathematics and physics to explain irregular (chaotic) features in dynamical systems.

In general, billiard systems describe a point mass moving in a planar closed area $\Omega \in \mathbb{R}^2$, with reflecting motion at a smooth boundary $\Gamma \sim \partial\Omega$. In the absence of friction or any external force, particles in the billiard region move freely in between collisons with the boundary. According to this, the dynamics of such a conservative system is characterized by the geometry of the billiard boundary. For example, a billiard with circular shaped wall represents an integrable system, where particles have stable periodic orbits [26]. In contrast, the Sinai and the Bunimovich stadium billiards [27, 28, 29] (see Fig.[1]) are examples of fully chaotic systems. The presence of external fields also creates another class of billiards,

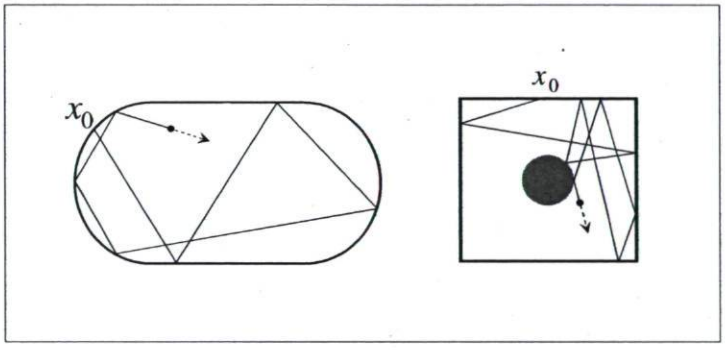

Figure 1: Left: Bunimovich stadium billiard. Right: Sinai billiard

namely dissipative systems. An external force influences the motion of the billiard ball and may create classical trajectories with curved sections in the billiard zone Ω. This also occurs when Ω has non-Euclidean geometry, i.e. non-zero curvature [30, 31, 32]. In such cases, the classical billiard dynamics not only depends on the shape of the outer boundary Γ, but also on the dynamics of the motion in Ω. These types of billiards are known as "curved-trajectory billiards" [33]. Several theoretical and experimental studies have been carried out on these systems. For example, gravitational billiards [34, 35, 36, 37, 38, 39] and magnetic billiards [40, 41, 42, 43] are frequently studied curved-trajectory systems, related to atom optics and condensed matter physics.

There are also numerous experimental and theoretical works on the subject of billiards in quantum chaos [25, 44, 45, 46, 47]. As a remarkable application of chaotic billiards, we can refer to quantum dots (also known as nanocrystals) in physics of semiconductors. The shape of these nanostructures is usually represented by the Bunimovich stadium billiards, containing excitation pairs (electrons and holes) [25]. Miao et al. [48] have recently found

that graphene (a one-atom thick plane of carbon atoms arranged in hexagonal rings) can act as a billiard table in atomic scale. In such a microscopic table, electric charges act as quantum billiard balls and reflect by graphene's boundaries. Such electronic materials can be used to develop new kinds of transistors, based on quantum physics.

Furthermore, ultra cold atoms within some spatial patterns of billiard geometries have been studied by Milner et al. [49] and Friedman et al. [50]. They present some experimental results of integrable and chaotic motion of ultracold rubidium atoms restricted in a billiard-shaped optical dipole potential, generated by laser beams. Via atomic trajectories inside a number of optical billiard sytems (elliptical, circle and tilted-stadium), they probe the effects of gravity, velocity spread, scattering and wall softness. They also show that this optical billiard is useful to study classical and quantum chaos, as well as their relation with atomic collisions, external fields, temporal charges, quantum statistics, and noise.

The Sinai billiard has also been a model system to explore the spectral properties of chaotic quantum systems. Here we refer to the Sinai billiard-shaped microwave cavities, which have been widely investigated by Sridhar et al. [51, 61], Stöckmann et al. [56, 53, 54, 55] and Dembrowski et al. [57, 58, 59, 60]. For instance, through microwave quantum chaos experiments, Sridhar et al. [61] have shown that a 2D Sinai microwave cavity reveals universal properties in spectral and eigenfunction statistics. In addition, they have studied a 2D planar system of n disks by microwave experiments, indicating that the quantum resonances of this system correspond to quantum and classical resonances of dynamical Ruelle zeta-functions. Here, let us mention that a two-dimensional n-disk system is, actually, a 2D Lorentz gas, regarding n-Sinai billiards as unit cells of the system (in particular, it is a hyperbolic system with no ergodic properties).

Quantum systems with fully chaotic classical analog have been shown in experiments and computer simulations to possess universal properties [62, 46, 47]. This means that the statistical fluctuation properties of spectra become independent of the particular quantum system, and exhibit a universal behavior [63]. In quantum chaos, the universality of level spacing fluctuations has been observed in a number of systems in nuclear and atomic physics. Examples are the heavy nuclei resonances [63, 64, 65], the non-relativistic hydrogen atom in a uniform magnetic field [66, 67, 68], the diamagnetic helium atom [69], and so forth.

Now the question is: do the classical fully chaotic systems also exhibit spectral properties, in agreement with random matrix theory (RMT) predictions of universality of spectral statistics?

This question was addressed by Argaman et al. [70], who found a universal behavior in two-point correlation functions of actions of classical periodic orbits (in classical chaotic

systems). However, they left this question open if these action correlation functions can be explained on a completely classical level. In order to answer that, Laprise et al. [71, 72] recently have observed universality in level spacing fluctuations of fully chaotic classical systems, using RMT. In particular, this has been shown by computer simulations for the Bunimovich stadium [29, 71] and cardioid billiards [71, 73, 74].

In the second part of this thesis, we attempt to answer this question for the two-dimensional Lorentz gas. By constructing matrices of length of trajectories in a classical framework, we analyze the spectral fluctuations of such matrices, to study the universal behavior of this chaotic system. This will be done using techniques form RMT.

Another interesting problem is the transport properties of this system. An example for studying this topic is the diffusion coefficient of the Lorentz gas. In order to investigate this property, we propose to use the lengths of trajectories for evaluating the diffusion constant of the Lorentz gas in the finite-horizon regime.

Remaining chapters of this part are organized as follows:

Chapter 5 covers some details about RMT as well as its application in quantum chaos. Here we also talk about level spacing analysis, which we need for our numerical simulations in the Lorentz gas and the optical billiard.

In chapter 6 we study the level spacing statistics of two systems in order to see if universality exists in their spectral fluctuations. First we consider the 2D Lorentz gas in the finite and the infinite-horizon regimes. Second, we study a quasi-potential system which we name it as an optical billiard. To this end, we employ the length matrices of trajectories, generated by a moving-particle within billiard areas.

Chapter 7 treats the diffusion properties of the Lorentz gas. We present some results of the diffusion coefficient of this system, computed via the lengths of trajectories. We show that the length variances confirm a normal diffusion for a bounded Lorentz gas.

Remarks and discussions for both parts of the thesis are presented in chapter 8.

There is also a short appendix related to this part of the thesis. Appendix C involves the algorithm of tracing the random-walk motion of billiard balls, inside billiard zones. It shows the general procedure of constructing the trajectories of point-particle in the interior of the billiard domains.

Part I

Excited States in $U(1)_{2+1}$ Lattice Gauge Theory

Chapter 1

Hamiltonian Lattice Gauge Theory

Nowadays, the standard approach in LGT is the Lagrangian formulation, in which most numerical calculations have been performed via Monte Carlo techniques. Nevertheless, there are some areas of research where progress in the Lagrangian method has been quite slow. Some examples are the calculations of excited states, the computation of hadron wave functions and the determination of the QCD phase diagram of high temperature and finite density, and so on. These problematic situations suggest that alternative methods should be regarded.

A feasible alternative approach is the Hamiltonian LGT [4], which may have a number of advantages. It has been suggested that the Hamiltonian LGT could handle finite density QCD, because there is no complex action problem [75]. Other areas in which Hamiltonian LGT may be preferred over the Lagrangian method are: calculation of excited sites, time dependent quantities and wave functions. A preferable aspect of the Hamiltonian approach is that it reduces LGT to a many-body problem. Thus a host of analytic techniques from nuclear and condensed matter many-body theory is applicable. In spite of these advantages, however, the Hamiltonian formulation has not been discussed in the literature as extensively as the Lagrangian formulation, and it is still open to more studies.

In this chapter, we review two procedures of constructing the lattice Hamiltonian. One is based on Legendre transformations via the lattice Lagrangian, and the other is based on transfer matrices, which are obtained using the Wilson action. The result of these methods is the KS Hamiltonian, which is the starting point of our calculations in the next chapters. But, first let us start with some fundamental concepts in LGT.

1.1 Lattice action and Lagrangian

In the continuum limit, the gluonic Yang-Mills Lagrangian is given by

$$\mathcal{L}_{YM} = -\frac{1}{4}\int F^{\alpha}_{\mu\nu}(\mathbf{x})F^{\alpha}_{\mu\nu}(\mathbf{x})\, d^3x \;=\; \int \mathscr{L}\, d^3x\,, \tag{1.1}$$

where $F_{\mu\nu}$ is the field tensor. In general, for a non-Abelian gauge theory (e.g. QCD) one has

$$F^{\alpha}_{\mu\nu}(\mathbf{x}) = \partial_\mu A^{\alpha}_{\nu}(\mathbf{x}) - \partial_\nu A^{\alpha}_{\mu}(\mathbf{x}) + g\, f^{\alpha\beta\gamma} A^{\beta}_{\mu}(\mathbf{x}) A^{\gamma}_{\nu}(\mathbf{x})\,, \tag{1.2}$$

where g is the bare coupling constant, A_μ is the four-vector potential and the symbols $f^{\alpha\beta\gamma}$ are the structure constants of the gauge group. Also, the Yang-Mills action is given by

$$S_{YM} = \frac{1}{4}\int F^{\alpha}_{\mu\nu}(\mathbf{x})F^{\alpha}_{\mu\nu}(\mathbf{x})\, d^4x \;=\; -\frac{1}{2g^2}\int \mathrm{Tr}\left[F_{\mu\nu}(\mathbf{x})F_{\mu\nu}(\mathbf{x})\right] d^4x\,, \tag{1.3}$$

with

$$F_{\mu\nu}(x) = -igF^{\alpha}_{\mu\nu}(x)\lambda^{\alpha}\,, \tag{1.4}$$

where λ^{α}'s are the gauge group Hermitian generators (e.g. $\alpha = 1, 2, ..., 8$ for the group SU(3)).

Before discretizing the action and Lagrangian, one considers the Wilson line

$$\ell(C) = P\,\exp\left[ig\int_C A^{\alpha}_{\mu}(\mathbf{x})\lambda^{\alpha}dx^{\mu}\right] \tag{1.5}$$

along the path C, and the Wilson loop

$$W(C) = \mathrm{Tr}\,[\ell(C)] = \mathrm{Tr}\left\{P\,\exp\left[ig\oint_C A^{\alpha}_{\mu}(\mathbf{x})\lambda^{\alpha}dx^{\mu}\right]\right\}\,, \tag{1.6}$$

for a closed path C, which is a gauge invariant quantity [2, 5, 23].

On a lattice, the shortest Wilson line is given by

$$U_\mu(\mathbf{x}) = \exp\,[-a\,A_\mu(\mathbf{x})] = \exp\,[iag\,A^{\alpha}_{\mu}(\mathbf{x})\,\lambda^{\alpha}]\,, \tag{1.7}$$

where $U_\mu(\mathbf{x})$ is the link variable on the lattice, with the direction on μ and origin at $\mathbf{x}$. The link variable is, in fact, a matrix in the gauge group G, and it transports color(charge) information between lattice points. The elementary (planar) Wilson loop on the lattice, as a local gauge invariant object, is a square defined by multiplication of four neighboring links in the plane (μ-ν):

$$U_\square = U_\mu(x)U_\nu(x + a_\mu)U^{\dagger}_{\mu}(x + a_\nu)U^{\dagger}_{\nu}(x)\,. \tag{1.8}$$

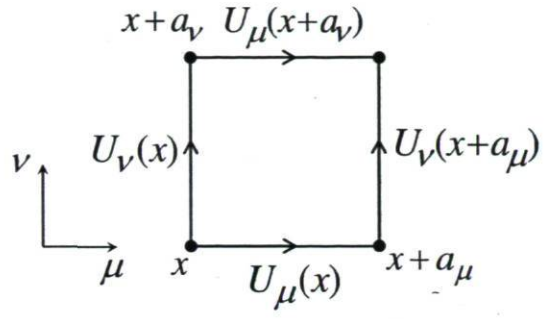

Figure 1.1: An elementary plaquette variable, containing four links and four sites in the plane $\mu - \nu$.

This quantity is called a plaquette variable[1] (see Fig.[1.1]). For pure gauge theory, the gauge invariant lattice action is defined in terms of plaquette variables by [5]

$$S = \frac{2N}{g^2}\sum_{\square}\left[1 - \frac{1}{2N}\mathrm{Tr}(U_{\square} + U_{\square}^{\dagger})\right] = \frac{2N}{g^2}\sum_{\square}\left[1 - \frac{1}{N}\mathrm{Re\ Tr}U_{\square}\right], \tag{1.9}$$

where N refers to the dimension of the gauge group SU(N). Likewise, one must consider the fermionic part of the action [2]. Here let us recall that, making the substitution

$$\sum_{\square} = \sum_{x}\sum_{\mu\nu} \to \int \frac{1}{2a^4} d^4x \sum_{\mu\nu} \tag{1.10}$$

with some algebraic calculations, gives the Eq.(1.3) of the continuum limit ($a \to 0$).

The lattice Lagrangian and its density (for a symmetric hypercubic lattice) are respectively given by

$$\mathcal{L} = -\frac{2N}{ag^2}\sum_{\square}\left[1 - \frac{1}{2N}\mathrm{Tr}(U_{\square} + U_{\square}^{\dagger})\right] \tag{1.11}$$

and

$$\mathscr{L} = -\frac{2N}{a^4g^2}\sum_{\square}\left[1 - \frac{1}{2N}\mathrm{Tr}(U_{\square} + U_{\square}^{\dagger})\right]. \tag{1.12}$$

1.2 Hamiltonian formulation

To obtain the lattice Hamiltonian theory, one can use the standard method of Legendre transformation [76, 77] or the transfer matrix method [23, 78].

[1]The Wilson loops along the temporal (thermal) direction of a lattice are named Polyakov loops, which are applied to probe the quark-antiquark potential (i.e., the quark confinement phenomenon).

1.2.1 The method of Legendre transformation

To construct the Hamiltonian on the lattice, one works in a temporal gauge (like $A_0 = 1$), which means to fix all time-like links to identity. To this end, one separates temporal and spatial plaquettes and sets the temporal links to unity. Thus the Lagrangian density is characterized by

$$\mathscr{L} = \frac{1}{g^2 a_s{}^2 a_t{}^2} \sum_{\mu\nu} \left\{ \mathrm{Tr}\left[U^\dagger_{\mu\nu}(x, t + a_t)\, U_{\mu\nu}(x, t) \right] + \mathrm{H.c.} \right\} + \frac{1}{g^2 a_s{}^4} \sum_{\square_s} \left[\mathrm{Tr} U_\square + \mathrm{Tr} U^\dagger_\square \right] , \quad (1.13)$$

where the constant term in the Eq.(1.12) has been ignored. Notice that $U_{\mu\nu}$ denotes the link variable connecting the lattice sites μ and ν.

On the other hand, one has

$$\begin{aligned} &\mathrm{Tr}\left[U^\dagger_{\mu\nu}(x, t + a_t)\, U_{\mu\nu}(x, t) \right] + \mathrm{H.c.} \; = \\ &-\mathrm{Tr}\left\{ \left[U^\dagger_{\mu\nu}(x, t + a_t) - U^\dagger_{\mu\nu}(x, t) \right] \left[U_{\mu\nu}(x, t + a_t) - U_{\mu\nu}(x, t) \right] \right\} \; + \; \text{const.} \end{aligned} \quad (1.14)$$

Therefore, the first term of Eq.(1.13) is replaced by

$$-\frac{1}{g^2 a_s{}^2} \sum_{\mu\nu} \mathrm{Tr} \left\{ \left[\frac{U^\dagger_{\mu\nu}(x, t + a_t) - U^\dagger_{\mu\nu}(x, t)}{a_t} \right] \left[\frac{U_{\mu\nu}(x, t + a_t) - U_{\mu\nu}(x, t)}{a_t} \right] \right\} . \quad (1.15)$$

Taking $a_t \to 0$, one obtains

$$\mathcal{L} = \frac{a_s}{g^2} \sum_{\mu\nu} \mathrm{Tr}(\dot{U}^\dagger_{\mu\nu} \dot{U}_{\mu\nu}) \; + \; \frac{1}{g^2 a_s} \sum_{\square_s} \left[\mathrm{Tr} U_\square + \mathrm{Tr} U^\dagger_\square \right] , \quad (1.16)$$

which is a conventional quantum mechanical picture of LGT in terms of Lagrangian.

Now, using the Legendre transformation

$$\mathcal{H} = \sum \left[\dot{U}^\dagger_{\mu\nu} \frac{\partial \mathcal{L}}{\partial \dot{U}^\dagger_{\mu\nu}} \; + \; \dot{U}_{\mu\nu} \frac{\partial \mathcal{L}}{\partial \dot{U}_{\mu\nu}} \right] - \mathcal{L} , \quad (1.17)$$

the lattice Hamiltonian is deduced as

$$\mathcal{H} = \frac{a_s}{g^2} \sum_{\mu\nu} \mathrm{Tr}(\dot{U}^\dagger_{\mu\nu} \dot{U}_{\mu\nu}) \; - \; \frac{1}{g^2 a_s} \sum_{\square_s} \left[\mathrm{Tr} U_\square + \mathrm{Tr} U^\dagger_\square \right] . \quad (1.18)$$

The theory is not quantized yet. To quantize it in the temporal gauge, one enforces the canonical commutation relations

$$\begin{aligned} \left[\hat{\mathbf{E}}^\alpha_{\mu\nu}(\mathbf{x}) \, , \; \hat{U}_{\mu\nu}(\mathbf{y}) \right] &= \lambda^\alpha \hat{U}_{\mu\nu}(\mathbf{y}) \delta_{\mu\nu} \delta^3_{\mathbf{x},\mathbf{y}} \\ \left[\hat{\mathbf{E}}^\alpha_{\mu\nu}(\mathbf{x}) \, , \; \hat{\mathbf{E}}^\beta_{\mu\nu}(\mathbf{y}) \right] &= i \epsilon^{\alpha\beta\gamma} \hat{\mathbf{E}}^\gamma_{\mu\nu}(\mathbf{x}) \delta_{\mu\nu} \delta^3_{\mathbf{x},\mathbf{y}} . \end{aligned} \quad (1.19)$$

Here the operators $\hat{\mathbf{E}}^{\alpha}_{\mu\nu}(\mathbf{x})$ denote color-electric fields with the color index α, outgoing from the lattice point $\mathbf{x}$ in the direction $\mu \rightarrow \nu$. They represent the variables conjugated to the link variables $U_{\mu\nu}(\mathbf{x})$. One can see that $\hat{\mathbf{E}}^{\alpha}_{\mu\nu}(\mathbf{x})$ acts as a differential operation on the link variable $U_{\mu\nu}(\mathbf{x})$, with respect to the parameters of the SU(N) rotation.

Since $\hat{\mathbf{E}}^{\alpha}_{\mu\nu}$ generates the local gauge rotation as a symmetry of $\mathcal{L}$, one can write

$$\begin{aligned} \hat{\mathbf{E}}^{\alpha}_{\mu\nu} &= \frac{\partial \mathcal{L}}{\partial \dot{U}_{\mu\nu}}[i\lambda^{\alpha}U]_{\mu\nu} + \frac{\partial \mathcal{L}}{\partial \dot{U}^{\dagger}_{\mu\nu}}[-i\lambda^{\alpha}U]^{\dagger}_{\mu\nu} \\ &= i\frac{a_s}{g^2}\left[\mathrm{Tr}\left(\dot{U}^{\dagger}_{\mu\nu}\lambda^{\alpha}U_{\mu\nu}\right) - H.c.\right] . \end{aligned} \tag{1.20}$$

One can compute the quadratic Casimir[2] operator $\hat{\mathbf{E}}^{\alpha}_{\mu\nu}\mathbf{E}^{\alpha}_{\mu\nu}$ using the operators $\hat{\mathbf{E}}^{\alpha}_{\mu\nu}$. The result is

$$\hat{\mathbf{E}}^{\alpha}_{\mu\nu}\hat{\mathbf{E}}^{\alpha}_{\mu\nu} = \frac{a_s^2}{2g^4}\mathrm{Tr}(\dot{U}^{\dagger}_{\mu\nu}\dot{U}_{\mu\nu}) . \tag{1.21}$$

Consequently the KS Hamiltonian is given by

$$\mathcal{H}_{KS} = \frac{g^2}{2a_s}\sum_{<\mu\nu>,\mathbf{x}} \hat{\mathbf{E}}^{\alpha}_{\mu\nu}(\mathbf{x})\hat{\mathbf{E}}^{\alpha}_{\mu\nu}(\mathbf{x}) - \frac{1}{g^2 a_s}\sum_{\square_s}\left[\mathrm{Tr}U_{\square} + \mathrm{Tr}U^{\dagger}_{\square}\right] , \tag{1.22}$$

which defines the dynamics of the Hamiltonian LGT for the gauge group G. The first part is the electric (kinetic) Hamiltonian, and the second (i.e., the potential part) is called the magnetic Hamiltonian. It is related to the magnetic field as follows:

$$\begin{aligned} U_{\square} &= U_{\mu}(x)U_{\nu}(x+a_{\mu})U^{\dagger}_{\mu}(x+a_{\nu})U^{\dagger}_{\nu}(x) \\ &\propto \exp\left[ik_0 A_{\mu}(x)\right]\exp\left[ik_0 A_{\nu}(x+a_{\mu})\right]\exp\left[-ik_0 A_{\mu}(x+a_{\nu})\right]\exp\left[-ik_0 A_{\nu}(x)\right] \\ &= \exp\left[ik_0\Big(A_{\mu}(x) + A_{\nu}(x+a_{\mu}) - A_{\mu}(x+a_{\mu}) - A_{\nu}(x)\Big)\right] \\ &= \exp\left[ik_0\vec{\nabla}\times\mathbf{A}\right] = \exp\left[ik_0\mathbf{B}\right] , \end{aligned} \tag{1.23}$$

where $\mathbf{B}$ is the magnetic field of a plaquette (see Fig.[1.2] and Ref. [79]). Therefore one finds

$$\mathrm{Tr}U_{\square} + \mathrm{Tr}U^{\dagger}_{\square} = 2\ \mathrm{Re}\ \mathrm{Tr}U_{\square} \propto \cos(k_0 B) . \tag{1.24}$$

Consequently, one has

$$\mathcal{H}_{KS} = \mathcal{H}^{\mathrm{elec}} + \mathcal{H}^{\mathrm{mag}} \tag{1.25}$$

[2]An operator which commutes with all elements of a Lie group is said to be a Casimir Operator of that group.

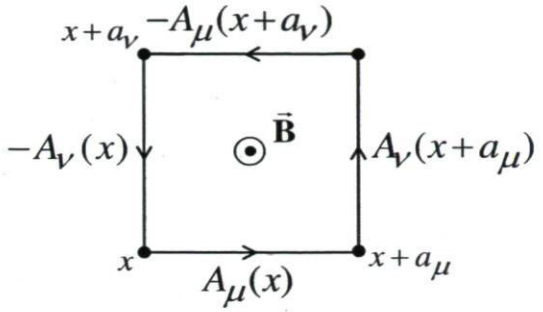

Figure 1.2: Magnetic field of an elementary plaquette [79].

with

$$\mathcal{H}^{\text{elec}} = \frac{g^2}{2a_s} \sum_{\mu\nu,\mathbf{x}} \hat{\mathbf{E}}^{\alpha}_{\mu\nu}(\mathbf{x}) \hat{\mathbf{E}}^{\alpha}_{\mu\nu}(\mathbf{x}) \tag{1.26}$$

and

$$\mathcal{H}^{\text{mag}} = -\frac{1}{g^2 a_s} \sum_{\square_s} \left[\text{Tr} U_{\square} + \text{Tr} U^{\dagger}_{\square} \right] , \tag{1.27}$$

as the electric and magnetic Hamiltonians, respectively.

1.2.2 Transfer matrix method

Another approach to construct the lattice Hamiltonian is the idea of transfer matrix [2, 5, 23, 78]. The basis of this idea is similar to that in the ordinary quantum mechanics, for linking the Hamiltonian and the Lagrangian pictures of quantum mechanics. In other words, it relates the Feynmann path integral formulation to the conventional operator formalism.

Working on a lattice with an Euclidean descretized time, and considering the pure gauge Wilson action, the partition function of the system is given by

$$\mathcal{Z} = \int [dU] \, e^{-S_W} . \tag{1.28}$$

The local nature of the Wilson action allows one to write the partition function $\mathcal{Z}$ in a fixed temporal gauge (i.e. all time-like links are unity due to $A_0 = 0$) as

$$\mathcal{Z} = \text{Tr}(\hat{T}^N) = \int \prod_t \left(\hat{T}[U(t + a_t)U(t)] \prod dU \right) . \tag{1.29}$$

Here $\hat{T}$ is the transfer matrix of the theory. It is a self-adjoint bounded operator in a Hilbert space $\mathscr{H}$. Also, N is the number of time slices along a time axis with periodic boundary conditions. Before going further, we define the Hilbert space $\mathscr{H}$.

The Hilbert space of the Kogut-Susskind Hamiltonian

The Hilbert space of this theory is given by all square integrable functions $\psi(U) = \psi(\{U_{\mu\nu}(x)\})$, with respect to a unique normalized measure on the gauge group G, such that

$$\int [dU]\, |\psi(U)|^2 < \infty\,, \quad [dU] = \prod_{<\mu\nu>,x} dU_{\mu\nu}(x)\,. \tag{1.30}$$

The measure $dU_{\mu\nu}(x)$ is the gauge invariant Haar measure over the gauge group. Notice that the physical Hilbert space of the theory is composed of the gauge invariant square integrable functions.

A state $|\psi\rangle$ in this space is specified by a wave function $\psi(U)$ depending on a configuration $U = \{U_{\mu\nu}(x)\}$. Choosing the basis states $|U\rangle$ results

$$\int [dU]\ |U\rangle\langle U| = 1\,, \tag{1.31}$$

and

$$\langle U|U'\rangle \ = \prod_{<\mu\nu>,x} \delta\left(U_{\mu\nu}(x), U'_{\mu\nu}(x)\right)\,. \tag{1.32}$$

Therefore, the state $|\psi\rangle$ is represented by

$$|\psi\rangle \ = \int [dU]\ |U\rangle\,\psi(U)\,, \quad \text{with} \quad \psi(U) \propto \langle U|\,\psi\rangle\,, \tag{1.33}$$

and the inner product defining square integrability is

$$\langle\phi|\psi\rangle \ = \int [dU]\ \phi^{\star}(U)\,\psi(U)\,. \tag{1.34}$$

The physical states have to be gauge invariant under the local rotation of gauge group G. This condition is satisfied by the Gauss' law constraint of the theory at each lattice site, that is

$$\hat{C}_{\mu\nu}(x) = \sum_{<\mu\nu>,x} \hat{\mathbf{E}}_{\mu\nu}(x)\ , \quad \hat{C}_{\mu\nu}(x)\,|\psi\rangle = 0\,. \tag{1.35}$$

It means that the net electric flux at any site is zero (notice that there is no charge on the lattice sites in the case of the pure gauge theory).

Now we go back to the computation of the transfer matrix. The transfer matrix is gauge invariant under the restricted class of gauge transformations, and it is strictly positive with eigenvalues larger than zero. It operates on the wave function $|\psi\rangle$ of the Hilbert space $\mathscr{H}$ as

$$|\psi(t + a_t)\rangle = \hat{T}\,|\psi(t)\rangle\ . \tag{1.36}$$

This means that the system has been evolved from one time slice to the rest. The positivity of $\hat{T}$ guarantees the existence of the Hamiltonian

$$\mathcal{H} \propto -\frac{1}{a_t} log\, \hat{T} \,. \tag{1.37}$$

Therefore one finds [23],

$$\mathcal{Z} \;=\; \mathrm{Tr}(\hat{T}^N) = \mathrm{Tr}(e^{-\mathcal{H}\, a_t})^N = \mathrm{Tr}(e^{-\mathcal{H}\mathcal{T}}) = \int [dU]\, e^{-S_W} \,, \tag{1.38}$$

where $\mathcal{T}$ is the Euclidean time.

The transfer matrix operator in terms of its matrix elements (in the introduced Hilbert space $\mathscr{H}$) is characterized by

$$\hat{T}_{U',U} = \langle U'|\, \hat{T}\, |U\rangle \equiv \langle U'|\, e^{-\mathcal{H}a_t}\, |U\rangle \;. \tag{1.39}$$

It operates on the infinitesimal time-step a_t and fulfills the Eq.(1.38). Fixing the temporal gauge to identity and considering the asymmetric form of the Wilson action [23]

$$S = -\frac{2a_s}{g^2 a_t} \sum_{\square_t} \mathrm{Re\ Tr} U_{\square_t} \;-\; \frac{2a_t}{g^2 a_s} \sum_{\square_s} \mathrm{Re\ Tr} U_{\square_s} \,, \tag{1.40}$$

one obtains [23]

$$\hat{T}_{U',U} \;=\; \exp\left[\frac{2a_s}{g^2 a_t} \sum_{\mu} \mathrm{Re\ Tr}\left(U_\mu\, U_\mu'^{\,\dagger}\right)\right] \times \exp\left[\frac{2a_t}{g^2 a_s} \sum_{\square_s} \mathrm{Re\ Tr} U_{\square_s}\right], \tag{1.41}$$

where $U_{\mu\nu} = U_{\mu\nu}(x,t)$ and $U'_{\mu\nu} = U_{\mu\nu}(x, t + a_t)$.

In the ordinary quantum mechanics, one can write the operator $\hat{T}$ in terms of the canonically conjugate variables position $\hat{\mathbf{x}}$ and momentum $\hat{\mathbf{p}}$. In the present Hilbert space $\mathscr{H}$, one can define the matrix valued operators $\hat{U}_\mu$ and the unitary operators $R_{\mu\nu}(\mathscr{G})$ on the analogy of $\hat{\mathbf{x}}$ and $\hat{\mathbf{p}}$, respectively. In accordance with this, one writes [23]

$$\begin{aligned} \hat{U}_{\mu\nu}\, |U\rangle \;&=\; U_{\mu\nu}\, |U\rangle \;, \\ R_{\mu\nu}(\mathscr{G})\, |U\rangle \;&=\; |U'\rangle \;, \\ U'_{\mu\nu} \;&=\; \mathscr{G}\, U_{\mu\nu} \,, \end{aligned} \tag{1.42}$$

where $\mathscr{G}$ is an element of the gauge group G. The operator $R_{\mu\nu}(\mathscr{G})$ translates the basis state $|U\rangle$ (likewise the behavior of the canonical momentum operator on position state $|\mathbf{x}\rangle$, in quantum mechanics), and it satisfies the group representation property

$$R_{\mu\nu}(\mathscr{G}) R_{\mu\nu}(\mathscr{G}') = R_{\mu\nu}(\mathscr{G}\mathscr{G}') \,. \tag{1.43}$$

Therefore, one can write the transfer matrix $\hat{T}$ as

$$\hat{T} = \left\{ \prod_{<\mu\nu>} \left(\int \mathrm{d}\mathcal{G} R_{\mu\nu}(\mathcal{G}) \exp\left[\frac{2a_s}{g^2 a_t} \mathrm{ReTr}\, \mathcal{G} \right] \right) \right\} \times \exp\left[\frac{2a_t}{g^2 a_s} \sum_{\square_s} \mathrm{ReTr}\, U_{\square_s} \right] . \tag{1.44}$$

In order to evaluate the group integral in the above equation, one can parameterize the group elements $\mathcal{G}$ and the operator $R_\mu(\mathcal{G})$ in terms of the group generators (see Eq.(1.4)). It reads as

$$\begin{aligned} \mathcal{G} &= \exp\left[i\omega^\alpha \lambda^\alpha \right] , \\ R_{\mu\nu}(\mathcal{G}) &= \exp\left[i\omega^\alpha \hat{E}^\alpha_{\mu\nu} \right] , \end{aligned} \tag{1.45}$$

where ω^α and λ^α are group parameters and group generators, respectively, and $\hat{E}^\alpha_{\mu\nu}$ denotes the canonical momentum operator (here the color-electric field operator). In the Hamiltonian formulation of LGT, time is a continuous parameter. This means that one has to take the temporal lattice spacing to zero, while the spatial lattice spacing is fixed. In this limit, the group integrals in Eq.(1.44) are dominated by group elements near the unity, which occurs when ω becomes small in Eq.(1.45). Considering this point and replacing Eq.(1.45) in Eq.(1.44), one obtains a Gaussian integral [2]. Evaluating that integral yields

$$\hat{T} \propto \exp(-\mathcal{H} a_t) , \tag{1.46}$$

where

$$\mathcal{H} = \frac{g^2}{2a_s} \sum_{<\mu\nu>} \hat{\mathbf{E}}^2_{\mu\nu} + \frac{2}{g^2 a_s} \sum_{\square_s} \left[\mathrm{ReTr}\, U_\square \right] , \tag{1.47}$$

represents the KS Hamiltonian on a lattice.

1.3 Application of Hamiltonian methods in LGT

Several techniques have been employed in the Hamiltonian approach of LGT, in order to solve lattice QCD. Examples are t-expansion method [80, 81, 82, 83], Green's function Monte Carlo method [75, 84], strong coupling expansion [85, 86], coupled cluster method [87, 88, 89, 90, 91], variational techniques [92, 93, 94] and black box method [106].

In the Hamiltonian approach, these methods allow to investigate lattice QCD in different coupling regimes, for example the ground state expectation value of the plaquette operators, as well as the string tension in the lattice QCD. Lattice thermodynamics for the gauge groups SU(2) and SU(3) is also another example by the Hamiltonian methods. They yield an estimation for the ground state energy as well as lower excited levels (i.e. the glueball masses 0^{++}, 1^{+-}, etc.) in lattice QCD.

Chapter 2

Transition Amplitudes in U(1) Lattice Gauge Theory

In this chapter we develop a formulation for transition amplitudes in (2+1)-dimensional U(1) LGT. Using some group theoretical methods as well as the standard path integral, we construct the gauge invariant amplitudes of transition under the electric part of KS Hamiltonian. From such a gauge invariance procedure, we drive a formula for the electric transition amplitude, which can be used in Chapter 3 for generating the stochastic basis states. Moreover, it will be employed in Chapter 4 for the computation of spectrum and wave functions of $U(1)_{2+1}$ LGT.

2.1 $U(1)_{2+1}$ LGT

The original formulation of LGT by Wilson was based on U(1) gauge thory [1]. It has been shown that the pure U(1) LGT in (3+1) dimensions, contains two different phases [95, 96, 97, 98]. In the weak coupling limit, the linear confinement is absent and the interaction between charges is Coulomb type. In the strong coupling regime, the lattice system is in a confining phase, and the gauge bosons (photons) do not escape away. These two phases are separated by a first order phase transition [99].

On the other hand, the compact $U(1)_{2+1}$ LGT is asymptotically free and does not undergo any phase transition, when passing from the strong coupling to the weak coupling regime [100, 101, 102, 103]. The message of this property is that, U(1) LGT in (2 + 1) dimensions always (i.e., for all couplings) remains in a confining phase. Consequently, 3-

dimensional U(1) lattice theory is similar to 4-dimensional SU(N) lattice gauge theories (such as lattice QCD).

In addition, using the Villain approximation [104] of the Wilson action, it has been shown that $U(1)_{2+1}$ LGT is a renormalizable theory. The continuum limit of this theory is taken by varying the coupling constant g, as the lattice spacing tends to zero ($a \to 0$), in such a way that some physical quantity is held at a fixed value. If one holds the photon mass gap fixed (finite nonzero) as $a \to 0$, then the continuum limit exists as $g \to 0$. However, it does not lead to the familiar Maxwell electrodynamics, but to a theory of massive glueballs. The ordinary free electrodynamics is restored by preserving the unrenormalized electric charge $e^2 = g^2/a$ in a fixed vlue, as $a \to 0$ [100, 101, 102, 105].

Because of the above-mentioned properties, $U(1)_{2+1}$ LGT plays the role of a toy model, in order to study the complicated theories, such as lattice QCD (i.e. SU(3) gauge theory).

2.2 Transition amplitudes in Hamiltonian LGT

The transition amplitude between two physical lattice states (see Fig.[2.1]) under evolution of the KS Hamiltonian is characterized by the matrix element

$$\langle U', t = T | \, U, t = 0 \rangle \equiv \langle U' | \exp[-\mathcal{H}T/\hbar] | U \rangle \, . \tag{2.1}$$

Here, T is the Euclidean time, and the states $|U\rangle$ and $|U'\rangle$ stand for the Bargmann link states,

$$|U\rangle = |U_{12}, U_{23}, ...\rangle \, , \tag{2.2}$$

which assigns a link variable $U_{\mu\nu}$ to each link $\{\mu\nu\}$ on lattice. In order to compute the above

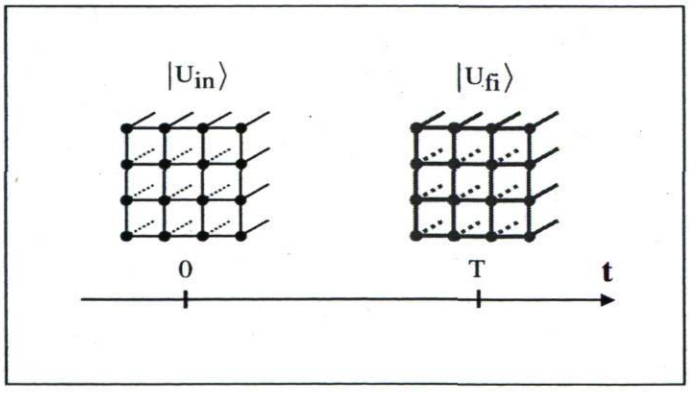

Figure 2.1: A schematic aspect of temporal transition of a lattice configuration

amplitude, we represent it as

$$\langle U'|\exp\left[-\mathcal{H}T/\hbar\right]|U\rangle = \frac{\langle U'|\exp\left[-\mathcal{H}T/\hbar\right]|U\rangle}{\langle U'|\exp\left[-\mathcal{H}^{\text{elec}}T/\hbar\right]|U\rangle} \times \langle U'|\exp\left[-\mathcal{H}^{\text{elec}}T/\hbar\right]|U\rangle \ , \quad (2.3)$$

where $\mathcal{H}^{\text{elec}}$ is the kinetic (electric) part of the KS Hamiltonian (see Chapter 1).

The first term of Eq.(2.3) can be computed numerically, which is discussed in Chapter 4. The second part is the transition amplitude under evolution of the electric part of the Hamiltonian. This term can be calculated analytically, which is the main discussion of this chapter.

2.3 Transition amplitude under evolution of the electric part of the Kogut-Susskind Hamiltonian

Let us consider the matrix element

$$\langle U'|\exp\left[-\mathcal{H}^{\text{elec}}T/\hbar\right]|U\rangle \quad (2.4)$$

as transition amplitude between Bargmann link states $|U\rangle$ and $|U'\rangle$. This propagator as a function of the group elements U' and U, depends only on the combination of $\mathcal{G} = U'^{-1}U$. To show this, let us take a group element

$$\mathcal{G} = \exp[i\omega^a\tau^a] \ , \quad (2.5)$$

where τ^a are the generators of the gauge group and ω^a are the group parameters. A time-dependent gauge transformation on a link $\{\mu\nu\}$ is given by [78]

$$R_{\mu\nu}(\mathcal{G}) = \exp[i\omega^a E^a_{\mu\nu}] \equiv \exp[i\omega\cdot\mathbf{E}_{\mu\nu}] \ , \quad (2.6)$$

where $E^a_{\mu\nu}$ is the infinitesimal generator of gauge transformations on the link $\{\mu\nu\}$. The unitary operators $R_{\mu\nu}(\mathcal{G})$ transform the link states according to [23]

$$R_{\mu\nu}(\mathcal{G})|U\rangle = |U'\rangle \quad , \quad U'_{\mu\nu} = \mathcal{G}U_{\mu\nu} \ . \quad (2.7)$$

Now we choose the group element $\mathcal{G}$ such that

$$R_{\mu\nu}(\mathcal{G})|U\rangle = |N\rangle \quad , \quad \mathcal{G} = U^{-1} \ , \quad (2.8)$$

or equivalently

$$|U\rangle = R^{-1}_{\mu\nu}(\mathcal{G})|N\rangle \ , \quad (2.9)$$

where N denotes the neutral group element. Notice that $R_{\mu\nu}$ operates solely on the link $\{\mu\nu\}$ and does not change other links.

Since $H^{\text{elec}} \propto E_{\mu\nu}^2$ is a Casimir operator, thus

$$[R_{\mu\nu}(\mathscr{G}), H^{\text{elec}}] = 0\,. \tag{2.10}$$

Consequently, we can rewrite the transition amplitude as

$$\begin{aligned}
&\langle U'| \exp\left[-\mathcal{H}^{\text{elec}} T/\hbar\right] |U\rangle \\
&= \langle U'| \exp\left[-\mathcal{H}^{\text{elec}} T/\hbar\right] \left|R_{\mu\nu}^{-1}(\mathscr{G})N\right\rangle \\
&= \left\langle R_{\mu\nu}^{-1}(\mathscr{G})U'\right| \exp\left[-\mathcal{H}^{\text{elec}} T/\hbar\right] |N\rangle \\
&= \left\langle U^{-1}U'\right| \exp\left[-\mathcal{H}^{\text{elec}} T/\hbar\right] |N\rangle\ ,
\end{aligned} \tag{2.11}$$

which means that the transition amplitude is a function of the group element $\mathscr{G} = U^{-1}U'$. Due to the Hermiticity of $\mathcal{H}^{\text{elec}}$, the amplitude must also be some function of $\mathscr{G} = U'^{-1}U$, and therefore, a symmetric function in $\mathscr{G}$ and $\mathscr{G}^{-1}$. This result holds in the Abelian case as well as in the non-Abelian case [107].

2.3.1 Transition amplitude for the gauge group U(1)

In order to express the transition amplitude, we consider the temporal transition of a single link state in the Abelian U(1) LGT. For this purpose, we use the close correspondence between quantum mechanics and lattice gauge theory. The kinetic part of the KS Hamiltonian, i.e. the squared electric field, is identified by

$$\mathcal{H}^{\text{elec}} = \frac{g^2\hbar}{2a_s} \sum_{<\mu\nu>} \hat{\mathbf{E}}_{\mu\nu}^2\,. \tag{2.12}$$

where $\hat{\mathbf{E}}_{\mu\nu}$ denotes the operator of the electric field between spatial neighboring lattice sites μ and ν. This operator has discrete eigenvalues,

$$\hat{\mathbf{E}}_{\mu\nu} \left|\lambda_{\mu\nu}\right\rangle = \lambda_{\mu\nu} \left|\lambda_{\mu\nu}\right\rangle\ , \quad \lambda_{\mu\nu} = 0, \pm 1, \pm 2, \ldots\,. \tag{2.13}$$

Therefore, the transition amplitude of a single link state can be expanded in terms of the electric eigen states

$$\begin{aligned}
\left\langle U'_{\mu\nu}\right| e^{-\mathcal{H}^{\text{elec}}T/\hbar}\left|U_{\mu\nu}\right\rangle &= \sum_{\lambda,\lambda'}\left\langle U'_{\mu\nu}\right|\lambda\rangle\langle\lambda| e^{-\mathcal{H}^{\text{elec}}T/\hbar}|\lambda'\rangle\left\langle\lambda'\right| U_{\mu\nu}\rangle \\
&= \sum_{\lambda,\lambda'}\left\langle U'_{\mu\nu}\right|\lambda\rangle\langle\lambda|\exp\left(-\frac{g^2\hbar T}{2a_s}\sum_{<\mu\nu>}\mathbf{E}^2_{\mu\nu}\right)|\lambda'\rangle\left\langle\lambda'\right| U_{\mu\nu}\rangle \\
&= \prod_{\mu\nu}\left\{\sum_{\lambda_{\mu\nu}=0,\pm1,\pm2,\ldots}\left\langle U'_{\mu\nu}\right|\lambda_{\mu\nu}\rangle\exp\left(-\frac{g^2\hbar T}{2a_s}\lambda^2_{\mu\nu}\right)\left\langle\lambda_{\mu\nu}\right| U_{\mu\nu}\rangle\right\} .
\end{aligned} \tag{2.14}$$

Due to the locality of the Bargmann link states, as well as the structure of the kinetic part of the KS Hamiltonian, this amplitude is factorized in separate amplitudes for each link. In order to evaluate such individual link amplitudes, one needs to compute the scalar product $\left\langle U_{\mu\nu}\right|\lambda_{\mu\nu}\rangle$, which defines the transition from the link basis to the electric field basis.

2.3.2 Scalar product $\langle U|\lambda\rangle$

By analogy with quantum mechanics, this scalar product is determined only by the algebraic commutator relation between the link operators $\hat{U}$ and $\hat{\mathbf{E}}$, and also the normalization of the link and electric field states. Here we would like to follow a procedure similar to the calculation of $\langle p|\,x\rangle$ from the commutator $[\hat{P},\hat{X}] = -i\hbar$, in quantum mechanics. First, let us recall the properties of a link basis state as follows [23]:

$$\begin{aligned}
\hat{U}|U\rangle &= U|U\rangle \\
\langle U'|\,U\rangle &= \delta(U'-U) \\
1 &= \int dU\ |U\rangle\langle U| ,
\end{aligned} \tag{2.15}$$

where $\int dU$ denotes a group integral, and $\delta(U'-U)$ is the δ function over group elements. Similarly, an electric field basis obeys

$$\begin{aligned}
\hat{\mathbf{E}}|\lambda\rangle &= \lambda|\lambda\rangle \\
\langle\lambda'|\,\lambda\rangle &= \delta_{\lambda',\lambda} \\
\sum_{\lambda_{\mu\nu}=0,\pm1,\ldots}|\lambda\rangle\langle\lambda| &= 1 .
\end{aligned} \tag{2.16}$$

The algebraic commutator relation of $\hat{U}$ and $\hat{\mathbf{E}}$ is characterized by

$$[\hat{\mathbf{E}}, \hat{U}] \;=\; -\hat{U}\,. \tag{2.17}$$

To compute the inner product $\langle U|\,\lambda\rangle$, we can write

$$\langle\lambda|\,[\hat{\mathbf{E}}, \hat{U}]\,|U\rangle \;=\; \langle\lambda|\,-\hat{U}\,|U\rangle \;=\; -U\,\langle\lambda|\,U\rangle\,. \tag{2.18}$$

On the other hand, expanding the commutator yields [22]:

$$\begin{aligned}
\langle\lambda|\,[\hat{\mathbf{E}}, \hat{U}]\,|U\rangle \;&=\; \lambda U\,\langle\lambda|\,U\rangle - \langle\lambda|\,\hat{U}\hat{\mathbf{E}}\,|U\rangle \\
&=\; \lambda U\,\langle\lambda|\,U\rangle \;-\; \int dX\,\langle\lambda|\,\hat{U}\,|X\rangle\,\langle X|\,\hat{\mathbf{E}}\,|U\rangle \\
&=\; \lambda U\,\langle\lambda|\,U\rangle \;+\; \int dX\left\{UX\;\langle\lambda|\,X\rangle\right\}\frac{\partial}{\partial X}\delta(X-U) \\
&=\; \lambda U\,\langle\lambda|\,U\rangle \;-\; \frac{\partial}{\partial X}\left\{UX\,\langle\lambda|\,X\rangle\right\}\Big|_{X=U} \\
&=\; \lambda U\,\langle\lambda|\,U\rangle \;-\; \left[U\,\langle\lambda|\,U\rangle + U^2\frac{\partial}{\partial U}\,\langle\lambda|\,U\rangle\right],
\end{aligned} \tag{2.19}$$

where the following property of the delta function has been applied:

$$\int_{-\infty}^{\infty} f(y)\frac{\partial}{\partial y}\delta(y-y_0)dy = -\frac{\partial f}{\partial y}\Big|_{y=y_0}\,. \tag{2.20}$$

Now, combining Eqs.(2.18) and (2.19) we obtain

$$U\frac{\partial}{\partial U}\,\langle\lambda|\,U\rangle \;=\; \lambda\,\langle\lambda|\,U\rangle\,. \tag{2.21}$$

This equation simply suggests that

$$\langle\lambda|\,U\rangle \;=\; C_\lambda(U)^\lambda\,, \tag{2.22}$$

where C_λ is a constant. This parameter is determined from the normalization condition of the electric field states, which reads

$$\begin{aligned}
\delta_{\lambda',\lambda} = \langle\lambda'|\,\lambda\rangle \;&=\; \int dU\,\langle\lambda'|\,U\rangle\,\langle U|\,\lambda\rangle \\
&=\; C'_\lambda C^\star_\lambda \int dU(U)^{\lambda'-\lambda} \;=\; C'_\lambda C^\star_\lambda \int \frac{d\alpha}{2\pi}\,\exp[i\alpha(\lambda'-\lambda)] \\
&=\; C'_\lambda C^\star_\lambda\,\delta_{\lambda',\lambda}\,,
\end{aligned} \tag{2.23}$$

where $dU = \dfrac{d\alpha}{2\pi}$ is the group integral Haar measure, and α stands for a link angle. We have also considered the parametrization of a link variable in the group U(1) as $U = \exp(i\alpha)$, and the following orthogonality relation:

$$\int_{-\pi}^{+\pi} d\xi \, e^{in\xi} e^{-in'\xi} \;=\; 2\pi\delta_{n,n'} \; . \tag{2.24}$$

From Eq.(2.23) one concludes that $C_\lambda = 1$, therefore

$$\langle \lambda |\, U \rangle \;=\; (U)^\lambda \; . \tag{2.25}$$

Now, denoting $U' = \exp(i\alpha')$ and $U = \exp(i\alpha)$, we obtain the transition amplitude for a single link as

$$\begin{aligned} &\langle U' | \exp\left[-\mathcal{H}^{\text{elec}} T/\hbar\right] | U \rangle \\ &= \sum_{\lambda=0,\pm1,\pm2,\ldots} \langle U' |\, \lambda \rangle \, \exp\left[-\frac{g^2\hbar T}{2a_s}\lambda^2\right] \langle \lambda |\, U' \rangle \\ &= \sum_{\lambda=0,\pm1,\pm2,\ldots} \exp\left[-\frac{g^2\hbar T}{2a_s}\lambda^2\right] \exp\left[i\lambda(\alpha' - \alpha)\right] \; . \end{aligned} \tag{2.26}$$

Notice that for the sake of simplicity we have dropped the index $\{\mu\nu\}$ from the link states. Now, by considering the physical part and replacing the index λ by n, one obtains

$$\begin{aligned} &\langle U' | \exp\left[-\mathcal{H}^{\text{elec}} T/\hbar\right] | U \rangle \\ &= \sum_{n=0,\pm1,\pm2,\ldots} \exp\left[-\frac{g^2\hbar T}{2a_s} n^2\right] \cos\left[n(\alpha' - \alpha)\right] \\ &= \frac{1}{2} \sum_{n=0,\pm1,\pm2,\ldots} \exp\left[-\frac{g^2\hbar T}{2a_s} n^2\right] \left[(U^{-1}U')^n + (U'^{-1}U)^n\right] \; , \end{aligned} \tag{2.27}$$

which is a symmetric polynomial in $U^{-1}U'$ and $U'^{-1}U$.

2.3.3 Scalar product $\langle U|\lambda\rangle$ via Peter-Weyl theorem

An alternative method to compute the scalar product $\langle \lambda |\, U \rangle$ is via using the Peter-Weyl theorem [108], which establishes orthogonality and completeness relations (see Appendix A for more details).

The basis functions $|\lambda\rangle$ of the electric field operator form an orthogonal and complete set in the Hilbert space of the theory [23, 108]. This is also the case for the basis of link states

$|U\rangle$, such that

$$\int dU\ |U\rangle\langle U| = 1\ \ ,\ \ \langle U'|\ U\rangle = \delta(U'-U)\,, \tag{2.28}$$

$$\sum_{\lambda=0,\pm1,\pm2,\ldots} \langle U'|\ \lambda\rangle\langle\lambda|\ U\rangle = \delta(U'-U)\,, \tag{2.29}$$

$$\int dU\ \langle\lambda'|\ U\rangle\langle U|\ \lambda\rangle = \delta_{\lambda',\lambda}\,, \tag{2.30}$$

$$\sum_{\lambda=0,\pm1,\pm2,\ldots} |\lambda\rangle\langle\lambda| = 1\ \ ,\ \ \langle\lambda'|\ \lambda\rangle = \delta_{\lambda',\lambda}\,. \tag{2.31}$$

On the other hand, according to the Peter-Weyl theorem, the orthogonality and completeness relations for SO(2) group are given by [108]

$$\frac{1}{2\pi}\int_0^{2\pi} d\phi U_m^\dagger(\phi)U_n(\phi) = \delta_{mn}\ \ ,\ \ m,n\in\{0,\pm1\pm2\} \tag{2.32}$$

and

$$\sum_{n=0,\pm1,\pm2,\ldots} U_n(\phi)U_n^\dagger(\phi') = \delta(\phi-\phi')\,. \tag{2.33}$$

The functions

$$U_m(\phi) = e^{-im\phi} \tag{2.34}$$

characterize the irreducible representations[1] of the group SO(2), and m is an eigenvalue of the infinitesimal generator J (See the theorem 6.4 in Ref. [108]). Now if we consider

$$U(\phi) = e^{i\phi}\ \ ,\ \ U^\lambda(\phi) = e^{i\lambda\phi} = \langle\lambda|\ U\rangle\ , \tag{2.35}$$

then Eq.(2.29) is identical to Eq.(2.33), and Eq.(2.30) is the same as Eq.(2.32). This means that the scalar product $\langle\lambda|\ U\rangle$ can be identified by the irreducible representation of the quantum number λ of the group SO(2).

2.4 Gauge invariance of the amplitude

2.4.1 Physical states

Physical observables in gauge theory have to be independent of the choice of gauge, i.e. they must be gauge invariant under local gauge transformations. This also holds for the wave

[1] An irreducible representation of a group is a group representation with the lowest possible dimension (Appendix A)

functions of physical particles. Let $|\Omega\rangle$ denote the vacuum state of some gauge theory, being a gauge invariant physical state. It means that under a local gauge transformation $R_{\mu\nu}(\mathcal{G})$, and for any link $\{\mu\nu\}$ and any group element $\mathcal{G}$, this state behaves as

$$|\Omega, t\rangle \rightarrow \left|R_{\mu\nu}(\mathcal{G})\Omega, t\right\rangle = |\Omega, t\rangle \ . \tag{2.36}$$

Note that the operator $R_{\mu\nu}(\mathcal{G})$ is defined by its transformation of the state constructed by the link variable $U_{\mu\nu}$,

$$\left|R_{\mu\nu}(\mathcal{G})U_{mn}\right\rangle = \begin{cases} |\mathcal{G}\ U_{mn}\rangle & \text{if } \mu\nu = mn \\ \\ |U_{mn}\rangle & \text{if } \mu\nu \neq mn \ . \end{cases} \tag{2.37}$$

2.4.2 Gauge invariance of the transition amplitude between physical states

Here we would like to study the gauge invariance of the transition amplitude. For this purpose let us consider the vacuum-to-vacuum transition amplitude in LGT, that is

$$\langle \Omega, t = T | \ \Omega, t = 0\rangle \ . \tag{2.38}$$

As a consequence of the gauge invariance of the ground state, this amplitude is also invariant under local gauge transformations

$$\left\langle R_{\mu\nu}(\mathcal{G}')\ \Omega, t = T\right| R_{mn}(\mathcal{G})\ \Omega, t = 0\rangle = \langle \Omega, t = T | \ \Omega, t = 0\rangle \ , \tag{2.39}$$

for all links $\{\mu\nu\}$ and $\{mn\}$, as well as all group elements $\mathscr{G}$ and $\mathscr{G}'$. Expanding the vacuum-vacuum amplitude in terms of the lattice link states yields:

$$\begin{aligned}
&\left\langle R_{\mu\nu}(\mathscr{G}')\,\Omega, T\right| R_{mn}(\mathscr{G})\,\Omega, 0\rangle \\
&= \int dU' dU \left\langle R_{\mu\nu}(\mathscr{G}')\,\Omega\right| U', T\rangle \langle U', T|\, U, 0\rangle \langle U, 0|\, R_{mn}(\mathscr{G})\,\Omega\rangle \\
&= \int dU' dU \left\langle \Omega\right| U'_{12}, ..., \mathscr{G}'^{-1} U'_{\mu\nu}, ..., T\rangle \langle U', T|\, U, 0\rangle \left\langle U_{12}, ..., \mathscr{G}^{-1} U_{mn}, ..., 0\right| \Omega\rangle \\
&= \int [dU'_{12}...d(\mathscr{G}'^{-1}U'_{\mu\nu})...][dU_{12}...d(\mathscr{G}^{-1}U_{mn})...] \left\langle \Omega\right| U'_{12}, ..., \mathscr{G}'^{-1}U'_{\mu\nu}, ..., T\rangle \\
&\times \left\langle U'_{12}, ..., \mathscr{G}'\mathscr{G}'^{-1}U'_{\mu\nu}, ..., T\right| U_{12}...\mathscr{G}\mathscr{G}^{-1}U_{mn}..., 0\rangle \left\langle U_{12}, ..., \mathscr{G}^{-1}U_{mn}, ..., 0\right| \Omega\rangle \\
&= \int [dU'_{12}...d(\mathscr{U}'_{\mu\nu})...][dU_{12}...d(\mathscr{U}_{mn})...] \\
&\times \left\langle \Omega\right| U'_{12}, ..., U'_{\mu\nu}, ..., T\rangle \left\langle U'_{12}, ..., \mathscr{G}'U'_{\mu\nu}, ..., T\right| U_{12}...\mathscr{G}U_{mn}..., 0\rangle \langle U_{12}, ..., U_{mn}, ..., 0|\, \Omega\rangle\ .
\end{aligned} \tag{2.40}$$

On the other hand, due to the gauge invariance of the amplitude, this expression is equivalent to

$$\begin{aligned}
&\langle \Omega, T|\, \Omega, 0\rangle \\
&= \int dU' dU \langle \Omega|\, U', T\rangle \langle U', T|\, U, 0\rangle \langle U, 0|\, \Omega\rangle \\
&= \int [dU'_{12}...dU'_{\mu\nu}...][dU_{12}...dU_{mn}...] \\
&\times \left\langle \Omega\right| U'_{12}, ..., U'_{\mu\nu}, ..., T\rangle \left\langle U'_{12}, ..., U'_{\mu\nu}, ..., T\right| U_{12}...U_{mn}..., 0\rangle \langle U_{12}, ..., U_{mn}, ..., 0|\, \Omega\rangle\ .
\end{aligned} \tag{2.41}$$

Comparing the last two equations we conclude

$$\left\langle U'_{12}, ..., \mathscr{G}'U'_{\mu\nu}, ..., T\right| U_{12}...\mathscr{G}U_{mn}..., 0\rangle = \left\langle U'_{12}, ..., U'_{\mu\nu}, ..., T\right| U_{12}...U_{mn}..., 0\rangle\ , \tag{2.42}$$

which supports all links $\{\mu\nu, mn\}$ and all group elements $\mathscr{G}', \mathscr{G}$. This confirms that the amplitude

$$\left\langle U'_{12}, ..., U'_{\mu\nu}, ..., T\right| U_{12}...U_{mn}..., 0\rangle \tag{2.43}$$

is gauge invariant.

2.4.3 Gauge invariance of transition amplitudes expressed by path integral

Although the previous calculation is no rigorous proof, the result is correct if we express the amplitude by the path integral. It is remarkable that this is true, although the link states $|U, t = 0\rangle$ and $|U', t = T\rangle$ are not gauge invariant states.

Let us express the above amplitude in terms of the path integral

$$\langle U'_{12}, ..., T|\, U_{12}, ..., 0\rangle \;=\; \int [dU] \exp\left(-S[U]/\hbar\right)\Big|_{U,t=0}^{U',t=T} . \tag{2.44}$$

This amplitude is gauge invariant under local gauge transformation because of two properties; first, the Haar measure of the group integral dU is gauge invariant, and second, the Wilson action $S[U]$ is gauge invariant. According to this, the whole path integral must be invariant under gauge transformations.

Since the link states are not gauge invariant, so this means that the path integral carries out some projection onto the gauge invariant part. This addresses the Elitzur's theorem[109, 110]. According to this theorem, gauge variant operators have been vanishing expectation values. In other words, the vacuum expectation value of some operator $\hat{\mathcal{O}}$ follows

$$\langle \Omega, T|\, \hat{\mathcal{O}}\, |\Omega, 0\rangle \;=\; \langle \Omega, T|\, \hat{\mathcal{O}}_{\text{inv}}\, |\Omega, 0\rangle \;, \tag{2.45}$$

which means that only the projection of the operator onto its gauge invariant part survives, and the non-invariant part is projected to zero.

Gauge invariance of the transition amplitude of a 4-link (plaquette) state

Here, in some details, we examine the gauge invariance of Eq.(2.44), for the Abelian U(1) gauge theory. Let us consider a $2^2 \times 2$ lattice in (2 + 1)-D (see Fig.[2.2]). It contains two time slices at $t_{\text{in}} = 0$ and $t_{\text{fi}} = T = a_t$, where a_t is temporal lattice spacing. The Bargmann link states for such a lattice are characterized by

$$\begin{aligned} &\text{Initial state } (t = 0): \;\; |U_{\text{in}}\rangle \;=\; \left|U^{\text{in}}_{12}, U^{\text{in}}_{23}, U^{\text{in}}_{43}, U^{\text{in}}_{14}\right\rangle \\ &\text{Final state } (t = T): \;\; |U_{\text{fi}}\rangle \;=\; \left|U^{\text{fi}}_{12}, U^{\text{fi}}_{23}, U^{\text{fi}}_{43}, U^{\text{fi}}_{14}\right\rangle . \end{aligned} \tag{2.46}$$

Now, the transition amplitude can be written in the following form:

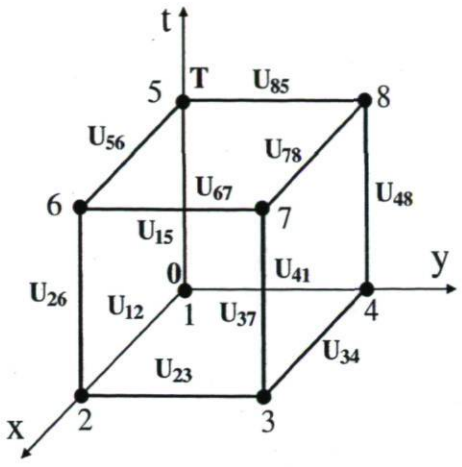

Figure 2.2: Schema of links in the lattice $2^2 \times 2$ in (2 + 1) dimensions.

$$\langle U_{\rm fi}, T|\, U_{\rm in}, 0\rangle$$

$$= \int [dU] \exp\left(-S[U]/\hbar\right)\Big|_{U_{\rm in},t=0}^{U_{\rm fi},t=T} = \int [dU_{15}dU_{26}dU_{37}dU_{48}]$$

$$\times \exp\Big\{ -\frac{1}{\hbar g^2}\Big(\Big[1 - Re(U_{12}^{\rm in}U_{23}^{\rm in}U_{34}^{\rm in}U_{41}^{\rm in})\Big] + \Big[1 - Re(U_{12}^{\rm in}U_{26}U_{56}^{\rm fi}U_{15})\Big] \tag{2.47}$$

$$+ \Big[1 - Re(U_{23}^{\rm in}U_{37}U_{67}^{\rm fi}U_{26})\Big] + \Big[1 - Re(U_{34}^{\rm in}U_{48}U_{78}^{\rm fi}U_{37})\Big]$$

$$+ \Big[1 - Re(U_{41}^{\rm in}U_{15}U_{85}^{\rm fi}U_{48})\Big] + \Big[1 - Re(U_{56}^{\rm fi}U_{67}^{\rm fi}U_{78}^{\rm fi}U_{85}^{\rm fi})\Big]\Big)\Big\}\,.$$

Note that the link variables with the indices "in" or "fi" correspond to the spatial links, while the rest correspond to the temporal links.

On the other hand, let us now consider the initial and final states after a local gauge transformation. A single link variable transforms according to

$$U_{\mu\nu} \to U_{\mu\nu}^{\mathcal{G}} = \mathcal{G}_\mu U_{\mu\nu}\mathcal{G}_\nu^{-1}\,. \tag{2.48}$$

Consequently, For the transformation of a Bargmann link state we have

$$|U_{12}, U_{23}, U_{43}, U_{14}\rangle \to \left|U_{12}^{\mathcal{G}}, U_{23}^{\mathcal{G}}, U_{43}^{\mathcal{G}}, U_{14}^{\mathcal{G}}\right\rangle = \left|\mathcal{G}_1 U_{12}\mathcal{G}_2^{-1}, \mathcal{G}_2 U_{23}\mathcal{G}_3^{-1}, \mathcal{G}_4 U_{43}\mathcal{G}_3^{-1}, \mathcal{G}_1 U_{14}\mathcal{G}_4^{-1}\right\rangle\,. \tag{2.49}$$

Thus, the initial and final Bargmann states after local gauge transformation are represented by

$$\begin{aligned} |U_{\rm in}\rangle \to \left|U_{\rm in}^{\mathcal{G}}\right\rangle &= \left|\mathcal{G}_1 U_{12}\mathcal{G}_2^{-1}, \mathcal{G}_2 U_{23}\mathcal{G}_3^{-1}, \mathcal{G}_4 U_{43}\mathcal{G}_3^{-1}, \mathcal{G}_1 U_{14}\mathcal{G}_4^{-1}\right\rangle \\ |U_{\rm fi}\rangle \to \left|U_{\rm fi}^{\mathcal{G}}\right\rangle &= \left|\mathcal{G}_5 U_{56}\mathcal{G}_6^{-1}, \mathcal{G}_6 U_{67}\mathcal{G}_7^{-1}, \mathcal{G}_8 U_{87}\mathcal{G}_7^{-1}, \mathcal{G}_5 U_{58}\mathcal{G}_8^{-1}\right\rangle\,. \end{aligned} \tag{2.50}$$

Hereby, for the transition amplitude between the gauge transformed Bargmann link states, we write

$$\left\langle U_{\mathrm{fi}}^{\mathscr{G}}, T \middle| U_{\mathrm{in}}^{\mathscr{G}}, 0 \right\rangle = \int [dU] \exp(-S[U]/\hbar) \Big|_{U_{\mathrm{in}}^{\mathscr{G}}, t=0}^{U_{\mathrm{fi}}^{\mathscr{G}}, t=T} = \int [dU_{15} dU_{26} dU_{37} dU_{48}]$$

$$\times \exp\Big\{ -\frac{1}{\hbar g^2} \Big(\Big[1 - Re(\mathscr{G}_1 U_{12}^{\mathrm{in}} \mathscr{G}_2^{-1}\ \mathscr{G}_2 U_{23}^{\mathrm{in}} \mathscr{G}_3^{-1}\ \mathscr{G}_3 U_{34}^{\mathrm{in}} \mathscr{G}_4^{-1}\ \mathscr{G}_4 U_{41}^{\mathrm{in}} \mathscr{G}_1^{-1}) \Big]$$

$$+ \Big[1 - Re(\mathscr{G}_1 U_{12}^{\mathrm{in}} \mathscr{G}_2^{-1}\ U_{26}\ \mathscr{G}_6 U_{65}^{\mathrm{fi}} \mathscr{G}_5^{-1}\ U_{51}) \Big] + \Big[1 - Re(\mathscr{G}_2 U_{23}^{\mathrm{in}} \mathscr{G}_3^{-1}\ U_{37}\ \mathscr{G}_7 U_{76}^{\mathrm{fi}} \mathscr{G}_6^{-1}\ U_{62}) \Big]$$

$$+ \Big[1 - Re(\mathscr{G}_3 U_{34}^{\mathrm{in}} \mathscr{G}_4^{-1}\ U_{48}\ \mathscr{G}_8 U_{87}^{\mathrm{fi}} \mathscr{G}_7^{-1}\ U_{73}) \Big] + \Big[1 - Re(\mathscr{G}_4 U_{41}^{\mathrm{in}} \mathscr{G}_1^{-1}\ U_{15}\ \mathscr{G}_5 U_{58}^{\mathrm{fi}} \mathscr{G}_8^{-1}\ U_{84}) \Big]$$

$$+ \Big[1 - Re(\mathscr{G}_5 U_{56}^{\mathrm{fi}} \mathscr{G}_6^{-1}\ \mathscr{G}_6 U_{67}^{\mathrm{fi}} \mathscr{G}_7^{-1}\ \mathscr{G}_7 U_{78}^{\mathrm{fi}} \mathscr{G}_8^{-1}\ \mathscr{G}_8 U_{85}^{\mathrm{fi}} \mathscr{G}_5^{-1}) \Big] \Big) \Big\} . \tag{2.51}$$

Remark that the first term in the exponent corresponds to the initial space-like plaquette, while the last term stands for the final space-like plaquette. The four middle terms represent the time-like plaquettes. Now, by introducing a variable transformation for all temporal links as

$$\begin{aligned}
\widetilde{U}_{26} &= \mathscr{G}_2^{-1} U_{26} \mathscr{G}_6 \Longleftrightarrow U_{26}^{\mathscr{G}} = \mathscr{G}_2 \widetilde{U}_{26} \mathscr{G}_6^{-1} \\
\widetilde{U}_{37} &= \mathscr{G}_3^{-1} U_{37} \mathscr{G}_7 \Longleftrightarrow U_{37}^{\mathscr{G}} = \mathscr{G}_3 \widetilde{U}_{37} \mathscr{G}_7^{-1} \\
\widetilde{U}_{48} &= \mathscr{G}_4^{-1} U_{48} \mathscr{G}_8 \Longleftrightarrow U_{48}^{\mathscr{G}} = \mathscr{G}_4 \widetilde{U}_{48} \mathscr{G}_8^{-1} \\
\widetilde{U}_{15} &= \mathscr{G}_1^{-1} U_{15} \mathscr{G}_5 \Longleftrightarrow U_{15}^{\mathscr{G}} = \mathscr{G}_1 \widetilde{U}_{15} \mathscr{G}_5^{-1} ,
\end{aligned} \tag{2.52}$$

we obtain

$$\left\langle U_{\mathrm{fi}}^{\mathscr{G}}, T \middle| U_{\mathrm{in}}^{\mathscr{G}}, 0 \right\rangle =$$

$$\int [d(\mathscr{G}_1 \widetilde{U}_{15} \mathscr{G}_5^{-1}) d(\mathscr{G}_2 \widetilde{U}_{26} \mathscr{G}_6^{-1}) d(\mathscr{G}_3 \widetilde{U}_{37} \mathscr{G}_7^{-1}) d(\mathscr{G}_4 \widetilde{U}_{48} \mathscr{G}_8^{-1})]$$

$$\times \exp\Big\{ -\frac{1}{\hbar g^2} \Big(\Big[1 - Re(U_{12}^{\mathrm{in}} U_{23}^{\mathrm{in}} U_{34}^{\mathrm{in}} U_{41}^{\mathrm{in}}) \Big] + \Big[1 - Re(U_{12}^{\mathrm{in}} \widetilde{U}_{26} U_{65}^{\mathrm{fi}} \widetilde{U}_{51}) \Big] \tag{2.53}$$

$$+ \Big[1 - Re(U_{23}^{\mathrm{in}} \widetilde{U}_{37} U_{76}^{\mathrm{fi}} \widetilde{U}_{62}) \Big] + \Big[1 - Re(U_{34}^{\mathrm{in}} \widetilde{U}_{48} U_{87}^{\mathrm{fi}} \widetilde{U}_{73}) \Big]$$

$$+ \Big[1 - Re(U_{41}^{\mathrm{in}} \widetilde{U}_{15} U_{58}^{\mathrm{fi}} \widetilde{U}_{84}) \Big] + \Big[1 - Re(U_{56}^{\mathrm{fi}} \widetilde{U}_{67}^{\mathrm{fi}} \widetilde{U}_{78}^{\mathrm{fi}} U_{85}^{\mathrm{fi}}) \Big] \Big) \Big\} .$$

Using the invariance property of the group measure

$$\begin{aligned} d(\mathcal{G}_1 \widetilde{U}_{15} \mathcal{G}_5^{-1}) &= d\widetilde{U}_{15} \\ \vdots \qquad\qquad & \quad \vdots \\ d(\mathcal{G}_4 \widetilde{U}_{48} \mathcal{G}_8^{-1}) &= d\widetilde{U}_{48} \end{aligned} \tag{2.54}$$

we find an expression identical to that given by Eq.(2.47), which proves the gauge invariance of the transition amplitude.

2.4.4 Gauge invariance of the transition amplitude expressed as time evolution under Hamiltonian

In this part, let us investigate the gauge transformation properties of transition amplitude expressed by the time evolution under Hamiltonian, that is

$$\langle \Psi' | \exp(-\mathcal{H}T/\hbar) | \Psi \rangle \ , \tag{2.55}$$

where $\mathcal{H}$ is the KS Hamiltonian (a gauge invariant operator). How the amplitude (2.55) transforms under local gauge transformations depends on the wave functions Ψ and Ψ'. If they are physical states (e.g. the vacuum state), then the propagator

$$\left\langle \Psi'_{\text{phys}} \right| \exp(-\mathcal{H}T/\hbar) \left| \Psi_{\text{phys}} \right\rangle \tag{2.56}$$

is gauge invariant. But on the contrary, if the states Ψ and Ψ' are not gauge invariant states, then the amplitude is not gauge invariant. In particular, this is the case for the Bargmann link states, i.e. the transition amplitude

$$\langle U' | \exp(-\mathcal{H}T/\hbar) | U \rangle \tag{2.57}$$

is not a gauge invariant object.

How can one create a gauge invariant transition amplitude?

We discuss this in analogy with quantum mechanics and rotational symmetry. Consider the matrix elements

$$\langle \Phi | \hat{\mathcal{O}} | \Phi \rangle \ , \tag{2.58}$$

where $\hat{\mathcal{O}}$ is assumed to be rotationally an invariant operator (it commutes with all generators $\hat{L}_i$ of the rotation group, like $\hat{\mathcal{O}} = \hat{L}^2$). On the other hand, let $|\Phi\rangle$ and $|\Phi'\rangle$ be rotationally

non-invariant states. Then the whole matrix element is non-invariant under rotations. Furthermore, the spherical harmonics $Y_{lm}(\theta, \phi)$ are rotationally non-invariant, except for $Y_{00}(\theta, \phi)$. This means that one has to make a projection onto the state $Y_{00}(\theta, \phi)$, such as

$$|\Phi\rangle \rightarrow |\Phi\rangle_{\text{inv}} = |Y_{00}\rangle \langle Y_{00}| \Phi\rangle \ . \tag{2.59}$$

The same thing can be expressed using the rotation group SO(3), elements $\mathcal{G} \in$ SO(3), as well as a representation $\mathcal{R}$ of the rotation group in Hilbert space defined by $\mathcal{G} \rightarrow \mathcal{R}(\mathcal{G})$. It reads as

$$\langle \mathcal{G}\vec{x}| \Phi\rangle = \left\langle \vec{x}\right| \mathcal{R}^{\dagger}(\mathcal{G})\Phi\Big\rangle \ . \tag{2.60}$$

Then one can construct a rotationally invariant state by integrating over the rotation group as

$$\langle \vec{x}| \Phi\rangle \rightarrow \langle \vec{x}| \Phi\rangle_{\text{inv}} = \Phi_{\text{inv}}(\vec{x}) = Z \int \mathrm{d}\mathcal{G}\Phi(\mathcal{G}\vec{x}) = Z \int \mathrm{d}\mathcal{G} \langle \mathcal{G}\vec{x}| \Phi\rangle = Z \int \mathrm{d}\mathcal{G} \left\langle \vec{x}\right| R^{\dagger}(\mathcal{G})\Phi\Big\rangle \ . \tag{2.61}$$

Since we look for a projection in such a way that no rotationally invariant state changes, the factor Z is related to the group volume as

$$Z = \frac{1}{V_{\text{group}}} = \frac{1}{4\pi} (\text{for rotations in 3-D space}) \ . \tag{2.62}$$

One can easily check that such construction yields a rotationally invariant state:

$$\langle \mathcal{G}'\vec{x}| \Phi_{\text{inv}}\rangle = Z \int \mathrm{d}\mathcal{G} \langle \mathcal{G}\mathcal{G}'\vec{x}| \Phi\rangle = Z \int \mathrm{d}(\mathcal{G}\mathcal{G}') \langle \mathcal{G}\mathcal{G}'\vec{x}| \Phi\rangle = Z \int \mathrm{d}\mathcal{G}'' \langle \mathcal{G}''\vec{x}| \Phi\rangle = \langle \vec{x}| \Phi\rangle \ , \tag{2.63}$$

where the invariance of the group measure has been used.

The above method can also be employed for the construction of a gauge invariant state of Bargmann link states. To this end, we make a gauge invariant state of a link state by

$$\left|U_{\mu\nu}\right\rangle \rightarrow \left|U^{\text{inv}}_{\mu\nu}\right\rangle = Z^2 \int d\mathcal{G}_{\mu} d\mathcal{G}_{\nu} \left|\mathcal{G}_{\mu} U_{\mu\nu} \mathcal{G}_{\nu}^{-1}\right\rangle \ . \tag{2.64}$$

(the prefactor Z is again related to the group measure of the gauge group: $Z = \frac{1}{V_{\text{group}}}$).

Likewise, a state composed of several links becomes invariant by

$$\begin{aligned} |U\rangle &= \left|U_{12}, U_{23}, ..., U_{N-1,N}\right\rangle \longrightarrow \\ \left|U^{\text{inv}}\right\rangle &= Z^N \int d\mathcal{G}_1 ... d\mathcal{G}_N \left|\mathcal{G}_1 U_{12} \mathcal{G}_2^{-1}, ..., \mathcal{G}_{N-1} U_{N-1,N} \mathcal{G}_N^{-1}\right\rangle \ . \end{aligned} \tag{2.65}$$

Now let us go back to the problem of how to obtain a gauge invariant transition amplitude between link states, under evolution of the Hamiltonian (as given by Eq.(2.57)).

According to the above discussion, we have:

$$\langle U'|\exp\left[-\mathcal{H}T/\hbar\right]|U\rangle \longrightarrow$$

$$\begin{aligned}
&\left\langle U'_{\text{inv}}\right|\exp\left[-\mathcal{H}T/\hbar\right]|U_{\text{inv}}\rangle \;=\; Z^N\int d\mathcal{G}'_1...d\mathcal{G}'_N\, Z^N\int d\mathcal{G}_1...d\mathcal{G}_N \\
&\times\left\langle \mathcal{G}'_1U'_{12}\mathcal{G}'^{-1}_2,...,\mathcal{G}'_{N-1}U'_{N-1,N}\mathcal{G}'^{-1}_N\right|\exp\left[-\mathcal{H}T/\hbar\right]\left|\mathcal{G}_1U_{12}\mathcal{G}_2^{-1},...,\mathcal{G}_{N-1}U_{N-1,N}\mathcal{G}_N^{-1}\right\rangle \\
&Z^N\int d\mathcal{G}_1...d\mathcal{G}_N\left\langle U'_{12},...,U'_{N-1,N}\right|\exp\left[-\mathcal{H}T/\hbar\right]\left|\mathcal{G}_1U_{12}\mathcal{G}_2^{-1},...,\mathcal{G}_{N-1}U_{N-1,N}\mathcal{G}_N^{-1}\right\rangle .
\end{aligned} \tag{2.66}$$

The last equation follows the fact that the mapping from a Bargmann state to the gauge invariant state is led by a projection operator. Any projection $\hat{P}$ commutes with the Hamiltonian, and also it satisfies: $\hat{P}^2 = \hat{P}$.

2.4.5 Comparison of the path integral with the evolution under Hamiltonian

We have shown the gauge invariance of the amplitude between link states expressed in terms of the path integral

$$\langle U_{\text{fi}}, T|\, U_{\text{in}}, 0\rangle \;=\; \int [dU]\exp\left(-S[U]/\hbar\right)\Big|_{U_{\text{in}},t=0}^{U_{\text{fi}},t=T}. \tag{2.67}$$

and the gauge invariance of transition amplitude, expressed in terms of evolution under the Hamiltonian between gauge invariant projected Bargmann states

$$\left\langle U^{\text{inv}}_{\text{fi}}\right|\exp\left[-\mathcal{H}T/\hbar\right]\left|U^{\text{inv}}_{\text{in}}\right\rangle . \tag{2.68}$$

Now the question is: do both expression give the same results? The response to this question is "yes", meaning that

$$\left\langle U^{\text{inv}}_{\text{fi}}\right|\exp\left[-\mathcal{H}T\right]\left|U^{\text{inv}}_{\text{in}}\right\rangle \;=\; \int [dU]\exp\left(-S[U]/\hbar\right)\Big|_{U_{in},t=0}^{U_{\text{fi}},t=T}. \tag{2.69}$$

Kröger et al. [111] through a high precision numerical simulation for the Abelian U(1) LGT, indicated that both amplitudes are in agreement. However, it should be pointed out that in LGT, it is customary to identify the measure $[dU]$ in Eq.(2.69) with the Haar measure of the gauge group. In fact, this is not quite correct, as there is some normalization factor missing. Such normalization factor, however, is canceled out when computing ratios of path integrals by means of the Monte Carlo method with importance sampling. Nevertheless, if the path integral stands alone, such normalization factor needs to be taken into account. In the case of U(1) LGT, such normalization factor has been computed in Ref. [111].

2.5 Gauge projection of the Bargmann link states via group integral

In this section, we would like to see how a scalar product of Bargmann link states transforms under gauge projection. To this aim, we work on a few examples for the transition times zero and T.

2.5.1 Gauge projection of the amplitude for transition time $T = 0$

(a) Single plaquette:

Let us consider a 2D spatial lattice containing only one plaquette (see Fig.[2.3]). In this case,

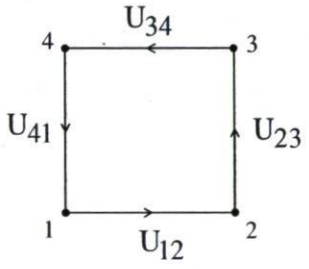

Figure 2.3: Spatial lattice in 2 dimensions including one plaquette.

the Bargmann link state is given by

$$|U\rangle = |U_{12}, U_{23}, U_{34}, U_{41}\rangle \ . \tag{2.70}$$

Now we parameterize link variables as $U_{\mu\nu} = \exp[i\alpha_{\mu\nu}]$ and a group element at node μ as $\mathcal{G}_\mu = \exp[i\beta_\mu]$. Hence, for the gauge projection of this Bargmann state, we have

$$|U_{\text{inv}}\rangle = \int_0^{2\pi} \frac{d\beta_1}{2\pi} \dots \int_0^{2\pi} \frac{d\beta_4}{2\pi} \left| e^{i(\alpha_{12}+\beta_1-\beta_2)}, e^{i(\alpha_{23}+\beta_2-\beta_3)}, e^{i(\alpha_{34}+\beta_3-\beta_4)}, e^{i(\alpha_{41}+\beta_4-\beta_1)} \right\rangle \ . \tag{2.71}$$

Therefore, the scalar product between gauge-projected Bargmann link states of this system is obtained as

$$\begin{aligned}
&\langle U'_{\text{inv}}|\, U_{\text{inv}}\rangle = \int_0^{2\pi}\frac{d\beta_1}{2\pi}\cdots\int_0^{2\pi}\frac{d\beta_4}{2\pi} \\
&\times\left\langle e^{i\alpha'_{12}}, e^{i\alpha'_{23}}, e^{i\alpha'_{34}}, e^{i\alpha'_{41}}\right| e^{i(\alpha_{12}+\beta_1-\beta_2)}, e^{i(\alpha_{23}+\beta_2-\beta_3)}, e^{i(\alpha_{34}+\beta_3-\beta_4)}, e^{i(\alpha_{41}+\beta_4-\beta_1)}\Big\rangle \\
&= \int\frac{d\beta_1}{2\pi}\cdots\int\frac{d\beta_4}{2\pi}\times 2\pi\delta\left[\alpha'_{12}-(\alpha_{12}+\beta_1-\beta_2)\right]\times 2\pi\delta\left[\alpha'_{23}-(\alpha_{23}+\beta_2-\beta_3)\right] \\
&\times 2\pi\,\delta\left[\alpha'_{34}-(\alpha_{34}+\beta_3-\beta_4)\right]\times\ 2\pi\,\delta\left[\alpha'_{41}-(\alpha_{41}+\beta_4-\beta_1)\right] \\
&= 2\pi\,\delta[(\alpha'_{12}+\alpha'_{23}+\alpha'_{34}+\alpha'_{41})-(\alpha_{12}+\alpha_{23}+\alpha_{34}+\alpha_{41})] \\
&= 2\pi\,\delta(\alpha'_P-\alpha_P)\ =\ \delta(U'_P-U_P)\ =\ \langle U'_P|\, U_P\rangle\ ,
\end{aligned} \tag{2.72}$$

where the parameter

$$\alpha_P = \alpha_{12}+\alpha_{23}+\alpha_{34}+\alpha_{41} \tag{2.73}$$

denotes the plaquette angle variable, which corresponds to the plaquette

$$U_P = U_{12}U_{23}U_{34}U_{41}\ . \tag{2.74}$$

(b) Four plaquettes:

Another example is a 2D spatial lattice, including four plaquettes (Fig.[2.4]). The Bargmann

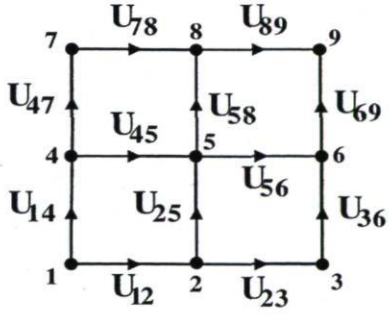

Figure 2.4: Spatial 2D lattice including four plaquettes.

link states of this system are presented by

$$\begin{aligned}
|U\rangle\ &=\ |U_{12}, U_{23}, U_{45}, U_{56}, U_{78}, U_{89}, U_{14}, U_{25}, U_{36}, U_{47}, U_{58}, U_{69}\rangle\ , \\
|U'\rangle\ &=\ \left|U'_{12}, U'_{23}, U'_{45}, U'_{56}, U'_{78}, U'_{89}, U'_{14}, U'_{25}, U'_{36}, U'_{47}, U'_{58}, U'_{69}\right\rangle\ .
\end{aligned} \tag{2.75}$$

Again via a gauge projection one finds

$$\begin{aligned}
&\left\langle U'_{\text{inv}} \right| U_{\text{inv}} \rangle \\
&= \delta(U'_{P_1} - U_{P_1}) \times \delta(U'_{P_2} - U_{P_2}) \\
&\times \delta(U'_{P_3} - U_{P_3}) \times \delta(U'_{P_4} - U_{P_4}) \\
&= \left\langle U'_{P_1}, U'_{P_2}, U'_{P_3}, U'_{P_4} \right| U_{P_1}, U_{P_2}, U_{P_3}, U_{P_4} \rangle \ .
\end{aligned} \tag{2.76}$$

(c) N plaquettes:

From the above results, one can obtain a general consequence for a 2D lattice of the size $N_x \times N_y$ or a 3D lattice of the size $N_x \times N_y \times N_z$. It is given by

$$\langle U'_{\text{inv}} | U_{\text{inv}} \rangle = \left\langle U'_{P_1}, ..., U'_{P_N} \right| U_{P_1}, ..., U_{P_N} \rangle = \prod_{k=1}^{N} \delta \left[U'_{P_k} - U_{P_k} \right] . \tag{2.77}$$

As a conclusion we find that after gauge projection, the scalar product of Bargmann link states (which is identical to the transition amplitude for $T = 0$), is equal to the scalar product of Bargmann plaquette states (over all possible plaquettes).

2.5.2 Gauge projection of transition amplitude for the finite transition time T

Now we would like to see how the transition amplitude between Bargmann link states under Hamiltonian evolution, becomes gauge invariant under the operation of the group integral in U(1) LGT (See Eq.(2.66) again).

(i) Single plaquette:

First we consider a 4-link state (plaquette) presented in Fig.[2.2]. In order to obtain the transition amplitude of a single plaquette, we return to the amplitude of transition for one

link state, given by Eq.(2.27), and similarly we find:

$$\begin{aligned}&\left\langle U'_{12}, U'_{23}, U'_{43}, U'_{14}\right| \exp\left[-\mathcal{H}^{\text{elec}} T/\hbar\right] |U_{12}, U_{23}, U_{43}, U_{14}\rangle \\ &= \prod_{\{\mu\nu=12,23,43,14\}} \left(\sum_{n_{\mu\nu}=0,\pm1,\pm2,\ldots} \exp\left[-\frac{g^2\hbar T}{2a_s} n_{\mu\nu}^2\right] \cos\left[n_{\mu\nu}(\alpha'_{\mu\nu} - \alpha_{\mu\nu})\right]\right).\end{aligned} \tag{2.78}$$

According to Eq.(2.66), we carry out the group integral $\int d\mathcal{G}_\mu = \frac{1}{2\pi}\int_0^{2\pi} d\beta_\mu$ at the lattice sites $\{\mu = 1, 2, 3, 4\}$ to enforce the gauge invariance property on the amplitude. To this end, we write

$$\begin{aligned}\langle U'_{\text{inv}}| \exp\left[-\mathcal{H}^{\text{elec}} T/\hbar\right] |U_{\text{inv}}\rangle &= \left(\frac{1}{2\pi}\right)^4 \int_0^{2\pi} d\beta_1 \ldots \int_0^{2\pi} d\beta_4 \\ \prod_{\{\mu\nu=12,23,43,14\}} \left(\sum_{n_{\mu\nu}=0,\pm1,\pm2,\ldots} \right. &\left. \times \exp\left[-\frac{g^2\hbar T}{2a_s} n_{\mu\nu}^2\right] \cos\left[n_{\mu\nu}(\alpha'_{\mu\nu} - (\alpha_{\mu\nu} + \beta_\mu - \beta_\nu))\right]\right).\end{aligned} \tag{2.79}$$

Here we remark that, there is an infinite sum over $n_{\mu\nu}$ corresponding to different irreducible representations. Due to the exponential factor $\exp\left[-\frac{g^2\hbar T}{2a_s} n_{\mu\nu}^2\right]$, such summation rapidly does converge. Depending on the transition time T, by starting from $n_{\mu\nu} = 0$ only a few terms will be sufficient to obtain a reliable precision. Nevertheless, such values of $n_{\mu\nu}$ will create a huge number of terms, which turn out to be closed loop diagrams.

Now, we expand the product in Eq.(2.79) and obtain

$$\begin{aligned}\langle U'_{\text{inv}}| \exp\left[-\mathcal{H}^{\text{elec}} T/\hbar\right] |U_{\text{inv}}\rangle &= \left(\frac{1}{2\pi}\right)^4 \int_0^{2\pi} d\beta_1 \ldots \int_0^{2\pi} d\beta_4 \\ &\times \sum_{n_{12}=0,\pm1,\pm2,\ldots} \exp\left[-\frac{g^2\hbar T}{2a_s} n_{12}^2\right] \cos\left[n_{12}(\alpha'_{12} - \alpha_{12} - \beta_1 + \beta_2)\right] \\ &\times \sum_{n_{23}=0,\pm1,\pm2,\ldots} \exp\left[-\frac{g^2\hbar T}{2a_s} n_{23}^2\right] \cos\left[n_{23}(\alpha'_{23} - \alpha_{23} - \beta_2 + \beta_3)\right] \\ &\times \sum_{n_{43}=0,\pm1,\pm2,\ldots} \exp\left[-\frac{g^2\hbar T}{2a_s} n_{43}^2\right] \cos\left[n_{43}(\alpha'_{43} - \alpha_{43} - \beta_4 + \beta_3)\right] \\ &\times \sum_{n_{14}=0,\pm1,\pm2,\ldots} \exp\left[-\frac{g^2\hbar T}{2a_s} n_{14}^2\right] \cos\left[n_{14}(\alpha'_{14} - \alpha_{14} - \beta_1 + \beta_4)\right] .\end{aligned} \tag{2.80}$$

Using the orthogonality of trigonometric functions

$$\frac{1}{2\pi}\int_0^{2\pi} d\beta \cos\left[n(\beta + \theta)\right] \cos\left[m(\beta + \phi)\right] = \cos\left[n\theta + m\phi\right] \delta_{m+n,0} \tag{2.81}$$

and integrating over β_1 and β_3, we have:

$$\langle U'_{\rm inv}|\exp\left[-\mathcal{H}^{\rm elec}T/\hbar\right]|U_{\rm inv}\rangle = \left(\frac{1}{2\pi}\right)^2\int_0^{2\pi}d\beta_2\int_0^{2\pi}d\beta_4$$
$$\times\sum_{n=0,\pm1,\pm2,\ldots}\exp\left[-\frac{g^2\hbar T}{2a_s}2n^2\right]\cos\Big(n\left[\alpha'_{12}-\alpha_{12}-(\alpha'_{14}-\alpha_{14})+\beta_2-\beta_4\right]\Big) \tag{2.82}$$
$$\times\sum_{m=0,\pm1,\pm2,\ldots}\exp\left[-\frac{g^2\hbar T}{2a_s}2m^2\right]\cos\Big(m\left[\alpha'_{23}-\alpha_{23}-(\alpha'_{43}-\alpha_{43})-\beta_2+\beta_4\right]\Big).$$

Finally, the integrating over β_2 and β_4 yields

$$\langle U'_{\rm inv}|\exp\left[-\mathcal{H}^{\rm elec}T/\hbar\right]|U_{\rm inv}\rangle$$
$$=\sum_{n=0,\pm1,\pm2,\ldots}\exp\left[-\frac{g^2\hbar T}{2a_s}4n^2\right]\cos\Big(n\left[\alpha'_{12}-\alpha_{12}-(\alpha'_{14}-\alpha_{14})+\alpha'_{23}-\alpha_{23}-(\alpha'_{43}-\alpha_{43})\right]\Big)$$
$$=\sum_{n=0,\pm1,\pm2,\ldots}\exp\left[-\frac{g^2\hbar T}{2a_s}4n^2\right]\cos\Big(n\left[\alpha'_{12}+\alpha'_{23}-\alpha'_{43}-\alpha'_{14}-\alpha_{12}-\alpha_{23}+\alpha_{43}+\alpha_{14}\right]\Big). \tag{2.83}$$

From the relation $U_{\mu\nu} = U^{-1}_{\mu\nu}$ one can conclude that $\alpha_{\mu\nu} = -\alpha_{\nu\mu}$. Now by considering this property and using Kronecker δ-function, we can represent Eq.(2.83) in the following form:

$$\langle U'_{\rm inv}|\exp\left[-\mathcal{H}^{\rm elec}T/\hbar\right]|U_{\rm inv}\rangle = \sum_{n_{12}=0,\pm1,\ldots}\sum_{n_{23}=0,\pm1,\ldots}\sum_{n_{41}=0,\pm1,\ldots}\sum_{n_{34}=0,\pm1,\ldots}$$
$$\times\delta_{n_{12},n_{23}}\,\delta_{n_{23},n_{34}}\,\delta_{n_{34},n_{41}}\,\delta_{n_{41},n_{12}}\exp\left[-\frac{g^2\hbar T}{2a_s}(n_{12}^2+n_{23}^2+n_{41}^2+n_{34}^2)\right] \tag{2.84}$$
$$\times\cos\Big(n_{12}\left[\alpha'_{12}-\alpha_{12}\right]+n_{23}\left[\alpha'_{23}-\alpha_{23}\right]+n_{34}\left[\alpha'_{34}-\alpha_{34}\right]+n_{41}\left[\alpha'_{41}-\alpha_{41}\right]\Big).$$

The message of δ-functions for plaquette vertices is that the number of incoming links is the

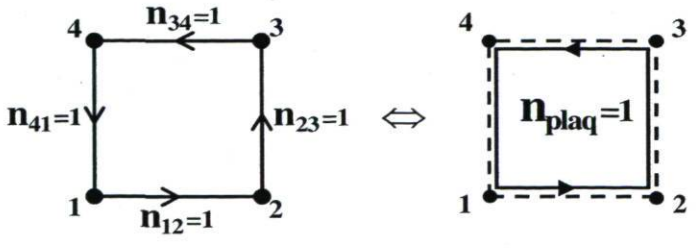

Figure 2.5: The Gauss' law for one plaquette. The number of incoming links is equal to the number of outgoing links at each lattice node.

same as the number of outgoing links (see Fig.[2.5]). Actually, this is the lattice form of the Gauss' law, $\vec{\nabla}.\vec{E} = 0$, in each vertex, and in the absence of charges (fermions) on the lattice sites. In fact, the Gauss' law on the lattice denotes the gauge invariance of lattice states. We enforced this property by performing group integral at all vertices, confirming that it is equivalent to the standard method of constructing gauge invariant states.

Now from Eq.(2.83) and considering the plaquette angle α_P, defined by Eq.(2.73), the temporal transition amplitude of one plaquette is determined by

$$\langle U'_{\text{inv}} | \exp\left[-\mathcal{H}^{\text{elec}} T/\hbar\right] | U_{\text{inv}} \rangle = \sum_{n=0,\pm1,\pm2,\ldots} \exp\left[-\frac{g^2\hbar T}{2a_s} 4n^2\right] \cos\left[n\Delta\alpha_P\right] , \tag{2.85}$$

where $\Delta\alpha_P = \alpha'_P - \alpha_P$. Here $4n^2$ corresponds to the contribution of n elementary loops (plaquettes) on top of each other (n^2 characterizes the eigenvalue of the electric field $\hat{\mathbf{E}}^2$).

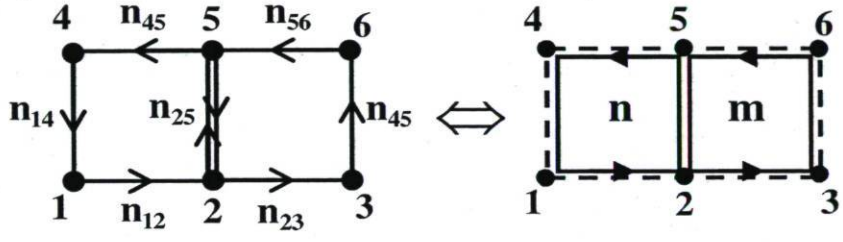

Figure 2.6: Scheme of the Gauss' law in a 2D lattice including two plaquettes.

(ii) Two plaquettes:

Now, as another example we calculate the electric transition amplitude for a lattice of two plaquettes (as shown in Fig.[2.6]). In this case, a Bargmann link state is defined by

$$|U\rangle = |U_{12}, U_{23}, U_{45}, U_{56}, U_{14}, U_{25}, U_{36}\rangle \ . \tag{2.86}$$

The gauge projected transition amplitude is given by

$$\left\langle U'_{\rm inv}\right| \exp\left[-\mathcal{H}^{\rm elec}T/\hbar\right] |U_{\rm inv}\rangle \;=\; \left(\tfrac{1}{2\pi}\right)^6 \int_0^{2\pi} d\beta_1 \;\ldots\; \int_0^{2\pi} d\beta_6$$

$$\times \sum_{n_{12}=0,\pm1,\pm2,\ldots} \exp\left[-\frac{g^2\hbar T}{2a_s} n_{12}^2\right] \cos\left[n_{12}(\Delta\alpha_{12} - \beta_1 + \beta_2)\right] \quad \text{(term 1)}$$

$$\times \sum_{n_{14}=0,\pm1,\pm2,\ldots} \exp\left[-\frac{g^2\hbar T}{2a_s} n_{14}^2\right] \cos\left[n_{14}(\Delta\alpha_{14} - \beta_1 + \beta_4)\right] \quad \text{(term 2)}$$

$$\times \sum_{n_{45}=0,\pm1,\pm2,\ldots} \exp\left[-\frac{g^2\hbar T}{2a_s} n_{45}^2\right] \cos\left[n_{45}(\Delta\alpha_{45} - \beta_4 + \beta_5)\right] \quad \text{(term 3)}$$

$$\times \sum_{n_{23}=0,\pm1,\pm2,\ldots} \exp\left[-\frac{g^2\hbar T}{2a_s} n_{23}^2\right] \cos\left[n_{23}(\Delta\alpha_{23} - \beta_2 + \beta_3)\right] \quad \text{(term 4)} \qquad (2.87)$$

$$\times \sum_{n_{36}=0,\pm1,\pm2,\ldots} \exp\left[-\frac{g^2\hbar T}{2a_s} n_{36}^2\right] \cos\left[n_{36}(\Delta\alpha_{36} - \beta_3 + \beta_6)\right] \quad \text{(term 5)}$$

$$\times \sum_{n_{56}=0,\pm1,\pm2,\ldots} \exp\left[-\frac{g^2\hbar T}{2a_s} n_{56}^2\right] \cos\left[n_{56}(\Delta\alpha_{56} - \beta_5 + \beta_6)\right] \quad \text{(term 6)}$$

$$\times \sum_{n_{25}=0,\pm1,\pm2,\ldots} \exp\left[-\frac{g^2\hbar T}{2a_s} n_{25}^2\right] \cos\left[n_{25}(\Delta\alpha_{25} - \beta_2 + \beta_5)\right] \quad \text{(term 7)}\,,$$

where $\Delta\alpha_{ij} = \alpha'_{ij} - \alpha_{ij}$.

Considering two first terms, integrating over $d\beta_1$, and using Eq.(2.81) during this procedure, one finds

$$\frac{1}{2\pi}\int_0^{2\pi} d\beta_1 \sum_{n_{12}=0,\pm1,\pm2,\ldots} \sum_{n_{14}=0,\pm1,\pm2,\ldots} \exp\left[-\frac{g^2\hbar T}{2a_s}(n_{12}^2 + n_{14}^2)\right]$$

$$\cos\left[n_{12}(\Delta\alpha_{12} - \beta_1 + \beta_2)\right] \cos\left[n_{14}(\Delta\alpha_{14} - \beta_1 + \beta_4)\right]$$

$$= \sum_{n_{12}=0,\pm1,\pm2,\ldots} \sum_{n_{14}=0,\pm1,\pm2,\ldots} \exp\left[-\frac{g^2\hbar T}{2a_s}(n_{12}^2 + n_{14}^2)\right] \cos\left[n_{12}(\Delta\alpha_{12} + \beta_2) + n_{14}(\Delta\alpha_{14} + \beta_4)\right]$$

$$\times\, \delta_{n_{12}+n_{14},0} \;=\; \sum_{n_1=0,\pm1,\pm2,\ldots} \exp\left[-\frac{g^2\hbar T}{2a_s} 2n_1^2\right] \cos\left[n(-\Delta\alpha_{12} + \Delta\alpha_{14} - \beta_2 + \beta_4)\right]\,, \qquad (2.88)$$

where due to the factor $\delta_{n_{12}+n_{14},0}$ we have defined $n_{12} = -n_{14} = n$.

The parameter β_4 is shared between the above result and the third term in Eq.(2.87). Hence, by multiplying the "term 3" by the last result of Eq.(2.88), and integrating over $d\beta_4$ we find

$$\left(\frac{1}{2\pi}\right)^2 \int_0^{2\pi} d\beta_4 \sum_{n=0,\pm1,\pm2,\ldots} \sum_{n_{45}=0,\pm1,\pm2,\ldots} \exp\left[-\frac{g^2\hbar T}{2a_s}(2n^2 + n_{45}^2)\right]$$

$$\cos\left[n(-\Delta\alpha_{12} + \Delta\alpha_{14} - \beta_2 + \beta_4)\right] \cos\left[n_{45}(\Delta\alpha_{45} - \beta_4 + \beta_5)\right]$$

$$= \sum_{n=0,\pm1,\pm2,\ldots} \sum_{n_{45}=0,\pm1,\pm2,\ldots} \exp\left[-\frac{g^2\hbar T}{2a_s}(2n^2 + n_{45}^2)\right] \tag{2.89}$$

$$\cos\left[n(-\Delta\alpha_{12} + \Delta\alpha_{14} - \beta_2 + \beta_4) + n_{45}(\Delta\alpha_{45} - \beta_4 + \beta_5)\right] \times \delta_{n+n_{45},0}$$

$$= \sum_{n=0,\pm1,\pm2,\ldots} \exp\left[-\frac{g^2\hbar T}{2a_s}3n^2\right] \cos\left[n(-\Delta\alpha_{12} + \Delta\alpha_{14} + \Delta\alpha_{45} - \beta_2 + \beta_5)\right] .$$

In this step, the integration over the first three terms of Eq.(2.87) is summarized as

$$A = \sum_{n=0,\pm1,\pm2,\ldots} \exp\left[-\frac{g^2\hbar T}{2a_s}3n^2\right] \cos\left[n(-\Delta\alpha_{12} + \Delta\alpha_{14} + \Delta\alpha_{45} - \beta_2 + \beta_5)\right] . \tag{2.90}$$

Again, considering the forth, the fifth and the sixth terms in Eq.(2.87), and performing a similar approach (as done for the first three terms), we obtain

$$B = \sum_{m=0,\pm1,\pm2,\ldots} \exp\left[-\frac{g^2\hbar T}{2a_s}3m^2\right] \cos\left[m(-\Delta\alpha_{23} + \Delta\alpha_{36} - \Delta\alpha_{56} - \beta_2 + \beta_5)\right] . \tag{2.91}$$

Now, we multiply Eqs.(2.90,2.91) by the seventh term in Eq.(2.87), and integrate over $d\beta_2$ and $d\beta_5$ as follows:

$$\left(\frac{1}{2\pi}\right)^2 \int_0^{2\pi} d\beta_2 \int_0^{2\pi} d\beta_5 \sum_{n,m,k=0,\pm1,\pm2,\ldots} \exp\left[-\frac{g^2\hbar T}{2a_s}(3n^2 + 3m^2 + k^2)\right]$$
$$\cos\left[n(\psi - \beta_2 + \beta_5)\right] \cos\left[m(\xi - \beta_2 + \beta_5)\right] \cos\left[k(\omega - \beta_2 + \beta_5)\right] , \tag{2.92}$$

where,

$$\psi = -\Delta\alpha_{12} + \Delta\alpha_{14} + \Delta\alpha_{45} \ , \ \xi = -\Delta\alpha_{23} + \Delta\alpha_{36} - \Delta\alpha_{56} \ , \ \omega = -\Delta\alpha_{25} \ , \ k = n_{25} . \tag{2.93}$$

In order to do the remaining integrations, we use the following orthogonality relation of trigonometric functions

$$\frac{1}{2\pi} \int_0^{2\pi} d\beta \cos\left[n(\beta + \psi)\right] \cos\left[m(\beta + \xi)\right] \cos\left[k(\beta + \omega)\right] = \cos\left[n\psi + m\xi + k\omega\right] \delta_{m+n+k,0} . \tag{2.94}$$

Therefore, the result for the transition amplitude is:

$$\begin{aligned}
&\langle U'_{\text{inv}}| \exp\left[-\mathcal{H}^{\text{elec}} T/\hbar\right] |U_{\text{inv}}\rangle \\
&= \sum_{n,m,k=0,\pm1,\pm2,\ldots} \exp\left[-\frac{g^2\hbar T}{2a_s}(3n^2+3m^2+k^2)\right] \cos\left[n\psi + m\xi + k\omega\right]\ \delta_{m+n+k,0} \\
&= \exp\left[-\frac{g^2\hbar T}{2a_s}(3n^2+3m^2+(n+m)^2)\right] \cos\left[n(\psi-\omega)+m(\xi-\omega)\right] .
\end{aligned} \tag{2.95}$$

Replacing the definition of angles in Eq.(2.93), and considering the plaquette angles

$$\alpha_{P_1} = \alpha_{12} + \alpha_{25} - \alpha_{45} - \alpha_{14}\ ,\ \alpha_{P_2} = \alpha_{23} + \alpha_{36} - \alpha_{56} - \alpha_{25} \tag{2.96}$$

we find

$$\begin{aligned}
&\langle U'_{\text{inv}}| \exp\left[-\mathcal{H}^{\text{elec}} T/\hbar\right] |U_{\text{inv}}\rangle \\
&= \sum_{n,m=0,\pm1,\pm2,\ldots} \exp\left[-\frac{g^2\hbar T}{2a_s}(3n^2+3m^2+(n+m)^2)\right] \cos\left[n\Delta\alpha_{P_1} - m\Delta\alpha_{P_2}\right] .
\end{aligned} \tag{2.97}$$

And as the final result for the transition amplitude of two adjacent plaquette with a common link, we have

$$\begin{aligned}
&\langle U'_{\text{inv}}| \exp\left[-\mathcal{H}^{\text{elec}} T/\hbar\right] |U_{\text{inv}}\rangle \\
&= \sum_{n,m=0,\pm1,\pm2,\ldots} \exp\left[-\frac{g^2\hbar T}{2a_s}(3n^2+3m^2+(n-m)^2)\right] \cos\left[n\Delta\alpha_{P_1} + m\Delta\alpha_{P_2}\right] .
\end{aligned} \tag{2.98}$$

From the above calculations, one can see that, the group integrals at each lattice vertex generates a Kronecker δ-function, so that the number of incoming links is equivalent to the number of outgoing links at each site. This is again a manifestation of gauge invariance, expressed in terms of the Gauss' law in lattice.

(iii) Four plaquettes:

Likewise the above calculations, for a lattice including four plaquettes (as shown in Fig.[2.7]) one obtains

$$\left\langle U'_{\text{inv}}\right| \exp\left[-\mathcal{H}^{\text{elec}}T/\hbar\right] |U_{\text{inv}}\rangle \;=\; \sum_{n_1=0,\pm1,\ldots} \sum_{n_2=0,\pm1,\ldots} \sum_{n_3=0,\pm1,\ldots} \sum_{n_4=0,\pm1,\ldots}$$

$$\exp\Big[-\frac{g^2\hbar T}{2a_s}\left[2n_1^2 + 2n_2^2 + 2n_3^2 + 2n_4^2 + (n_1-n_2)^2 + (n_1-n_3)^2 + (n_2-n_4)^2 + (n_3-n_4)^2\right]\Big]$$

$$\times\cos\left[n_1\Delta\alpha_{P_1} + n_2\Delta\alpha_{P_2} + n_3\Delta\alpha_{P_3} + n_4\Delta\alpha_{P_4}\right] . \tag{2.99}$$

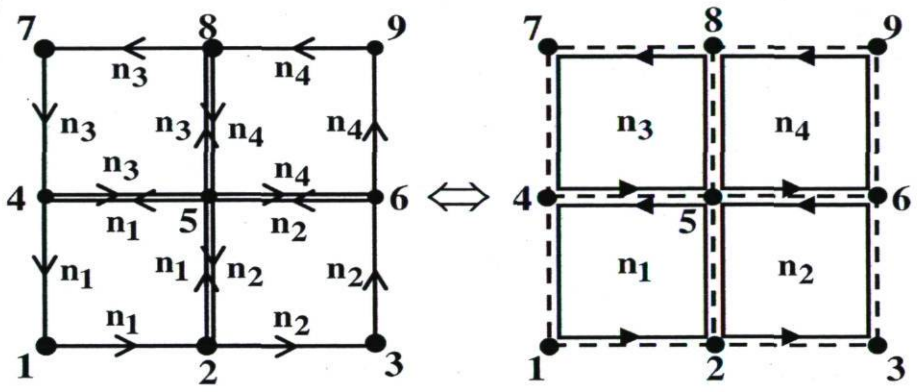

Figure 2.7: Scheme of the Gauss' law in a 2D lattice including four plaquettes.

(iv) N plaquettes:

For the general case, we conjecture the gauge projected transition amplitude for a 2D spatial lattice of the size $N_x \times N_y$ (i.e. including $N = N_xN_y$ plaquettes) to be of the following form:

$$\left\langle U'_{\text{inv}}\right| \exp\left[-\mathcal{H}^{\text{elec}}T/\hbar\right] |U_{\text{inv}}\rangle \;=\; \sum_{n_1=0,\pm1,\pm2,\ldots} \cdots \sum_{n_N=0,\pm1,\pm2,\ldots} \tag{2.100}$$

$$\exp\Big[-\frac{g^2\hbar T}{2a_s}\vec{E}^2_{\text{graph}}\Big] \times \cos[\vec{n}\cdot\vec{\Delta\alpha}_P] ,$$

where $\vec{n}.\vec{\Delta\alpha}_P = n_1\Delta\alpha_{P_1} + \ldots + n_N\Delta\alpha_{P_N}$. Moreover, the factor $\vec{E}^2_{\text{graph}}$ denotes the eigenvalue of the electric field operator of the graph, constructed from plaquettes filling the lattice, each with counter-clockwise orientation.

2.5.3 Gauge projection of transition amplitude from group theory point of view

Now let us interpret the gauge projection of the transition amplitude from the group theory point of view. According to the Peter-Weyl theorem [108], a matrix element of an operator function $f(\hat{C})$ is expressed by

$$\langle \mathscr{G} | f(\hat{C}) | \mathscr{G}' \rangle = \sum_{\nu} |\nu| \, f(C_\nu) \chi^{\{\nu\}}(\mathscr{G}^{-1}\mathscr{G}') \,, \tag{2.101}$$

where $\mathscr{G}$ and $\mathscr{G}'$ are group elements, $\hat{C}$ is the quadratic Casimir operator with the eigenvalues C_ν in the irreducible representation $\{\nu\}$, and $\chi^{\{\nu\}}(\mathscr{G})$ denotes the group character. In other words, this theorem says that it does not matter if $\mathscr{G}$ and $\mathscr{G}'$ denote link variables or plaquette variables. Thus the analytic result obtained previously for transition amplitude between Bargmann link states, must also hold for Bargmann plaquette states. Here we summarize the above conclusions in the following expressions:

- Transition amplitude for a single link Bargmann state

$$\langle U' | \exp\left[-\mathcal{H}^{\text{elec}} T/\hbar\right] | U \rangle = \sum_{n=0,\pm1,\pm2,\ldots} \exp\left[-\frac{g^2 \hbar T}{2a_s} n^2 \right] \cos\left[n(\theta' - \theta)\right] \,. \tag{2.102}$$

- Transition amplitude for a single plaquette Bargmann state

$$\langle U'_P | \exp\left[-\mathcal{H}^{\text{elec}} T/\hbar\right] | U_P \rangle = \sum_{n_P=0,\pm1,\pm2,\ldots} \exp\left[-\frac{g^2 \hbar T}{2a_s} 4n_P^2 \right] \cos\left[n_P(\theta'_P - \theta_P)\right] \,. \tag{2.103}$$

- Transition amplitude for multi-link Bargmann state

$$\begin{aligned} &\left\langle U'_{12}, U'_{23}, \ldots \right| \exp\left[-\mathcal{H}^{\text{elec}} T/\hbar\right] \left| U_{12}, U_{23}, \ldots \right\rangle \\ &= \prod_{<\mu\nu>}^{N_{link}} \sum_{n_{\mu\nu}=0,\pm1,\pm2,\ldots} \exp\left[-\frac{g^2 \hbar T}{2a_s} n_{\mu\nu}^2 \right] \cos\left[n_{\mu\nu}(\theta'_{\mu\nu} - \theta_{\mu\nu})\right] \,. \end{aligned} \tag{2.104}$$

- Transition amplitude for Bargmann link states of non-adjacent plaquettes

$$\begin{aligned} &\left\langle U'_{P_1}, U'_{P_2}, \ldots \right| \exp\left[-\mathcal{H}^{\text{elec}} T/\hbar\right] \left| U_{P_1}, U_{P_2}, \ldots \right\rangle \\ &= \prod_{P}^{N_{plaq}} \sum_{n_P=0,\pm1,\pm2,\ldots} \exp\left[-\frac{g^2 \hbar T}{2a_s} 4n_P^2 \right] \cos\left[n_P(\theta'_P - \theta_P)\right] \,. \end{aligned} \tag{2.105}$$

2.6 Construction of the physical transition amplitude under evolution of the full Hamiltonian

In the previous section, we discussed the issue of gauge invariance of transition amplitudes. Now we are prepared to come back to the proper definition and method of computation of amplitudes. The goal is the construction of the MCH (Chapter 4). In order to do so, the first step is to compute the transition amplitudes between "physical" states. By physical states we mean states chosen from a basis which is suitable to describe wave functions of physical particles. The minimal requirement of such a basis is its gauge invariance. For the technical reason, to make practical computations simple we choose the basis of link variables. Thus we consider the transition amplitude between the gauge invariant projection of link states, like

$$\langle U'_{\text{inv}}, T \big| \, U_{\text{inv}}, 0 \rangle \ . \tag{2.106}$$

According to the Eq.(2.69), this gauge invariant amplitude can be expressed in terms of path integral

$$\langle U'_{\text{inv}}, T \big| e^{-\mathcal{H}T/\hbar} | U_{\text{inv}}, 0 \rangle \ = \ \int [dU] \exp\left(-S[U]/\hbar\right) \Big|_{U,t=0}^{U',t=T} \ . \tag{2.107}$$

The standard method to compute such a quantity is the Monte Carlo technique. Using the standard Monte Carlo turns out to be impractical, because the integrand varies over many orders of magnitude. The solution is using the Monte Carlo with importance sampling [112].

2.6.1 Transition amplitude in terms of a ratio of path integrals

The Monte Carlo method with importance sampling is employed in the standard LGT, as the main algorithm to compute the expectation value of an observable expressed by the ratio of two path integrals [2, 5].

In order to express the amplitude as a ratio of two path integrals, a possible trick is splitting

the action into a kinetic (electric) part and a potential (magnetic) part, such that

$$S[U] = \frac{1}{g^2}\frac{a_s}{a_t}\sum_{\square_t}[1 - \text{Re Tr}U_{\square}] + \frac{1}{g^2}\frac{a_t}{a_s}\sum_{\square_s}[1 - \text{Re Tr}U_{\square}] \equiv S^{\text{elec}}[U] + S^{\text{mag}}[U]\,,$$

$$S^{\text{elec}}[U] = \frac{1}{g^2}\frac{a_s}{a_t}\sum_{\square_t}[1 - \text{Re Tr}U_{\square}]\,,$$

$$S^{\text{mag}}[U] = \frac{1}{g^2}\frac{a_t}{a_s}\sum_{\square_s}[1 - \text{Re Tr}U_{\square}]\,. \tag{2.108}$$

Here, $S[U]$ is the Wilson action in U(1) LGT for an anisotropic lattice [23, 24]. Consequently, the transition amplitude can be written as

$$\begin{aligned}\left\langle U'_{\text{inv}}, T\middle|\, U_{\text{inv}}, 0\right\rangle \;=\; & \frac{\int [dU]\,\exp(-S^{\text{mag}}[U]/\hbar)\,\exp(-S^{\text{elec}}[U]/\hbar)\Big|_{U,t=0}^{U',t=T}}{\int [dU]\,\exp(-S^{\text{elec}}[U]/\hbar)\Big|_{U,t=0}^{U',t=T}} \\ & \times \int [dU]\,\exp(-S^{\text{elec}}[U]/\hbar)\Big|_{U,t=0}^{U',t=T}\,.\end{aligned} \tag{2.109}$$

We proved that the path integral is equivalent to the transition amplitude under evolution of Hamiltonian, provided that one considers the transition between gauge invariant projected states. Therefore, we have

$$\begin{aligned}\left\langle U'_{\text{inv}}, T\middle|\, U_{\text{inv}}, 0\right\rangle \;=\; & \frac{\int [\mathrm{d}U]\,\exp(-S^{\text{mag}}[U]/\hbar)\,\exp(-S^{\text{elec}}[U]/\hbar)\Big|_{U,t=0}^{U',t=T}}{\int [dU]\,\exp(-S^{\text{elec}}[U]/\hbar)\Big|_{U,t=0}^{U',t=T}} \\ & \times \left\langle U'_{\text{inv}}, T\middle|\exp\left[-\mathcal{H}^{\text{elec}}T/\hbar\right]|U_{\text{inv}}, 0\right\rangle\,,\end{aligned} \tag{2.110}$$

where for the group U(1), this is given by [23]

$$\mathcal{H} = \frac{g^2}{2a_s}\sum_{<\mu\nu>}\hat{\mathbf{E}}^2_{\mu\nu} + \frac{1}{g^2 a_s}\sum_{\square_s}[1 - \text{Re Tr}U_{\square}]\,,$$

$$\mathcal{H}^{\text{elec}} = \frac{g^2}{2a_s}\sum_{<\mu\nu>}\hat{\mathbf{E}}^2_{\mu\nu}\,, \tag{2.111}$$

$$\mathcal{H}^{\text{mag}} = \frac{1}{g^2 a_s}\sum_{\square_s}[1 - \text{Re Tr}U_{\square}]\,.$$

For using the full action as distribution function in the ratio of path integrals, we rewrite the ratio factor as follows:

$$\frac{\int [\mathrm{d}U]\, \exp(-S^{\mathrm{mag}}[U]/\hbar)\, \exp(-S^{\mathrm{elec}}[U]/\hbar)\Big|_{U,t=0}^{U',t=T}}{\int [dU]\, \exp(-S^{\mathrm{elec}}[U]/\hbar)\Big|_{U,t=0}^{U',t=T}} = \frac{\int [\mathrm{d}U]\, \exp(-S[U]/\hbar)\Big|_{U,t=0}^{U',t=T}}{\int [dU]\, \exp(-S[U]/\hbar)\, \exp(+S^{\mathrm{mag}}[U]/\hbar)\Big|_{U,t=0}^{U',t=T}} \,. \tag{2.112}$$

Combining Eqs.(2.100, 2.110, 2.112) we obtain

$$\left\langle U'_{\mathrm{inv}}, T \middle| U_{\mathrm{inv}}, 0 \right\rangle = \frac{\int [\mathrm{d}U]\, \exp(-S[U]/\hbar)\Big|_{U,t=0}^{U',t=T}}{\int [dU]\, \exp(-S[U]/\hbar)\, \exp(+S^{\mathrm{mag}}[U]/\hbar)\Big|_{U,t=0}^{U',t=T}} \times \sum_{n_1=0,\pm1,\pm2,\ldots} \cdots \sum_{n_N=0,\pm1,\pm2,\ldots} \exp\left[-\frac{g^2\hbar T}{2a_s} \vec{E}^2_{\mathrm{graph}} \right] \times \cos[\vec{n}.\Delta\vec{\alpha}_P] \,. \tag{2.113}$$

In the case of the gauge group U(1), this represents the central expression which yields all physical information about U(1) LGT.

In Chapter 4 we will discuss aspects of the numerical simulation of this ratio, as well as the kinetic (electric) transition amplitude.

Chapter 3

Stochastic Basis

In this chapter, we define the physical stochastic (reduced) basis states, and demonstrate the strategies of construction of such a set of basis states in U(1) LGT. We also introduce the concept of square integrable box states in order to generate normalized stochastic basis states. This kind of basis states will be used to construct finite-size matrices of transition amplitudes, as well as a finite-dimensional effective Hamiltonian (Chapter 4).

3.1 Preliminaries

The standard strategy for the evaluation of path integrals in the Euclidean lattice calculations is the Monte Carlo method with importance sampling. This means that the success of lattice calculations crucially depends on the efficiency of this technique.

In general, one can compute a path integral represented by a sum over some configurations x_i, such that [112]

$$\langle \hat{O} \rangle = \int \hat{O}(x)\mathrm{d}x \approx \frac{1}{N_c} \sum_{i=1}^{N_c} \hat{O}(x_i) \,, \tag{3.1}$$

where $\hat{O}$ is an observable, and N_c is the number of Monte Carlo configurations. Evidently, when N_c is large, Monte Carlo evaluations can be inconvenient. Furthermore, the process of constructing the configurations (basis states) x_i becomes tedious and inefficient. This particularly occurs when one intends to apply this method to systems with many degrees of freedom, e.g. in condensed matter physics, elementary particle physics, lattice field theory and other many-body problems. In such situations, a relevant solution to keep the computational costs at a minimum is to choose a small set of basis states, constructed via stochastic mechanisms,

to reduce the degrees of freedom. Since a finite size basis can catch only some degrees of freedom, one should find the most important basis with the least damaging loss of accuracy, in comparison to a large set of basis states (see Fig.[3.1] as a schematic example.). This small set of basis is identified as a *reduced basis* [113] or the so-called *stochastic basis* [20]. In this case, indeed, we truncate the Hilbert space of theory by decreasing its dimension (which is quite large in the case of deterministic (regular) basis states).

In fact, choosing a finite basis means to decide from what window we want to look at the Hamiltonian. This choice of a suitable basis is crucial for physics. The idea that we suggest here is to construct an effective Hamiltonian, which describes physics in a finite window (e.g. a window of low energy). This is similar to the Kadanoff-Wilson's idea of the renormalization group, which suggests to construct a Hamiltonian, describing physics at the critical point [7, 114].

Figure 3.1: Regular basis (left panel) versus the stochastic basis (right panel) constructed from a distribution function. The regular basis are distributed equidistantly, while the stochastic basis nodes are distributed in a random scheme.

3.2 Principles underlying stochastic basis

We look for a small set of basis states, which should capture the important degrees of freedom of a many-body lattice gauge field Hamiltonian, in some window (a low-energy window or a low-temperature window). That basis should be constructed based on two principles: First the principle of randomness, and second the principle of guidance by the physical action. Therefore, there is a close relation between "stochastic basis" and "equilibrium configurations" (corresponding to thermodynamical equilibrium configurations from a Boltzmann distribution). Such configurations can be generated via the method of Monte Carlo with importance sampling.

The "equilibrium field configurations" in lattice Lagrangian are closely related to the stochastic basis in lattice Hamiltonian. In other words, taking equilibrium configurations at a fixed time slice, yields Bargmann states, which represent physically important degrees of freedom. Hence, via the Monte Carlo with importance sampling (involving a weight factor with the action), we generate a subspace of Hilbert space with a relatively small dimension. It is sufficient to capture most of the physics in some finite temperature window. Therefore, we can construct a reduced set of basis states (Fig.[3.1]), such that the energies of the effective Hamiltonian follows a Boltzmann distribution.

In fact, the equilibrium configurations constructed by the Monte Carlo process belong to a Markov chain, whose elements are correlated with each other [2, 112]. In lattice calculations (generally in the Monte Carlo evaluations of observables), the lattice configurations should be independent of each other, thus we choose a sequence of N_b^{stoc} auto-correlated Markovian configurations $\{C^{(i)}, i = 1, 2, ...N_b^{\text{stoc}}\}$ through the primary Marcov chain, and take it as a set of stochastic basis states.

3.3 Stochastic basis states in U(1) LGT

In general, one can consider the stochastic basis as analogues of configurations drawn from importance sampling (like Metropolis algorithm [115]). Although a configuration is similar to a trajectory in time, and a basis state is a wave function independent of time, however, we can generate a set of basis states, which resemble "representative configurations" using random walks and guidance from the action. For the sake of simplicity, let us consider a single link in U(1) LGT as well as its time evolution. In this case, we have a set of link angles $\{\alpha_1, \alpha_2, ..., \alpha_{N_b^{\text{stoc}}}\}$ as basis states, and the transition amplitude between two link states characterized by

$$M_{ij}(T) = \langle \alpha_i | \exp[-\mathcal{H}T] | \alpha_j \rangle . \tag{3.2}$$

We should mention that in the regular (deterministic) case, the basis states are distributed with the identical distance $\Delta\alpha = \alpha_{i+1} - \alpha_i$, as shown in Fig.[3.1]. To calculate the transition amplitude (see Eq.(3.2)), we have to use normalizable states, which can be constructed by so-called "box states" (Fig.[3.2]). These localized states are denoted by $|\sqcap_i\rangle$, $i = 1, 2, ..., N_b^{\text{stoc}}$, such that:

$$|\sqcap_i\rangle = \int_{\Delta\alpha_i} \frac{d\alpha}{2\pi} |\alpha\rangle \sqcap_i(\alpha) , \tag{3.3}$$

where

$$\sqcap_i(\alpha) = \begin{cases} \text{const.} \neq 0 & , \quad \alpha \in [\alpha_i - \frac{\Delta\alpha_i}{2} , \alpha_i + \frac{\Delta\alpha_i}{2}] \\ 0 & \text{elsewhere} . \end{cases} \tag{3.4}$$

The square integrable box states are normalized to unity, hence

$$\sqcap_i(\alpha) = \left[\frac{2\pi}{\Delta\alpha_i}\right]^{1/2} . \tag{3.5}$$

Using these box states, the transition amplitude is given by,

$$\begin{aligned} M_{ij}(T) &= \langle \sqcap_i | \exp[-\mathcal{H}T] | \sqcap_j \rangle \\ &= \int_{\Delta\alpha_i} \frac{d\alpha_i}{2\pi} \int_{\Delta\alpha_j} \frac{d\alpha_j}{2\pi} \sqcap_i^{\star}(\alpha) \times \Theta(\alpha_i, \alpha_j; T) \times \sqcap_j(\alpha) \\ &\simeq \sqcap_i \ \sqcap_j \frac{\Delta\alpha_i}{2\pi} \frac{\Delta\alpha_j}{2\pi} \Theta(\alpha_i, \alpha_j; T) \\ &= \left[\frac{\Delta\alpha_i}{2\pi}\right]^{1/2} \times \Theta(\alpha_i, \alpha_j; T) \times \left[\frac{\Delta\alpha_j}{2\pi}\right]^{1/2} , \end{aligned} \tag{3.6}$$

where

$$\Theta(\alpha_i, \alpha_j, T) = \sum_{n=0,\pm1,\pm2,\ldots} \exp\left[-\frac{g^2 T}{2a_s} n^2\right] \times cos\,[n\Delta\alpha] . \tag{3.7}$$

Now one can define

$$P_{\alpha_0}(\alpha; T) \propto \Theta(\alpha, \alpha_0; T) , \tag{3.8}$$

in which $P_{\alpha_0}(\alpha, T)$ is a probability density with the following properties:

$$\begin{cases} P_{\alpha_0}(\alpha; T) \geq 0 \quad \text{for all } \alpha , \\ \int_{-\pi}^{+\pi} \frac{d\alpha}{2\pi} P_{\alpha_0}(\alpha; T) = 1 . \end{cases} \tag{3.9}$$

Now let us consider the expectation value of a function $F(\alpha)$, defined by

$$\langle F \rangle = \int_{-\pi}^{+\pi} \frac{d\alpha}{2\pi} F(\alpha)\, P(\alpha) . \tag{3.10}$$

$\langle F \rangle$ can be approximated by

$$\langle F \rangle \approx \sum_{i=1}^{N_b} \frac{\Delta\alpha_i}{2\pi} F(\alpha_i) P(\alpha_i) \tag{3.11}$$

provided that α_i's are sampled from the distribution $P(\alpha)$.

On the other hand, this function can be also estimated by the Monte Carlo method, which reads

$$\langle F \rangle \approx \frac{1}{N_b} \sum_{i=1}^{N_b} F(\alpha_i) . \tag{3.12}$$

Comparing Eq.(3.11) and Eq.(3.12), one concludes that

$$\Delta\alpha_i = \frac{1}{N_b}\,\frac{2\pi}{P(\alpha_i)}\,. \tag{3.13}$$

The function $P(\alpha_i)$ falls off rapidly for large values of α_i, hence $\Delta\alpha_i$ grows when α_i becomes large.

The construction of stochastic basis starts out from considering square integrable box functions. Using Eq.(3.13) we can rewrite the box function $\sqcap_i(\alpha)$ as

$$\sqcap_i(\alpha) = \sqrt{\frac{2\pi}{\Delta\alpha_i}} \equiv \sqrt{N_b^{\text{stoc}}\,P(\alpha_i)}\,. \tag{3.14}$$

As one observes, when α_i is large, $\sqcap_i$ becomes small and vice versa (as stated in Fig.[3.2]).

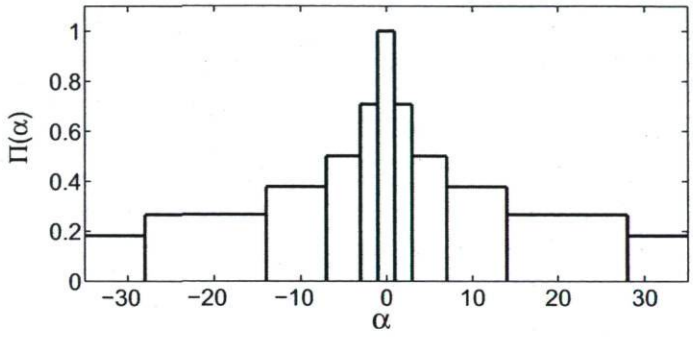

Figure 3.2: Box functions related to the stochastic link angle states.

By box states, the transition amplitude is represented as

$$\begin{aligned} M_{ij}(T) &= \langle \sqcap_i | \exp\left[-\mathcal{H}T\right] | \sqcap_j \rangle \\ &= \int_{\Delta\alpha_i} \frac{d\alpha_i}{2\pi} \int_{\Delta\alpha_j} \frac{d\alpha_j}{2\pi}\, \sqcap_i{}^{\star}(\alpha) \times \Theta(\alpha_i, \alpha_j; T) \times \sqcap_j(\alpha) \\ &\simeq \sqcap_i\ \sqcap_j\, \frac{\Delta\alpha_i}{2\pi}\frac{\Delta\alpha_j}{2\pi}\, \Theta(\alpha_i, \alpha_j; T) \\ &= \left[\frac{\Delta\alpha_i}{2\pi}\right]^{1/2} \times \Theta(\alpha_i, \alpha_j; T) \times \left[\frac{\Delta\alpha_j}{2\pi}\right]^{1/2}\,, \end{aligned} \tag{3.15}$$

Then, the transition matrix elements are given by

$$M_{ij}(T) = \frac{\Theta(\alpha_i, \alpha_j; T)}{N_b^{\text{stoc}}\left[P_{\alpha_0}(\alpha_i; T)\, P_{\alpha_0}(\alpha_j; T)\right]^{1/2}}\,, \tag{3.16}$$

where $P_{\alpha_0}(\alpha, T)$ is the probability density function for one link, given by

$$P_{\alpha_0}(\alpha, T) = \sum_{n=0,\pm1,\pm2,\ldots} \exp\left[-\frac{g^2 T}{2a_s} n^2\right] \cos(n\alpha) \,. \tag{3.17}$$

Table 3.1: Kinetic energy spectrum of one plaquette using regular basis for $g = 1.0$ and $\beta = 0.25$.

n	D_n	E_n^{eff}	E_n^{exact}	abs. error
0	1.00000000	0.0000000	0.0	0.0
1	0.60653083	1.9999989	2.0	1.1×10^{-6}
2	0.60653054	2.0000008	2.0	8.0×10^{-7}
3	0.13533532	7.9999988	8.0	1.2×10^{-7}
4	0.13533524	8.0000012	8.0	1.2×10^{-7}
5	0.01110900	17.9999999	18.0	1.0×10^{-7}
6	0.01110899	18.0000013	18.0	1.3×10^{-6}
7	0.00033546	31.9999995	32.0	5.0×10^{-7}
8	0.00035462	32.0000024	32.0	2.4×10^{-6}
9	3.7267×10^{-6}	49.9999876	50.0	1.2×10^{-5}
10	3.7266×10^{-6}	49.9999961	50.0	3.9×10^{-6}
11	1.5231×10^{-8}	71.9997633	72.0	2.4×10^{-4}
12	1.5231×10^{-8}	71.9997789	72.0	2.2×10^{-4}
13	2.2914×10^{-11}	97.9971144	98.0	2.9×10^{-3}
14	2.2913×10^{-11}	97.9973409	98.0	2.7×10^{-3}
15	1.2908×10^{-14}	127.9235530	128.0	7.6×10^{-2}
16	1.2877×10^{-14}	127.9332884	128.0	6.7×10^{-2}
17	7.3480×10^{-18}	157.8084005	162.0	4.192
18	4.3322×10^{-18}	159.9218144	162.0	2.078
19	2.2565×10^{-18}	162.5307945	200.0	37.47
20	1.8696×10^{-18}	163.2828884	200.0	36.72

The situation is the same for a lattice with an arbitrary size in (2+1)-D, but the mathematical form of distributions $\Theta(U_i, U_j, T)$ and $P(U, T)$ are different. Let us consider again the transition amplitude of a lattice for the compact U(1) gauge group, where the link variables are parameterized by $U(\alpha) = e^{i\alpha}$, $-\pi \leq \alpha \leq \pi$. In fact, this amplitude is a solution of the Schrödinger equation in imaginary time (equivalent to the diffusion equation), hence it takes a probability interpretation. Therefore, by analogy with one link we can express the high dimensional probability density function $\Theta(U_i, U_j, T)$ as

$$\Theta(U_i, U_j, T) \equiv \left\langle U_j \middle| \exp\left[-\mathcal{H}T/\hbar\right] \middle| U_i \right\rangle \,, \tag{3.18}$$

where $U_i(t=0)$ and $U_j(t=T)$ are lattice configurations. The function Θ satisfies the following properties:

$$\begin{cases} 0 \leq \Theta(U_i, U_j; T) \leq 1, & \text{for all } U_j \text{ and } U_i\,, \\ \int_{-\pi}^{+\pi} [dU]\, \Theta(U_i, U_j; T) = 1, & \text{for all } U_i \text{ and } \mathcal{H} = \mathcal{H}^{kin}\,. \end{cases} \tag{3.19}$$

Again we can define the probability density function $P_{U_0}(U,T) \equiv \Theta(U, U_0, T)$ with the same properties in Eq.(3.19). Tabs.[3.3,3.3] show the energy spectrum of the effective Hamiltonian of a plaquette state, calculated via regular basis and stochastic basis (in chapter 4 we will discuss the computation of the energy spectrum). The exact energy is computed by

$$E_n^{\text{exact}} = \frac{g^2\hbar}{2a_s} E^2_{\text{graph}}\,. \tag{3.20}$$

Comparing two situations with the exact results, the relative errors indicate that the idea of using the stochastic basis becomes a reasonable choice for U(1) LGT.

3.4 Stochastic basis via path integrals

For a lattice, the analytical form of the transition amplitude contains a number of summations multiplied by each other (see Eq.(2.100)). Likewise, the normalized distribution function is given by

$$\begin{aligned} P(U\{\alpha_1, \alpha_2, \ldots \alpha_N\}; T) = & \sum_{n_1=0,\pm1,\ldots} \cdots \sum_{n_N=0,\pm1,\ldots} \exp\left[-\frac{g^2\hbar T}{2a_s}\vec{E}^2_{\text{graph}}\right] \\ & \times \cos(n_1\Delta\alpha_1 + n_2\Delta\alpha_2 + \ldots + n_N\Delta\alpha_N)\,, \end{aligned} \tag{3.21}$$

where $\vec{E}^2_{\text{graph}}$ is defined in Eqs.(2.99,2.100). In order to draw samples from this distribution, one has to compute a large series of multiple summations. This is an inefficient way even using a parallel computation procedure, because the summations are highly correlated with each other.

As an alternative method, one can use the path integral in imaginary time as a high-speed technique [116]. In Chapter 2, we saw that Hamiltonian formulation of transition amplitude can be expressed as a path integral (see Eq.(2.107)). Therefore we can represent the probability density function $P(U\{\alpha_1, \alpha_2, \ldots \alpha_N\}; T)$ into a form of a path integral as

$$P(U\{\alpha_1, \alpha_2, \ldots \alpha_N\}; T) = \int [dU] \exp\left(-S[U]/\hbar\right)\Big|_{U^{\text{in}}, t=0}^{U^{\text{fi}}, t=T}\,. \tag{3.22}$$

Table 3.2: Kinetic energy spectrum of one plaquette using the stochastic basis. Same parameters as in Tab.[3.3] .

n	D_n	E_n^{eff}	E_n^{exact}	abs. error
0	1.031120938	-0.122586	0.0	0.122586
1	0.624158460	1.885404	2.0	0.114596
2	0.579030717	2.185599	2.0	0.185599
3	0.141150582	7.831712	8.0	0.168288
4	0.130277856	8.152343	8.0	0.152343
5	0.012367944	17.570589	18.0	0.429411
6	0.011901633	17.724319	18.0	0.275681
7	0.000383709	31.462503	32.0	0.537497
8	0.000356056	31.761693	32.0	0.238307
9	0.000004310	49.417849	50.0	0.582151
10	0.000003912	49.805686	50.0	0.194314
11	1.7499×10^{-8}	71.444358	72.0	0.555642
12	1.5997×10^{-8}	71.803512	72.0	0.196488
13	2.6359×10^{-11}	97.436782	98.0	0.563218
14	2.3551×10^{-11}	97.887341	98.0	0.112659
15	1.5887×10^{-14}	127.093168	128.0	0.906832
16	1.1706×10^{-14}	128.314560	128.0	0.314560
17	2.2392×10^{-15}	134.930608	162.0	27.06939
18	1.7909×10^{-15}	135.824172	162.0	26.17583
19	1.5494×10^{-15}	136.403750	200.0	63.59625

Again one finds that it is a positive function, because there is a positive measure $[\mathrm{d}\mathcal{U}]$ and a positive weight factor $\exp\left[-S^{\text{elec}}/\hbar\right]$ in the right hand side of the above equation. This enables us to find the stochastic basis states from some constructed path integrals between fixed points $(U^{\text{in}}, t = 0)$ and $(U^{\text{fi}}, t = T)$. Fig.[3.3] schematically shows the sampling of points U_i from the distribution $P(U,T)$ via the path integral approach, by intersecting zig-zag paths at $t = \frac{T}{2}$. In such a way one obtains a set of nodes $U_1, ..., U_N$, where each U_i stands for a lattice configuration. This yields a stochastic basis of (non-normalizable) states $|U_1\rangle, ..., |U_N\rangle$. In order to eventually compute normalized wave functions of the Hamiltonian, we need a basis of Hilbert states. We introduce a stochastic basis of square integrable (Hilbert) states via box functions, similar to Eq.(3.14) for one link. But, here we consider all lattice links in the probability density function P, i.e.

$$\sqcap_l(U\{\alpha_l\}) \equiv \sqrt{N_b^{\text{stoc}}\, P(U\{\alpha_l\})}\ ,\quad l = 1, 2, ..., N_{\text{link}}\ . \tag{3.23}$$

Consequently, a matrix element M_{ij} is expressed by

$$M_{ij}(T) = \frac{\Theta(U_i\{\alpha_l\}, U_j\{\alpha_l\}; T)}{N_b^{\text{stoc}} \left[P(U_i\{\alpha_l\}; T)\, P(U_j\{\alpha_l\}; T)\right]^{1/2}} \quad , \quad l = 1, 2, ..., N_{\text{link}} \, . \tag{3.24}$$

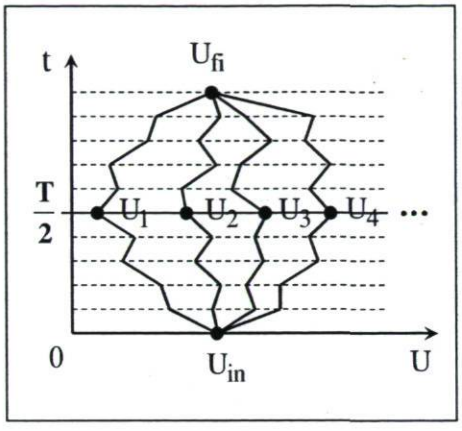

Figure 3.3: Construction of stochastic basis by path integral method. U_1, U_2,... are typical stochastic configurations.

In Chapter 4 we will use this idea to generate the stochastic basis states, for the purpose of extracting the lattice spectra and wave functions in the pure $U(1)_{2+1}$ LGT.

Chapter 4

Energy Spectrum of $U(1)_{2+1}$ LGT

In spite of the facts that LGT has been successful in describing many phenomena in gauge theory (particularly QCD), and potentially powerful enough to predict new events, however, it mostly succeeds in measurements of only ground-state expectation values of observables. As it was mentioned before, one usually computes vacuum-state quantities in the limit of large times, when the excited states collapse to ground state. However, in some situation ground states themselves cannot be easily obtained without considering excited states, when performing measurements through vacuum states (e.g., considering light pion masses and tiny lattice spacings are examples of such situations [106]). In other words, by estimation of excited states one can generally obtain higher precisions in numerical computations.

Because of technical limitations, the conventional Hamiltonian methods mentioned in Chapter 1, falls into serious problems when computing excited state energies and wave functions. On the other hand, there is a lot of interesting physics beyond the ground state. For instance, we can refer to scattering cross sections and decay amplitudes in hadronic systems, hadron wave functions and hadron structure functions, finite density and finite temperature in baryonic matter, etc., where excited states play an important role.

In this chapter, we discuss the MCH method in order to address such difficulties, and we attempt to use it for computing the spectrum of $U(1)_{2+1}$ LGT, in the Hamiltonian framework [116, 117]. Via this technique, we construct an effective low-energy Hamiltonian, based on the Monte Carlo method. By employing this effective Hamiltonian we calculate the transition amplitudes under the evolution of the electric KS Hamiltonian. From matrices of those transition amplitudes, we obtain ground and excited energy levels and wave functions. From such a spectra, we can also compute thermodynamical functions. As examples, the average energy and specific heat will be shown at the end of this chapter.

4.1 The MCH method in U(1) LGT

4.1.1 The effective Hamiltonian

Generally, in the Hamiltonian formulation of many body quantum systems, e.g. lattice systems in field theory, the dimension of Hilbert space is infinite. Therefore, it is a problem to solve the stationary Schrödinger equation

$$\mathcal{H}\,|E_n\rangle = E_n\,|E_n\rangle\ , \tag{4.1}$$

to compute the spectrum and the wavefunctions of the theory. To avoid the difficulty of working with an infinite dimensional Hilbert space, as an alternative solution one can make some approximations amounting to a truncation.

Here we would like to replace the original Hamiltonian by a new one with a finite dimension. It contains the most important degrees of freedom of system, and results in a Hilbert space of a finite dimension. This is similar to the renormalization group approach, by Kadanoff and Wilson [7, 114, 118], who constructed an effective renormalized Hamiltonian with a lower number of degrees of freedom, to compute critical phenomena. Distant from the critical point, such Hamiltonian has no physical meaning. It rises the question: how can we construct such a Hamiltonian in LGT?

In order to compute physical observables in the standard Lagrangian formulation of LGT, one has to evaluate high-dimensional path integrals. In practice, this is possible provided that one considers a small number of configurations of path integrals. Similarly, we propose to generate a limited Hilbert space in the Hamiltonian formulation of LGT. To this end, we employ the Monte Carlo technique with importance sampling. We aim to compute the transition amplitudes which correspond to a finite transiton time T (see Chapter 2). This is similar to the procedure of constructing a lattice KS Hamiltonian, using transfer matrix method (Chapter 1), where the transition time is small ($a_t \to 0$). Here we want to find a matrix of all possible finite temperature (time) transition amplitudes for a limited set of basis states. From this matrix, we construct an effective Hamiltonian which takes a restricted number of degrees of freedom.

Let us express a transition amplitude in imaginary time via the Hamiltonian,

$$\langle U', T|\, U, 0\rangle = \langle U'|\, e^{-\mathcal{H}T/\hbar}\,|U\rangle = \sum_{n=1}^{\infty} \langle U'|\, E_n\rangle\ \exp\left[-E_nT/\hbar\right]\ \langle E_n|\, U\rangle\ . \tag{4.2}$$

Here we use the eigen representation of the Hamiltonian $\mathcal{H}$. Now we want to approximate the Hamiltonian $\mathcal{H}$ by an effective Hamiltonian $\mathcal{H}^{\text{eff}}$, which has fewer degrees of freedom

(e.g. with N eigenstates). Therefore,

$$\langle U'|\, e^{-\mathcal{H}T/\hbar}\,|U\rangle \approx \langle U'|\, e^{-\mathcal{H}^{\text{eff}}T/\hbar}\,|U\rangle = \sum_{k=1}^{N} \langle U'|\, E_k\rangle\, \exp\left[-E_k^{\text{eff}}T/\hbar\right]\, \langle E_k|\, U\rangle\ . \tag{4.3}$$

The idea of the MCH method is that the effective Hamiltonian $\mathcal{H}^{\text{eff}}$ can be found from the action by means of the Monte Carlo technique, such that transition amplitudes become a finite sum over N eigenstates. In this case, N is in the order of magnitude of the number of equilibrium configurations in the Monte Carlo procedure.

We should note that the MCH is not an operator of the canonical form like an ordinary Hamiltonian. Below we show that the $\mathcal{H}^{\text{eff}}$ is defined in terms of some matrix elements in a subspace of the Hilbert space $\mathscr{H}$. This Hamiltonian describes physics in a low-energy window, including a number of low-lying states. In particular, it allows us to compute the thermodynamical observables in a low-temperature window. However, the Hamiltonians $\mathcal{H}$ and $\mathcal{H}^{\text{eff}}$ might describe a different physics in high energy regimes. The concept of MCH has been proven to be successful in numerous applications in quantum mechanics, as well as the Klein-Gordon model as a free scalar field theory [21].

4.1.2 Construction of the effective Hamiltonian

We start from a complete set of orthonormal Hilbert states $|U_1\rangle, ..., |U_N\rangle$, and consider the matrix elements corresponding to the transition amplitude (in imaginary time) between an initial state $\left|U_j, 0\right\rangle$, and final state $|U_i, T\rangle$. For a given N, it is

$$\mathcal{M}_{ij}(T) = \left\langle U_i, T\right|\, U_j, 0\right\rangle \equiv \langle U_i|\exp\left[-\mathcal{H}T/\hbar\right]\left|U_j\right\rangle, \quad i,j \in 1,2,...,N\ . \tag{4.4}$$

Notice that the link states $|U_i\rangle$ and $\left|U_j\right\rangle$ are gauge invariant. Therefore, we can construct a matrix $\mathcal{M} = [\mathcal{M}_{ij}]_{N\times N}$, which is a positive and Hermitian matrix, because the Hamiltonian $\mathcal{H}$ is Hermitian. The diagonalization of $M(T)$ by a unitary transformation yields a unitary matrix U as well as a real diagonal matrix D, such that

$$\mathcal{M}(T) = \mathcal{U}^{\dagger}\, D(T)\, \mathcal{U}\ . \tag{4.5}$$

On the other hand, the projection of $\mathcal{H}$ onto the subspace S_N, generated by the first N states of the basis $|U_i\rangle$, and use of the eigen representation of such Hamiltonian, gives:

$$M_{ij}(T) = \sum_{k=1}^{N} \left\langle U_i\right|\, E_k^{\text{eff}}\right\rangle \exp\left[-E_k^{\text{eff}}T/\hbar\right] \left\langle E_k^{\text{eff}}\right|\, U_j\right\rangle\ . \tag{4.6}$$

We write

$$\mathcal{U}_{ik}^{\dagger} = \left\langle U_i\right|\, E_k^{\text{eff}}\right\rangle, \quad D_k(T) = \exp\left[-E_k^{\text{eff}}T/\hbar\right]\ , \tag{4.7}$$

where $\left|E_k^{\text{eff}}\right\rangle$ are the eigenstates of D, and E_k^{eff} are the eigenvalues of $\ln(D)$. This procedure yields the spectrum of energies,

$$E_k^{\text{eff}} = -\frac{\hbar}{T} \ln D_k(T), \quad k = 1, 2, ..., N . \tag{4.8}$$

The corresponding *k-th* eigenvector can be identified by the *k-th* column of the matrix $\mathcal{U}_{ik}^{\dagger}$. The wave function of the *k-th* eigenstate, expressed in terms of the basis $|U_i\rangle$, is known by the equation (4.7). Therefore, the effective Hamiltonian is constructed as follows:

$$\mathcal{H}^{\text{eff}} = \sum_{k=1}^{N} \left|E_k^{\text{eff}}\right\rangle E^{\text{eff}} \left\langle E_k^{\text{eff}}\right| . \tag{4.9}$$

Once the spectrum and wave functions are available, all physical information can be retrieved. Since the theory described by $\mathcal{H}$, is now approximated by a theory described by a finite matrix $\mathcal{H}^{\text{eff}}$, the physics of $\mathcal{H}$ and $\mathcal{H}^{\text{eff}}$ might be quite different at high energy. Therefore, we expect that using $\mathcal{H}^{\text{eff}}$ we can only reproduce the low energy physics of the system. It means that the MCH takes a window of validity, meaning that there is no physics beyond such a window. In the rest of this chapter, we will show that such a window can be observed in the lattice energy spectrum.

4.2 Matrix of transition amplitudes

We need to compute the matrix $\mathcal{M}(T)$ of transition amplitudes to extract the spectrum of the effective Hamiltonian. In order to compute the elements $\langle U'|\exp[-\mathcal{H}T]|U\rangle$ of this matrix, we express them as

$$\langle U'|\exp[-\mathcal{H}T/\hbar]|U\rangle = \frac{\langle U'|\exp[-\mathcal{H}T/\hbar]|U\rangle}{\langle U'|\exp[-\mathcal{H}^{\text{elec}}T/\hbar]|U\rangle} \times \langle U'|\exp\left[-\mathcal{H}^{\text{elec}}T/\hbar\right]|U\rangle . \tag{4.10}$$

The second factor on the right side is a transition amplitude under the kinetic (electric) part of the Hamiltonian, and we have analytically computed it in Chapter 2. Here we try to compute the first term of Eq.(4.10), which is the ratio of transition amplitudes under evolution of the full Hamiltonian and its kinetic part. To this purpose, we write it as a ratio of path integrals:

$$\mathcal{R} = \frac{\int [dU] \exp(-S[U]/\hbar)\Big|_{U,t=0}^{U',t=T}}{\int [dU] \exp(-S^{\text{elec}}[U]/\hbar)\Big|_{U,t=0}^{U',t=T}} . \tag{4.11}$$

This representation enables us to compute the ratio of amplitudes via the Monte Carlo technique.

Monte Carlo with importance sampling

By convention, one can numerically evaluate the transition amplitude of an observable $\hat{O}$,

$$\langle \hat{O} \rangle = \frac{\int [\mathrm{d}x]\, \hat{O}[x] \exp(-S[x])}{\int [\mathrm{d}x] \exp(-S[x])}\,, \tag{4.12}$$

by Monte Carlo method with importance sampling. Therefore, one writes

$$\langle \hat{O} \rangle = \frac{1}{N_c} \sum_{C} \hat{O}[C]\,, \tag{4.13}$$

where C stands for a path configuration drawn from the distribution $P[x] = \dfrac{\exp(-S[x])}{Z}$. To generate the equilibrium configurations, we use the Metropolis algorithm [115]. Our numerical simulations have been briefly discussed in Appendix B.

Now, by considering the exponential of the full action, $\exp(-S[U]/\hbar)$, as the distribution function for the Monte Carlo calculations, we represent the ratio of transition amplitudes as

$$\mathcal{R} = \frac{\int [dU] \exp(-S[U]/\hbar)\Big|_{U,t=0}^{U',t=T}}{\int [dU] \exp(+S^{\mathrm{mag}}[U]/\hbar) \exp(-S[U]/\hbar)\Big|_{U,t=0}^{U',t=T}}\,, \tag{4.14}$$

where the following relation has been considered for the Wilson action:

$$S[U] = S^{\mathrm{elec}}[U] + S^{\mathrm{mag}}[U]\,. \tag{4.15}$$

Using Eq.(4.12), and considering

$$P(U) = \frac{\exp(-S[U]/\hbar)}{\mathcal{Z}} = \frac{\exp(-S[U]/\hbar)}{\int [dU] \exp(-S[U]/\hbar)\Big|_{U,t=0}^{U',t=T}}\,, \tag{4.16}$$

as a density function normalized to unity, we have

$$\mathcal{R} = \frac{1}{\frac{1}{N_c} \sum_{c=1}^{N_c} \exp(+S^{\mathrm{mag}}[U_c]/\hbar)\Big|_{U}^{U'}} = \frac{1}{\langle \exp(+S^{\mathrm{mag}}[U_c]/\hbar) \rangle_{U,U'}}\,. \tag{4.17}$$

The factor N_c denotes the number of lattice configurations, constructed through the Monte Carlo process. Consequently, we can write a matrix element $\mathcal{M}_{ij}(T)$ (see Eq.(4.4)) as:

$$\mathcal{M}_{ij}(T) = \langle U_i | \exp[-\mathcal{H}T/\hbar] | U_j \rangle = \mathcal{R}_{ij} \times \langle U_i | \exp\left[-\mathcal{H}^{\mathrm{elec}} T/\hbar\right] | U_j \rangle\,, \tag{4.18}$$

and using Eq.(4.17) we have

$$\mathcal{M}_{ij}(T) = \frac{\langle U_i| \exp\left[-\mathcal{H}^{\text{elec}} T/\hbar\right] |U_j\rangle}{\langle \exp(+S^{\text{mag}}[U_c]/\hbar)\rangle_{U_i,U_j}} . \tag{4.19}$$

In fact, the term

$$\left[\langle \exp(+S^{\text{mag}}[U_c]/\hbar)\rangle_{U_i,U_j}\right]^{-1} \tag{4.20}$$

plays the role of a correction factor for the transition amplitude of the electric part of the Hamiltonian. Our calculation of $\mathcal{M}_{ij}(T)$ will be completed by computation of the electric transition amplitude (the second factor in Eq.(4.18)).

Now, combining Eqs.(4.19,3.24) yields:

$$\mathcal{M}_{ij}(T) = \frac{1}{\langle \exp(+S^{\text{mag}}[U_c]/\hbar)\rangle_{U_i,U_j}} \times \frac{G(U_i\{\alpha_l\}, U_j\{\alpha_l\}; T)}{N_b^{\text{stoc}} \left[P(U_i\{\alpha_l\}; T)\, P(U_j\{\alpha_l\}; T)\right]^{1/2}} , \quad l = 1, 2, ..., N_{\text{link}} . \tag{4.21}$$

Notice that N_b^{stoc} is the number of stochastic basis states, while $\mathcal{N}_c$ indicates the number of lattice Monte Carlo configurations (for computing the ratio of path integrals in the full amplitude). In the case of U(1) LGT in two spatial dimensions, we have

$$\begin{aligned} \mathcal{M}_{ij}(T) &= M_{ij}^{\text{mag}}(T) \times M_{ij}^{\text{elec}}(T) \\ &= \frac{\mathcal{N}_c}{\sum_{c=1}^{\mathcal{N}_c} \exp(+S^{\text{mag}}[U_c]/\hbar)\Big|_{U_i}^{U_j}} \times \prod_{m=1}^{N_P} \Big\{ \sum_{n_m=0,\pm1,...} \exp\Big[-\frac{g^2 \hbar T}{2a_s} \vec{E}^2_{\text{graph}} \Big] \times \cos[\vec{n} \cdot \Delta\vec{\alpha}_P] \Big\} . \end{aligned} \tag{4.22}$$

Here

$$\Delta\vec{\alpha}_P = \vec{\alpha}_P^{(i)} - \vec{\alpha}_P^{(j)} \tag{4.23}$$

is the difference between plaquette angles for two lattice states $|U_i\rangle$ and $\left|U_j\right\rangle$. Note that $\vec{\alpha}_P$ is not a real vector, but it represents all N_P plaquette angles on a 2D lattice.

Finally, one constructs the transition matrix

$$\mathcal{M}(T) = [\mathcal{M}_{ij}(T)]_{N\times N}, \quad i, j = 1, 2, ..., N \tag{4.24}$$

corresponding to a finite long time T (i.e. $T \gg a_t$). This matrix enables us to reconstruct the spectrum of the KS Hamiltonian in a finite low energy (temperature) domain.

4.3 Behavior of the matrix of electric transition amplitudes

Here we want to check the validity of the numerical computations of the electric Hamiltonian. We know that $\mathcal{M}(T) \propto \exp(-\frac{\mathcal{H}T}{\hbar})$, therefore, one can simply write

$$\mathcal{M}(2T) \equiv \mathcal{M}(T) \times \mathcal{M}(T) \,. \tag{4.25}$$

This also holds for $\mathcal{M}^{\text{elec}}(T)$, that is

$$\eta = \frac{\mathcal{M}^{\text{elec}}(2T)}{\mathcal{M}^{\text{elec}}(T) \times \mathcal{M}^{\text{elec}}(T)} \equiv 1 \,. \tag{4.26}$$

Fig.[4.1] (left panel) shows a numerical test of this property of the electric transition matrix for a 4×4 lattice.

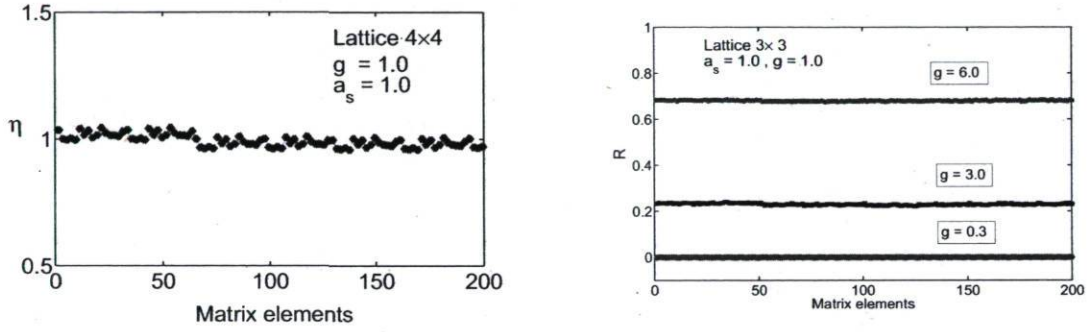

Figure 4.1: Left panel: behavior of the transition matrix elements for the electric Hamiltonian of the 4×4 lattice. The distribution around $\eta = 1$ confirms that $\mathcal{M}^{\text{elec}}(2T) \equiv \mathcal{M}^{\text{elec}}(T) \times \mathcal{M}^{\text{elec}}(T)$. Right panel: behavior of the ratio of transition matrix elements (path integrals) for strong and weak coupling regimes. The lattice size is 4×4 at $\beta = 1.5$. By increasing the coupling constant (e.g., $g = 3.0$ and $g = 6.0$ in the figure), the elements of the ratio matrix tend to 1.0. In the weak coupling regime (e.g., $g = 0.3$), the elements become zero .

4.4 The ratio of path integrals in the strong and weak coupling regimes

Let us express the ratio of path integrals as:

$$\mathcal{R} = \frac{\langle U' | e^{-\mathcal{H}T/\hbar} | U \rangle}{\langle U' | e^{-\mathcal{H}^{\text{elec}}T/\hbar} | U \rangle} \,, \,. \tag{4.27}$$

where

$$\mathcal{H} = \mathcal{H}^{\text{elec}} + \mathcal{H}^{\text{mag}} = \frac{g^2}{2a_s} \sum_{<\mu\nu>} \hat{\mathbf{E}}_{\mu\nu}^2 + \frac{2}{g^2 a_s} \sum_{\square_s} [\text{ReTr}\, U_{\square}] \ . \tag{4.28}$$

The magnetic part of the Hamiltonian becomes small for large coupling constants. Therefore, one expects that the ratio matrix elements tend to unity:

$$\lim_{g\to\infty} \mathcal{H} \equiv \mathcal{H}^{\text{elec}} \ \Rightarrow \ \lim_{\mathcal{H}\to\mathcal{H}^{\text{elec}}} \mathcal{R} = \frac{\langle U'| e^{-\mathcal{H}T/\hbar} |U\rangle}{\langle U'| e^{-\mathcal{H}^{\text{elec}}T/\hbar} |U\rangle} \to 1 \ . \tag{4.29}$$

For small couplings, the situation is different. In this regime, the electric Hamiltonian becomes small, while the magnetic Hamiltonian goes to large values. Hence the ratio of matrix elements goes to zero:

$$\lim_{g\to 0} \mathcal{H} \equiv \infty \ \Rightarrow \ \lim_{\mathcal{H}\to\infty} \mathcal{R} = \frac{\langle U'| e^{-\mathcal{H}T/\hbar} |U\rangle}{\langle U'| e^{-\mathcal{H}^{\text{elec}}T/\hbar} |U\rangle} \to 0 \ . \tag{4.30}$$

Fig.[4.1] (right panel) graphically shows these behaviors for a 3×3 spatial lattice, in a weak coupling regime ($g = 0.3$), as well as two artificial strong coupling regimes ($g = 3.0$ and 6.0).

4.5 Spectrum and wave functions of the lattice Hamiltonian

4.5.1 Spectrum of the electric Hamiltonian

Here we present some results of the MCH simulations. As an example, Fig.[4.2] shows the eigenvalues of the electric part of the KS Hamiltonian for an 8×8 lattice, when the inverse temperature (Euclidian time) is $\beta = 4.2$.

It is clear that the ground state energy is always zero, because there is no gauge nor matter field in the vacuum state of lattice. In the top of this single level, one observes several excited levels. Those states are regulated with respect to the energy of all possible configurations, made by elementary Wilson loops (plaquettes). Fig.[4.3] shows the possible configurations occurring in the first, the second and the third excited levels. The first excited level is the energy of one plaquette of the lattice and the second level is the energy of two neighboring plaquettes with similar orientations. The third level originates (i) from two distinct plaquettes with clockwise or counter-clockwise directions, and (ii) from three adjacent plaquettes and (iii) from square Wilson loops, constructed by four neighboring plaquettes with the same

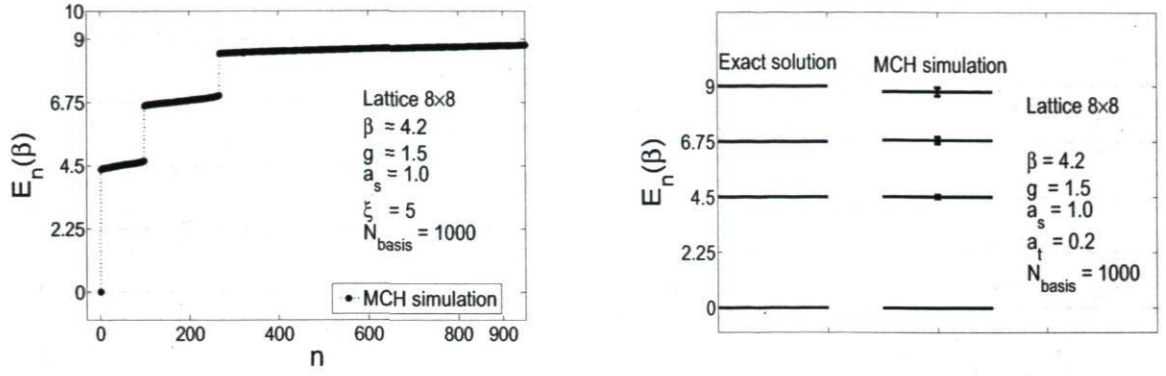

Figure 4.2: Electric Hamiltonian: Two schemes of the energy spectrum of the 8×8 lattice for $\beta = 4.2$. Left panel: Energy spectrum $E_n(\beta)$ in terms of the number of eigenvalues n [116, 117]. The ground level as well as three excited levels are shown. Notice that the horizontal length of each level represents the degree of degeneracy. Right panel: The results shown in the left panel are compared to the results of the exact Hamiltonian (we have made an average between degenerate states in each level of the MCH simulations, along with errorbars) [116].

orientations. The energies are given by

$$E_1^{\text{excit.}} = (g^2\hbar/2a_s)4n^2\Big|_{n=1} = 2g^2\hbar/a_s\,,$$

$$E_2^{\text{excit.}} = (g^2\hbar/2a_s)6n^2\Big|_{n=1} = 3g^2\hbar/a_s\,, \tag{4.31}$$

$$E_3^{\text{excit.}} = (g^2\hbar/2a_s)8n^2\Big|_{n=1} = 4g^2\hbar/a_s\,.$$

For instance, for $g = 1.5$, $\hbar = 1.0$ and $a_s = 1.0$, the first energy level is $E_1^{\text{excit.}} = 4.5$, the second is $E_2^{\text{excit.}} = 6.75$, and the third one is $E_2^{\text{excit.}} = 9.0$ (see Fig.[4.2]).

Recall that in Eq.(4.31) we have considered $n = 1$, but larger values of n also exist, however, they are manifested at higher levels in the spectrum. For example, if we take $n = 2$ for one plaquette, it gives $E = 16g^2\hbar/(2a_s)$, which is the energy of 7^{th} excited level. Likewise, the opposite orientations for side by side plaquettes are not forbidden, but they also give energies corresponding to higher levels. For instance, the energy of two plaquettes with a common link for $g = 1.5$, $\hbar = 1.0$ and $a_s = 1.0$ equals to $E = 11.25$, which is the energy of the forth excited level.

Another point which we should mention here, is the degeneracy of excited energies (as presented in Fig.[4.2]). Actually, this property is related to the number of single and multi-plaquette configurations (see Fig.[4.3]). For example, if a lattice contains only four plaquettes, for the first level we have four single plaquettes with two different orientations for each

one (clock and counter-clockwise). Accordingly, this system involves a number of $4 \times 2 = 8$ levels with the same energy. This means that the rank of degeneracy depends on the size of lattice. Hence, large lattices include very dense spectra. The message is that in the case of large lattices we are faced with a limitation in the number of excited levels. One can bypass such a problem by considering large matrices of transition amplitudes, but on the other hand, this requires very powerful computational resources, as well as long CPU-times.

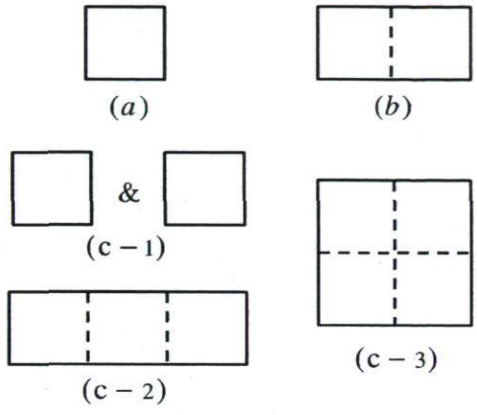

Figure 4.3: The lattice configurations related to the first, the second and the third excited level of the spectrum. The graph (a) is related to the first excited level, the graph (b) generates the second level, and the graphs (c-1),(c-2),(c-3) represent the third excited level.

4.5.2 Scaling window

By collecting energy levels related to various temperatures [116, 117], we can also study the behavior of energy in terms of temperature. This yields a scaling window, which is also called energy or temperature window. Fig.[4.4] presents such a window for the electric Hamiltonian of a spatial lattice sizes 3×3 and 8×8. It is obvious that the energy levels in scaling windows are valid in some special intervals of the Euclidian time β. This is not the case in the thermodynamical limit (Volume $\rightarrow \infty$) as well as the continuum limit (lattice spacings $\rightarrow 0$), where one observes a perfect window. In fact, it is impossible to obtain a smooth energy window, independent of temperature. The reason is that the volume of lattices are finite and the lattice spacings are not zero. Moreover, there is also the influence of statistical errors related to the Monte Carlo calculations, as well as the limited number of stochastic basis states.

As it can be seen from the energy window, the number of excited levels depends on the temperature (or β). For sufficiently large temperatures (when $\beta \rightarrow 0$) the system exhibits

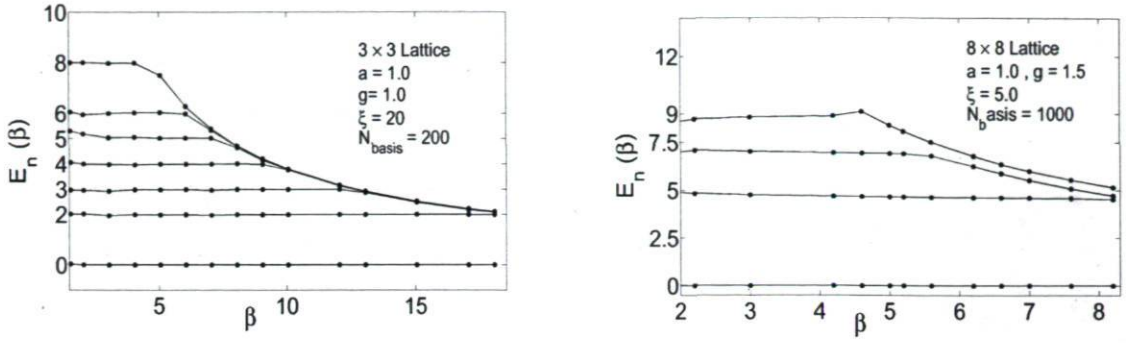

Figure 4.4: Electric Hamiltonian: Scaling window of the energy spectrum for two lattices. Left: 3×3 Lattice, $g = 1.0$, $\xi = 20$, $a_s = 1.0$, $N_{\text{basis}} = 200$. Right: 8×8 Lattice, $g = 1.5$, $\xi = 5$, $a_s = 1.0$, $N_{\text{basis}} = 1000$. Notice that the energy levels are degenerated (not shown), and for both figures the number of excited levels increases when $\beta \to 0$ [116].

more levels of energy, while in the case of $\beta \to \infty$ (small temperatures) the spectrum of the system reduces to the first level, and therefore, one practically observes only the ground state energy. This can be seen from the scaling window of the lattice in question (see Fig.[4.4], for example). In order to explain this in more detail, let us consider only one link state for the sake of simplicity. In this case. the distribution function of link angles

$$P(\alpha, T) = \sum_{n=0,\pm1,\pm2,\ldots} \exp\left[-\frac{g^2 T}{2a_s} n^2\right] \cos[n\alpha] \tag{4.32}$$

takes a Gaussian form (see Fig.[4.5].). It is clear that for larger values of T, the width of

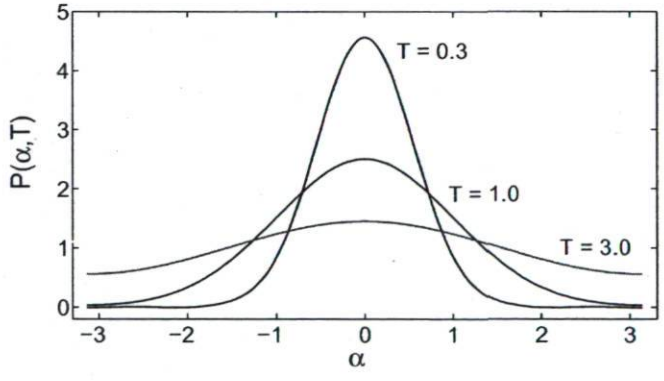

Figure 4.5: Distribution function $P(\alpha, T)$ for one link versus link angle α for T = 0.3, 1.0, 3.0 .

distribution $P(\alpha, T)$ grows, and vice versa. At the same time, one can proceed to the energy space, through a Fourier transformation $P(\alpha) \to \widetilde{P}(E)$ (E is the kinetic energy). One observes that, when $T \to \infty$, the probability density function $P(\alpha, T)$ is a uniform distribution. This means that the corresponding distribution $\widetilde{P}(E)$ becomes a Dirac's delta function $\delta(E)$. Consequently, when $T \to \infty$, the distribution $\widetilde{P}(E)$ projects onto the ground state $E = 0$. This is

similar to the behavior of the Boltzmann distribution, given by

$$\rho(E) = \frac{1}{\mathcal{Z}} \exp\left[-\frac{ET}{\hbar}\right] . \tag{4.33}$$

Therefore, the distribution function $P(\alpha, T)$ is capable of providing the effective Hamiltonian $\mathcal{H}^{\text{eff}}$, to describe the low-energy physics of the system. The above discussion holds for one link on the lattice, but it can be generalized to a lattice system of any size.

As another application, the scaling window also is useful, when computing the lattice thermodynamical functions (discussed at the end of this chapter).

4.5.3 Spectrum of the full Hamiltonian

In order to find the spectrum of the full Hamiltonian, we need to compute the average value of the magnetic part of the Wilson action (the denominator of Eq.(4.19)). For this purpose, we evaluate it by the Monte Carlo method with importance sampling, by analogy with the standard Lagrangian LGT. In this case, while constructing Monte Carlo configurations (path integrals), we should fix initial and final points of paths on U_i and U_j (see again Fig.[3.3] in Chapter 3). The configurations U_i and U_j are, indeed, the same lattice configurations (basis states), stochastically drawn from the kinetic transition amplitudes (Chapter 3).

We employ the even-odd preconditioning (checkerboard) method to construct lattice Monte Carlo configurations. This technique has been demonstrated in some detail in Appendix B. As examples, the results of the total Hamiltonian for the small lattice sizes 3×3 and 4×4 are presented in Figs.[4.11,4.12]. One can observe the vacuum energy level, as well as a few excited states. Also, expansion coefficients of the corresponding wave functions are shown in those figures (right panels). The range of the full energy and vector windows are much smaller than the corresponding electric scaling windows. For example, for the 4×4 lattice we observe just one level, which is ground state energy. Here we explain some possible reasons for such behavior:

(i) One of the principal reasons is the statistical errors, originated from Monte Carlo calculations of the magnetic action $S^{\text{mag}}(U)$. Below, we will discuss how the numerical errors may influence the spectrum of the full Hamiltonian. As an example, we have considered the kinetic scaling window of a single plaquette(see Fig.[4.6]). Applying only one percent of some artificial statistical errors, enormously decreases the number of excited levels and the extent of the original window. To reduce such errors in real computations, we need to increase the number of Monte Carlo configurations $\mathcal{N}_c$ in Eq.(4.22), which practically is limited by computational cost.

(ii) The other important role is played by the electric transition amplitudes. To measure the electric transition amplitudes, one has to perform an exact computation of multiple summations in Eq.(4.22) (which are related to the number of plaquettes in the lattice). In practice, such a term is not exactly computable, particularly for large lattices including many palquettes. The many-fold summations $\prod_{m=1}^{N_P}\Big(\sum_{n_m=0,\pm1,\pm2}[...]\Big)$ in Eq.(4.22) are not independent of each other, thus even parallel calculations would not be helpful for this purpose. Hence, we attempt to evaluate it via some approximations, applicable to relatively large values of β. This also decreases the chance of finding more energy levels, because the excited levels of the spectrum are concentrated in a zone with small values of β.

The technique which we use to compute such N_P-fold sums (with N_P as the number of plaquettes in the lattice), is to truncate them in such a way that those terms with most contributions in summations are maintained. In practice, this procedure is similar to an expansion of lattice in terms of various loop configurations (e.g. the Wilson loops) within a 2D spatial lattice (See Fig.[4.3] again). To illustrate this point further, let us consider a lattice including only four plaquettes (Fig.[2.7]). As discussed in Section 4.5.1, in the expansion of a multiple sum such as

$$\Sigma \equiv \sum_{n_1=0,\pm1,\pm2} \cdots \sum_{n_4=0,\pm1,\pm2} \exp\left[-\frac{g^2\hbar}{2a_s}E^2_{\text{graph}}(n_1,n_2,n_3,n_4)\right]\cos(\vec{n}\cdot\Delta\vec{\alpha})\,, \tag{4.34}$$

in terms of loop configurations (shown in Fig.[4.3]), one obtains that the first term is unity, representing the ground level energy (it is obtained when n_i, $i = 1, ..., 4$ are zero). The second term is related to single plaquettes with two different orientations. It gives the first excited state. The third term, indicating second excited state, is obtained by considering two adjacent plaquettes with the same orientations, and so forth. Therefore, one obtains

$$\begin{aligned}
\Sigma \approx\ & 1 + 2\exp\left[-\frac{4g^2\hbar T}{2a_s}\right]\sum_a \cos(\alpha_a) \\
& + 2\exp\left[-\frac{6g^2\hbar T}{2a_s}\right]\sum_b \cos(\alpha_{b_1}+\alpha_{b_2}) + \\
& + 2\exp\left[-\frac{8g^2\hbar T}{2a_s}\right]\sum_c \cos(\alpha_{c_1}+\alpha_{c_2}+\alpha_{c_3}) + \\
& + 2\exp\left[-\frac{8g^2\hbar T}{2a_s}\right]\sum_c \cos(\alpha_{c_1}+\alpha_{c_2}+\alpha_{c_3}+\alpha_{c_4}) + \\
& + 2\exp\left[-\frac{8g^2\hbar T}{2a_s}\right]\sum_c \cos(\alpha_{c_1}-\alpha_{c_2}) + \dots\,,
\end{aligned} \tag{4.35}$$

where α_a, α_{b_1} and α_{b_2} are plaquette angles defined from Fig.[4.3]. One has to consider all such graphs on the lattice. Use of this truncation process facilitates the computation of the electric transition amplitudes for large lattices, but on the other hand, it works for relatively large values of $\beta \equiv T$, i.e. in the limit where higher terms in Eq.(4.35) are negligible. The message is that it decreases the number of excited levels in the case of electric and full Hamiltonians. Such situation is observed in Fig.[4.12], where only the ground energy level has been retained in the case of full Hamiltonian and the excited levels are not included in the energy window.

(iii) Increasing the number of stochastic basis states can also improve the results for electric and full Hamiltonians, but it increases the dimension of the matrix of transition amplitudes. For such matrices one has to consume enormous CPU times, for the numerical computations (note that each element of that matrix requires individual Monte Carlo computations). On the other hand, this is out of scope of using stochastic basis states, which were considered to reduce the size of those matrices as much as possible.

One may also think about to evaluate such summations as a product of continuous integrals in intervals $[-\infty, +\infty]$ in the regime of weak couplings and low imaginary times (g and T in the exponential term of the electric transition amplitudes). Then for the evaluation of such integrals (namely Gaussian integrals), one should apply again numerical techniques such as Monte Carlo methods. Apart of that, there would be a multiplication of some matrices constructed from link indices, which makes it difficult to construct Gaussian integrands. However, we worked with this trick, but the results were not convincing. The reason was the complicated mathematical form of integrand, also limitations in constructing reliable distribution functions from integrand, as well as statistical ways of sampling of integer numbers (e.g. importance sampling) from such density functions.

4.5.4 Statistical errors in the simulation of the matrix $\mathcal{M}(T)$

In this section let us investigate how the statistical errors destroy the energy spectra of the MCH. It is obvious that in numerical simulations by Monte Carlo, one always encounters the statistical errors. According to this evidence, in our simulations for computing the ratio of path integrals by the method of Monte Carlo, we also observe some numerical errors. In order to visualize these errors in the energy spectrum, let us introduce the errors $\Delta\mathcal{M}_{ij}(T)$ when computing the matrix elements $\mathcal{M}_{ij}(T)$. Therefore, we write [119]

$$\mathcal{M}_{\text{sim}}(T) = \mathcal{M}(T) \pm \Delta\mathcal{M}(T)\,, \tag{4.36}$$

where $\Delta\mathcal{M}(T)$ is an error matrix of the matrix $\mathcal{M}_{\rm sim}(T)$, obtained from numerical Monte Carlo simulations. Previously, we saw that

$$\mathcal{M}(T) \propto \exp\left[-\frac{\mathcal{H}T}{\hbar}\right].$$

Thus, by considering $\mathcal{H}$ as the Hamiltonian of the theory, and also $\mathcal{H}^{\rm err}$ as the perturbation term related to numerical errors, we obtain

$$\mathcal{M}_{\rm sim}(T) \propto \exp\left[-\frac{(\mathcal{H}+\mathcal{H}^{\rm err})T}{\hbar}\right] \approx \exp(-\frac{\mathcal{H}T}{\hbar})\left[1-\frac{T}{\hbar}\mathcal{H}^{\rm err}\right], \tag{4.37}$$

where a Taylor expansion has been applied in the last part. Then from Eq.(4.36) one obtains

$$\Delta\mathcal{M}(T) \propto \exp\left[-\frac{(\mathcal{H}+\mathcal{H}^{\rm err})T}{\hbar}\right] - \exp\left[-\frac{\mathcal{H}T}{\hbar}\right] \approx -\frac{T}{\hbar}\mathcal{H}^{\rm err}\exp(-\frac{\mathcal{H}T}{\hbar}). \tag{4.38}$$

Consequently,

$$\mathcal{H}^{\rm err} \approx -\frac{\hbar}{T}\frac{\Delta\mathcal{M}(T)}{\mathcal{M}(T)}. \tag{4.39}$$

Now, according to the perturbation theory, the first order correction to the n-th eigenvalue of

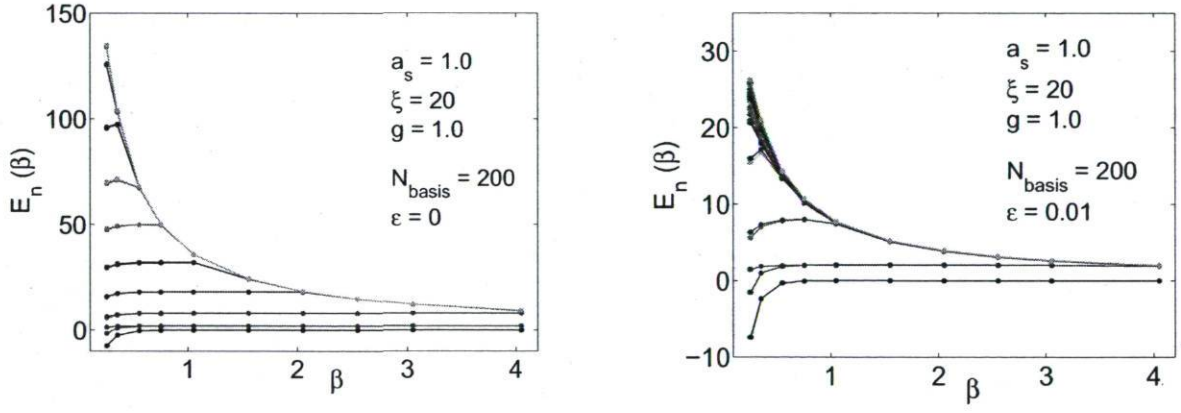

Figure 4.6: Left panel: spectrum of an asymmetric lattice including only one spatial plaquette with $\epsilon = 0$ (no artificial error). Right panel: spectrum with artificial error $\epsilon = 0.01$. For both figures $g = 1.0$, $a_s = 1.0$, $\xi = 20$ and $N_{\rm basis} = 200$ [116].

a wave function is given by [119]

$$\Delta E_n = \langle\Psi'_n|\mathcal{H}^{\rm err}|\Psi_n\rangle = -\frac{\hbar}{T}\frac{\langle\Psi_n|\Delta\mathcal{M}(T)|\Psi_n\rangle}{\exp(-E_nT/\hbar)},$$
$$\Psi'_n = \sum_{n'\neq n}\frac{\langle\Psi'_n|\mathcal{H}^{\rm err}|\Psi_n\rangle}{E_n-E'_n}\Psi'_n. \tag{4.40}$$

It means that from statistical errors of the matrix elements, arising from Monte Carlo simulations, one can estimate the errors in the eigenvalues E_n of the effective Hamiltonian. A similar procedure can be used for the evaluation of numerical errors of eigen functions.

To demonstrate this, we induce some artificial errors by multiplying an error factor ϵ on the electric transition matrix $\mathcal{M}^{\text{elec}}(T)$, such that

$$\Delta\mathcal{M}(T) = \epsilon\, \mathcal{M}^{\text{elec}}(T)\,. \tag{4.41}$$

As an example, Fig.[4.6] compares two situations with an error factor $\epsilon = 0.01$ (right panel) and without artificial errors, $\epsilon = 0.0$ (left panel). One can observe that not only a number of levels are missing, but also the width of the remaining levels has remarkably been decreased, by applying only 1% error (i.e. $\Delta\mathcal{M} = 0.01\mathcal{M}^{\text{elec}}$). The lesson here is that the spectrum of the matrix $\mathcal{M}$ is quite sensitive to the statistical errors in Monte Carlo simulations, particulary here where we perform a logarithmic evaluation in Eq.(4.8). Consequently, one should consider this point in the energy spectrum, especially for the full Hamiltonian discussed above.

4.5.5 Lattice wave functions

The stochastic Hamiltonian $\mathcal{H}^{\text{eff}}$ also enables us to obtain information on the wave functions of the theory. As Eqs.(4.5,4.7) show, the eigenvectors can be determined by means of the unitary transformation of the propagator matrix $\mathcal{M}(T)$. The *k-th* eigenstate $\left|E_k^{\text{eff}}\right\rangle$ can be identified in terms of the *k-th* column of the unitary matrix $\mathcal{U}^\dagger$. Recalling from linear algebra, and given the Hermitian operator $\mathcal{H}^{\text{eff}}$, the wave function $|\Psi_k\rangle$ related to the *k-th* level of the spectrum is characterized by

$$\begin{aligned} |\Psi_k(\beta)\rangle &= \sum_{i=1}^{N_b} C_i^{(k)}(\beta)\,|U_i\rangle \\ &= C_1^{(k)}(\beta)\,|U_1\rangle + C_2^{(k)}(\beta)\,|U_2\rangle + \ldots + C_{N_b}^{(k)}(\beta)\left|U_{N_b}\right\rangle\,, \end{aligned} \tag{4.42}$$

where $C_i^{(k)}(\beta) \equiv \mathcal{U}_{ik}^\dagger$ denotes the *k-th* column of the unitary matrix $\mathcal{U}^\dagger$, N_b is the number of stochastic basis states in our numerical simulations, and $|U_i\rangle$ refers to the Bargmann link states.

Figs.[4.7, 4.8, 4.9] show the orthonormal cofactors (expansion coefficients) $C_i^{(k)}(\beta)$ for the lattice sizes 2×2 as well as 8×8. The kinetic part of the KS Hamiltonian in U(1) LGT in (2 + 1)-dimension has been considered here. One can observe the scaling behavior in these results, where the width of scaling windows of expansion coefficients $C_i^{(k)}(\beta)$ varies for different levels. Moreover, the degenerated into excited energies correspond to different wave functions, which are presented in the respective figures. The same situation also holds for some other lattice sizes, such as 3^2, 4^2, 5^2, 6^2, ... (results not shown here).

In general, it is too complicated to figure out the scaling behavior of the lattice wave functions, because it contains many cofactors and eigenvectors. However, just as an example,

Fig.[4.10] exhibits the coefficients $\{C_i^{(k)}(\beta)\,, k = 1, 2\}$ for the vacuum state, as well as the first excited state of the 6×6 lattice for $\beta = 2.5$.

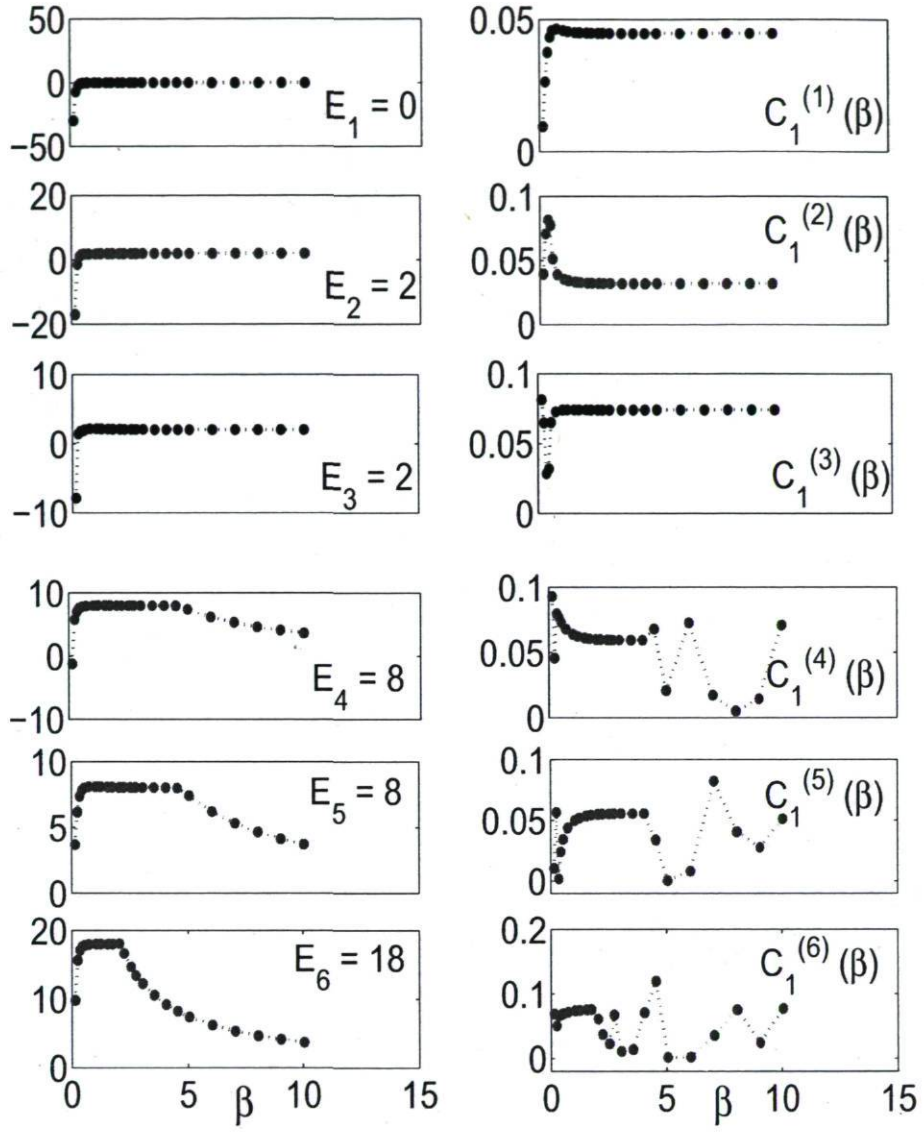

Figure 4.7: Electric Hamiltonian: scaling window for spectrum (left panel) and the expansion coefficients (right panel) of the eigen vectors $\{C_1^{(k)}(\beta) \mid k = 1, ..., 6\}$. Lattice size 2×2, $g = 1.0$, $a_s = 1.0$, $\xi = 20.0$, $N_{\text{basis}} = 500$ [116].

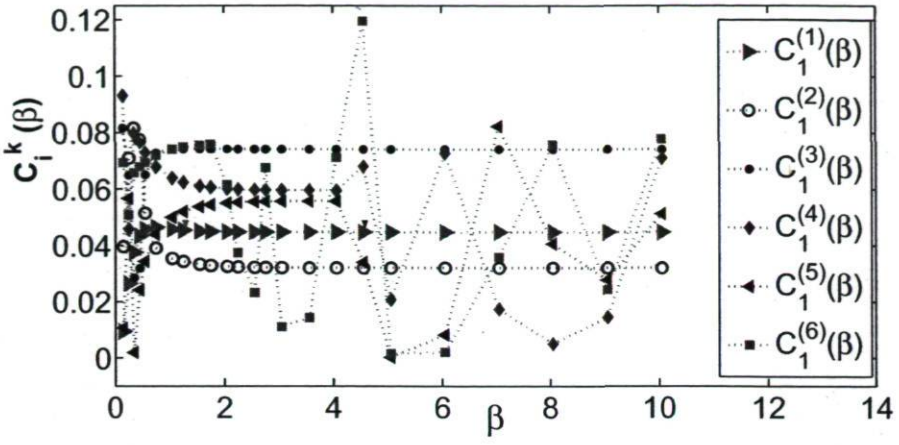

Figure 4.8: Electric Hamiltonian: scaling window for the expansion coefficients of the eigen vectors $\{C_1^{(k)}(\beta) \mid k = 1, ..., 6\}$. Lattice size 2×2, $g = 1.0$, $a_s = 1.0$, $\xi = 20.0$, $N_{\text{basis}} = 500$ [116].

4.6 Lattice thermodynamics from the effective Hamiltonian

The energy spectrum of the effective Hamiltonian enables us to compute thermodynamic observables at the thermodynamical equilibrium. By analogy to the statistical mechanics, one can compute the partition function $\mathcal{Z}^{\text{eff}}(\beta)$, free energy $F^{\text{eff}}(\beta)$, internal energy $U^{\text{eff}}(\beta)$, entropy $S^{\text{eff}}(\beta)$, specific heat $C^{\text{eff}}(\beta)$ and pressure $P^{\text{eff}}(\beta)$ of the lattice system. For example,

$$\begin{aligned}
\mathcal{Z}^{\text{eff}}(\beta) &= \text{Tr}\left[\exp(-\beta\mathcal{H}^{\text{eff}})\right] = \sum_{n=1}^{N} \exp\left[-\beta E_n^{\text{eff}}\right] , \\
U^{\text{eff}}(\beta) &= -\frac{\partial \log \mathcal{Z}^{\text{eff}}(\beta)}{\partial\beta} = \frac{1}{\mathcal{Z}^{\text{eff}}(\beta)} \sum_{n=1}^{N} E_n^{\text{eff}} \exp\left[-\beta E_n^{\text{eff}}\right] , \\
C^{\text{eff}}(\beta) &= -k_B\beta^2 \frac{\partial U^{\text{eff}}(\beta)}{\partial\beta}\bigg|_V \\
&= \frac{k_B\beta^2}{\mathcal{Z}^{\text{eff}}(\beta)} \left\{ \sum_{n=1}^{N} (E_n^{\text{eff}})^2 \exp\left[-\beta E_n^{\text{eff}}\right] - \left(\sum_{n=1}^{N} E_n^{\text{eff}} \exp\left[-\beta E_n^{\text{eff}}\right] \right)^2 \right\} ,
\end{aligned} \tag{4.43}$$

where $\beta = T/\hbar$, k_B is the Boltzmann constant and T denotes the Euclidian time, while τ is the temperature. Fig.[4.13] shows $U^{\text{eff}}(\beta)$ and $C^{\text{eff}}(\beta)$, which are obtained from the spectrum of the effective electric Hamiltonian of the 6×6 lattice [116].

One can also find thermodynamical functions in the Lagrangian formulation of LGT. This requires individual numerical computations for each value of β. For example, see the Ref.[20] for the thermodynamic observables of the free scalar field theory (the Klein-Gordon model). Another point is that the results obtained from the MCH generally exhibit fewer fluctuations

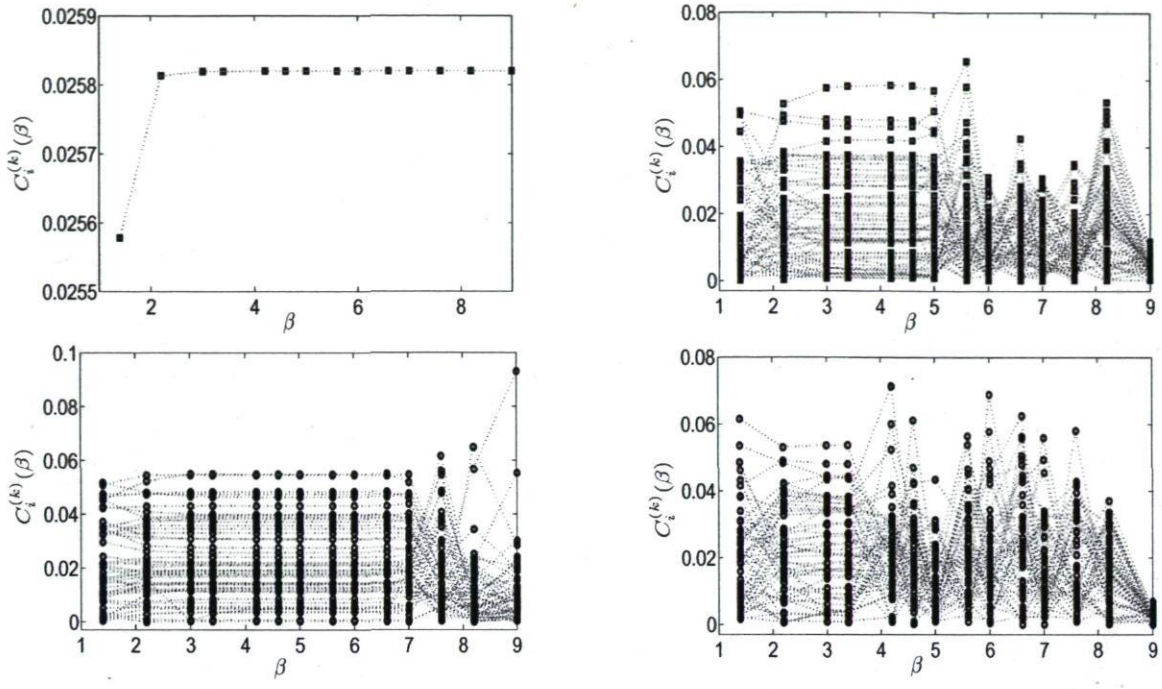

Figure 4.9: Electric Hamiltonian: scaling window for the expansion coefficients of the eigen vectors $\{C_1^{(k)}(\beta) \mid k = 1, ..., 320\}$. Lattice size 8×8, $g = 1.5$, $a_s = 1.0$, $\xi = 5.0$, $N_{\text{basis}} = 1000$. Top left panel: the ground state, bottom left: the first excited level, top right: the second excited level, bottom right: the third excited level. Note that the excited levels are degenerated and only some of their cofactors have been presented here [116].

than the results of the standard Lagrangian approach, in a low temperature regime [20, 19].

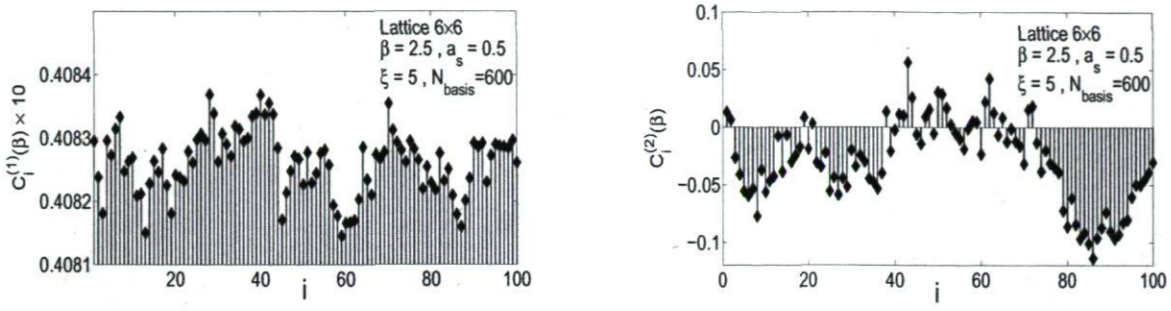

Figure 4.10: Expansion coefficient of wave functions of the electric Hamiltonian. The first two cofactors ($\{C_1^{(k)}(\beta) \mid k = 1, 2\}$) are presented for $\beta = 2.5$, $N_{\text{basis}} = 600$, $\xi = 5.0$, $a_s = 1.0$, lattice size 6×6. Only 100 coefficients are presented, and the first one, $C_i^{(1)}(\beta)$, is multiplied by the factor 10 for the sake of clarity.

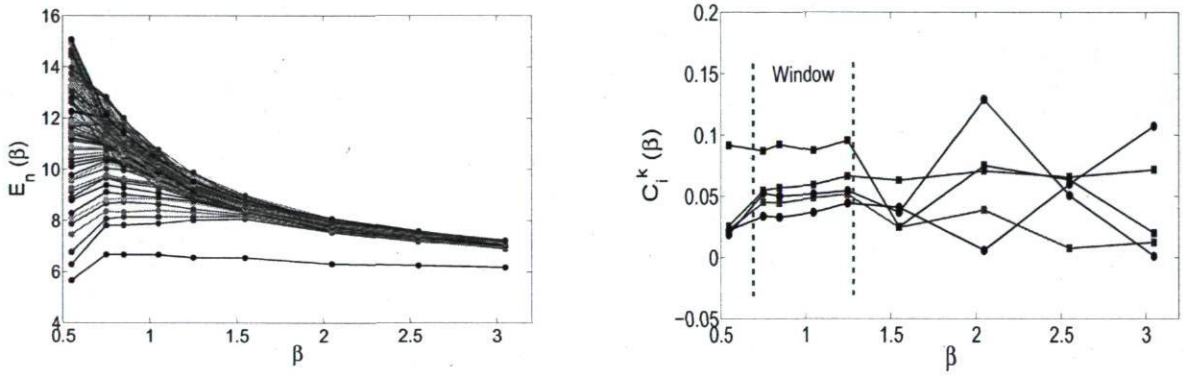

Figure 4.11: Spectrum of the 3×3 lattice ($N_{\text{basis}} = 200$, $\xi = 20.0$, $a_s = 1.0$, $g = 1.0$). Left panel: spectrum of the full Hamiltonian for the 3×3 lattice, Right panel: scaling window of wave functions' cofactors for the 3×3 lattice; $\{C_1^{(k)}(\beta) \mid k = 1, ..., 5\}$ (five levels have been considered) .

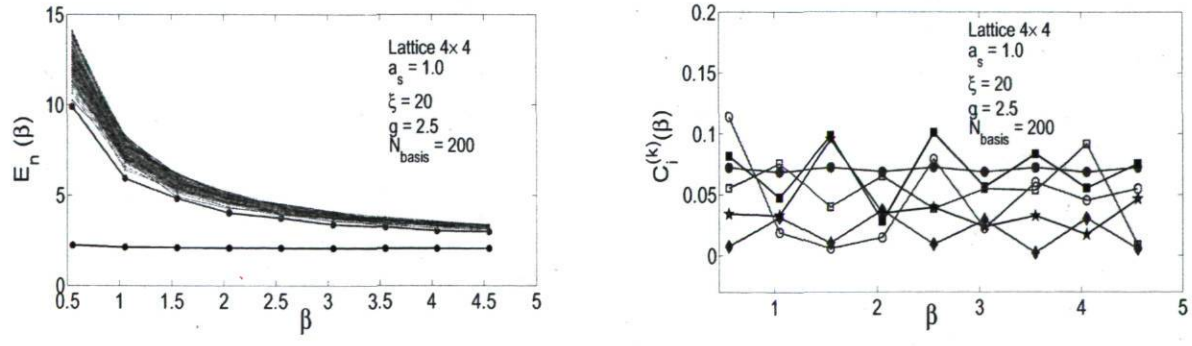

Figure 4.12: Full Hamiltonian: spectrum of the 4×4 lattice. Left panel: energy spectrum. Right panel: scaling window of wave functions' cofactors ($\{C_1^{(k)}(\beta) \mid k = 1, ..., 6\}$). Scaling is observed for one level [116].

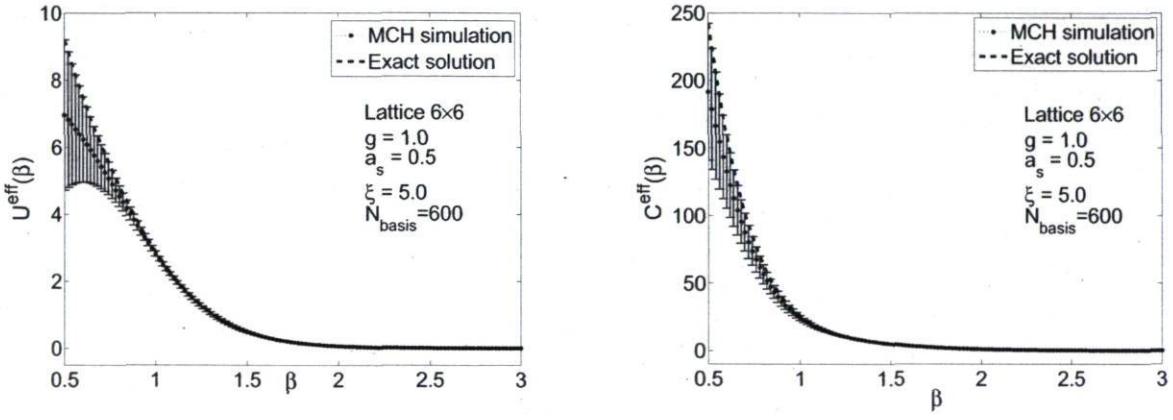

Figure 4.13: Thermodynamical functions. Internal energy $U^{\text{eff}}(\beta)$ and specific heat $C^{\text{eff}}(\beta)$ of the kinetic Hamiltonian. Lattice size 6×6, $N_{\text{basis}} = 600$, $\xi = 5.0$, $a_s = 1.0$, $k_B = 1$ [116].

Part II

Level Spacing Statistics in Classical Chaos

Chapter 5

Random Matrix Theory and Level Spacing Analysis

This chapter deals with some general aspects of random matrix theory (RMT) in quantum chaos, and also some related numerical techniques, such as the level spacing analysis. This is the primary step towards characterizing the global behavior of classical chaotic systems in terms of RMT, which will be discussed in Chapter 6 for two billiard systems.

5.1 Random matrix theory and chaos

In classical dynamics, the behavior of chaotic systems is usually studied in terms of Lyapunov exponents, Poincaré sections and Kolmogorov-Sinai entropy. For instance, the positive Lyapunov exponent $\bar{\lambda}$ determines the sensitivity of "*mixing*" trajectories to initial conditions, in the phase space of a system. It is given by [120]

$$\bar{\lambda} = \lim_{|t|\to 0} \frac{1}{|t|} \ln\left[\frac{\Delta_{ph}(t)}{\Delta_{ph}(0)}\right], \tag{5.1}$$

where $\Delta_{ph}(t) \equiv |\mathbf{q}(t) - \mathbf{p}(t)|$ denotes the distance between the two phase points (note that $\mathbf{q}$ and $\mathbf{p}$ are the canonical coordinates and momenta in a 2N-dimensional phase space). In other words, it is helpful to characterize the mean exponential rate of divergence of two initially close orbits in the phase space. A simple example is a rectangular billiard table with a convex boundary. Billiard balls starting from neighboring points follow diverging paths. Here the absolute value of time, $|t|$, means that the instability is reversible in Hamiltonian systems, and hence does not depend on the direction of time.

The situation in quantum chaos appears to be different. Let us recall that quantum chaos is just the quantum manifestation of chaos in classical mechanics, where one describes a classical chaotic system within the framework of quantum mechanics. In quantum systems, phase space does not exist. Instead, vectors in Hilbert space are used to describe the chaoticity of a system. But, according to the linearity of the Schrödinger equation, the distance between any two vectors in Hilbert space of the system does not change. Hence, any sensitivity to initial conditions is absent in quantum systems.

Another remarkable problem is the difficulty of working with the Schrödinger equation for many body systems, because the exact Hamiltonian is not known. Notice that in real cases, e.g. nuclear experiments, the system has many degrees of freedom and behaves as a many-body problem. Moreover, the dimension of Hilbert space of such systems is infinite. This does not allow one to find an exact solution of the Schrödinger equation, even if the Hamiltonian of the system is known.

However, in spite of these facts, there is a brilliant solution proposed by Wigner and Dyson [62], while studying the spectrum of complex nuclei. It is called random matrix theory (RMT). This theory is based on the statistical properties of the governing Hamiltonian of many body systems, along with its specific symmetries. Wigner et al. [122] evidently found a close similarity between the behavior of nuclear levels on one side, and the eigenvalues of random matrices on the other side. They applied a large ensemble of Hermitian matrices in order to statistically describe the heavy nuclei resonances, in terms of the eigenvalues of those random matrices. This idea enabled them to avoid the Schrödinger equation, as well as working with a self-adjoint Hamilton's operator in an infinite-dimensional Hilbert space. Since then, RMT has been successfully used to study the behavior of complex, disordered and chaotic systems in many-body physics, mathematics, engineering and other subjects.

5.1.1 RMT

In general, the underlying Hamiltonian of a physical system can be represented as a Hermitian matrix, possessing general symmetries such as invariance under time-reversal, rotational invariance, etc.. Therefore, in addition to the Hermiticity (being a critical requirement), the distribution of random matrix elements must also satisfy the same symmetries, for reproducing the statistical properties of Hamiltonian. Depending on the symmetry properties governing the quantum system, RMT proposes three types of invariant Gaussian ensembles of random matrices [62, 122, 130]. But, why the ensembles of Gaussian form? To answer this question, let us take $P(M)$ to be the probability distribution for an ensemble of Hermitian matrices M, and let T be a symmetry transformation on the Hilbert space of the system.

The probability density $P(\mathcal{M})$ is invariant under a symmetric transformation $\mathcal{M}' = T\mathcal{M}T^{-1}$, provided that [62, 131]

$$P(\mathcal{M})\,\mathrm{d}\mathcal{M} = P(\mathcal{M}')\,\mathrm{d}\mathcal{M}'\,, \tag{5.2}$$

where $\mathrm{d}\mathcal{M}$ and $\mathrm{d}\mathcal{M}'$ are some invariant measures. This equality holds only if $P(\mathcal{M})$ is a Gaussian function. For systems with time-reversal symmetry and even spin, the appropriate canonical ensemble to describe the statistical fluctuations of a system, is the Gaussian Orthogonal Ensemble (GOE). If a system is not invariant under time reversal, its statistics are identified by the Gaussian Unitary Ensemble (GUE). Contrary to GOE, where matrices are real and symmetric, here the random Hermitian matrices are complex with different statistical properties than GOE [130]. Another ensemble is called the Gaussian Symplectic Ensemble (GSE), which applies to systems with time-reversal symmetry and half-integer spin. In this case, the Hermitian matrices are quaternionic with two-fold degeneracy in all eigenvalues [62].

From linear algebra one knows that a Hermitian matrix can be expressed in terms of its eigenvalues and eigenstates. Therefore, having the spectrum of a random matrix at hand, instead of using the distribution of matrix elements, one can use the distribution of eigenvalues in order to study the statistics of a quantum system. Accordingly, one can transform the probability density of matrix elements to a probability density of adjacent levels, through a mapping procedure as [62]

$$P(\mathcal{M})\,\mathrm{d}\mathcal{M} \to P(\lambda, \Psi)\,J(\lambda, \Psi)\,\mathrm{d}\lambda\,\mathrm{d}\Psi\,. \tag{5.3}$$

Here λ, Ψ are spectrum and eigenvectors of the Hermitian matrix $\mathcal{M}$, and $J(\lambda, \Psi)$ is the Jacobian of this transformation. In the literature, people usually apply the spacing distribution of eigenvalues of random matrices, which is known as Wigner's surmise [62]. According to the Wigner's suggestion, the probability distribution of the nearest-neighbor spacing (NNS) is given by [121]

$$P_\beta(s) = C\, r_\beta(s) \exp\left[-\int_s^\infty r_\beta(x)dx\right], \tag{5.4}$$

where $r_\beta(s)$ is a conditional probability, which is called the level-repulsion function [122]. If, for example, $r_\beta(x)$ is independent of x, then the result of Eq.(5.4) is a Poisson distribution given by

$$P(s) = \exp[-s]\,, \quad s \geq 0\,. \tag{5.5}$$

A general form of $P_\beta(s)$, in the case of existing n levels in an interval $[s, s + ds]$, is obtained in Ref. [121] as the following form:

$$P_\beta(n, s) = \left[\frac{\Gamma(\frac{\alpha_n}{2} + 1)}{(n+1)}\right]^{\alpha_n+1} \left[\frac{2s^{\alpha_n}}{\Gamma(\frac{\alpha_n+1}{2})^{\alpha_n+2}}\right] \exp\left[-\left(\frac{\Gamma(\frac{\alpha_n}{2} + 1)}{(n+1)\Gamma(\frac{\alpha_n+1}{2})}\right)^2 s^2\right], \tag{5.6}$$

where

$$\alpha_n = n + \frac{(n+1)(n+2)}{2}\,. \tag{5.7}$$

In this relation, β determines the form of the distribution function. For $\beta = 1$, the distribution function takes a GOE behavior, but for $\beta = 2$, and 4 it follows GUE and GSE canonical ensembles, respectively. The zero-th order of $P_\beta(n, s)$ yields the so-called Wigner distribution (or nearest-neighbor level spacing distribution):

$$P_\beta(n=0,s) = \begin{cases} \dfrac{\pi s}{2} \exp\left[-\pi s^2/4\right], & \beta = 1 \quad \text{(GOE)} \\ \dfrac{3^2 s^2}{\pi^2} \exp\left[-4s^2/\pi\right], & \beta = 2 \quad \text{(GUE)} \\ \dfrac{2^{18} s^4}{3^6 \pi^3} \exp\left[-64s^2/\pi\right], & \beta = 4 \quad \text{(GSE)}. \end{cases} \tag{5.8}$$

Note that, most systems in quantum chaos show GOE fluctuations along with a universal behavior, which will be discussed in the following sections.

RMT in quantum chaos

Nowadays, it has been widely accepted that random matrices can also describe the dynamical behavior of fully chaotic quantum systems. An important attempt of using RMT in chaos was through a brilliant work by Bohigas et al. [64]. They hypothesized that the statistical properties of eigenvalues for a time-reversal invariant quantum system can be described by RMT, provided that the classical counterpart of the system is chaotic. They observed different statistical properties between eigenvalues of chaotic systems and those in regular (integrable) systems. They showed that spectra of chaotic quantum systems are equivalent to that restricted by RMT, and correspond to a probability density function of Wigner-type (or Rayleigh distribution), while the spectral properties of integrable systems statistically obey a Poissonian (exponential) distribution:

$$\begin{cases} P_{\text{Wigner}}(s) = \dfrac{\pi s}{2} \exp\left[-\pi s^2/4\right], & s \geq 0 \quad \text{(Chaotic systems)} \\ P_{\text{Poisson}}(s) = \exp\left[-s\right], & s \geq 0 \quad \text{(Integrable systems)}. \end{cases} \tag{5.9}$$

Progress towards a proof has been made by Berry [124, 125], Sieber et al. [126], Müller et al. [127] and Keating et al. [128]. Examples showing such behaviors are chaotic billiard systems, such as the well-known Bunimovich stadium billiard, Lorentz gas (Chapter 6) , etc., as well as regular billiards with square, elliptical and triangle shapes. Here let us recall that chaoticity or regularity of a system depends on symmetries of the Hamiltonian of the system in question. For example, if the number of symmetries is identical to the number of degrees of freedom, then the system is integrable, but if the system has lower symmetries, it becomes chaotic in the classical regime.

From Eq.(5.9) one observes that, the main difference between Wigner and Poisson level spacing distributions occur in the limit of $s = 0$, where $P_{\text{Wigner}}(s = 0) = 0$, but $P_{\text{Poisson}}(s = 0) \neq 0$. The fact behind this behavior of level statistics in physics originates from the so-called level-repulsion, and level-crossing in chaotic and regular cases, respectively. In the case of chaotic quantum systems, $P(s \to 0) = 0$ means that the degeneracies are missing in such a way that the adjacent energy levels repel each other, and the energy manifolds with different quantum numbers do not have any intersection. However, in the integrable case, degeneracies exist and one typically observes a level crossing in energy manifolds. This confirms that small values of s are forbidden so that $P(s \to 0) = 1$ [25]. Precisely speaking, this behavior comes from the nature of the underlying Hamiltonian of a system. For Hamiltonians with many symmetries, when the spacing s goes to zero, the distribution $P(s)$ tends to a maximum. But in the case of a few (or no) symmetries, $P(s \to 0)$ approaches a minimum (for example, see the left panel of Fig.[6.7] in Chapter 6, and compare the Poisson-type and the Wigner-type (GOE) curves for $s = 0$).

Now a key question arises here: is it possible to apply RMT for describing the dynamical behavior of classical chaotic systems? If it is so, then what quantities can play the same role as the Hamiltonian of a quantum system? We leave answering this question to Chapter 6, when discussing the chaotic properties of the classical Lorentz gas and an optical billiard system.

5.2 Level spacing analysis

Now let us consider a quantum system with the spectrum e_i $(i = 1, 2, ...N)$ and the level spacing $s_i = e_{i+1} - e_i$. In general, the spectrum distribution $N(e)$ of a Hermitian matrix fluctuates with its eigenvalues (e.g. see the staircase function $N(e)$ in Fig.[5.1]). One can define a mean level distribution $\overline{N}(e)$. Consequently, the primordial level density $N(e)$ can be splitted into an average part, as well as a fluctuating part:

$$N(e) = \overline{N}(e) + N_{\text{fluc}}(e) \,. \tag{5.10}$$

The average level distribution is given by

$$\overline{N}(e) = \int_0^e de' \, \overline{\rho}(e') \,, \tag{5.11}$$

where $\overline{\rho}(e)$ is the mean level spacing density function.

In fact, $\overline{N}(e)$ is the dominant system dependent part, and $N_{\text{fluc}}(e)$ exhibits the universal part of level spacing distribution. The reason for performing such separation is that the interesting part of the level spacing distribution is the universal fluctuating part, which takes a

small contribution of the distribution. In a fully chaotic system, one expects that this part is independent of the particular system, and exhibits universal fluctuations [63].

The main goal here is to study the sub-dominant fluctuating part of the spectrum by RMT. For this purpose, first one needs a constant mean level spacing s of eigenvalues. The technique that people use in quantum chaos is to renormalize the eigenvalues, in such a way that their average separation density $\overline{\rho}(e)$ becomes unity. After this so-called unfolding procedure, the leading smooth part $\overline{N}(e)$ gets a unit spacing on statistical average. The unfolded levels are characterized by [129]

$$\{\omega_i\} = \{\overline{N}(e_i)\}\,, \quad i = 1, 2, ...N\,, \tag{5.12}$$

where ω_i are dimensionless levels with the separation $s_i = \omega_{i+1} - \omega_i$, and with the density $\overline{\rho}(\omega) = 1$. For the unfolding process we have used a Gaussian broadening method, where the average level density function $\overline{\rho}(e)$ is given by [129]

$$\overline{\rho}_G(e) = \frac{1}{\sigma\sqrt{2\pi}} \sum_k \exp\left[-\frac{(e - e_k)^2}{2\sigma^2}\right]. \tag{5.13}$$

From the unfolded spectrum, we compute the NNS distribution $P(s)$ (see Eqs.(5.8, 5.9)). It

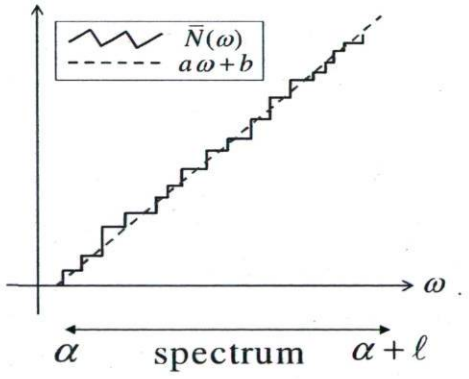

Figure 5.1: Schema of level density $N(\omega)$ and corresponding average density $\overline{N}(\omega)$.

denotes the histogram of finding a separation s between neighboring levels. This can indicate whether a system is chaotic or regular.

The level spacing distribution $P(s)$ contains no information about the correlation between consecutive eigenvalues. The quantity which measures the seperability between two adjacent spacings is the two-point correlation coefficient C, which is defined by [62, 63]

$$C = \sum_i (s_i - 1)(s_{i+1} - 1) \Big/ \sum_i (s_i - 1)^2\,, \tag{5.14}$$

where $s_i = \omega_{i+1} - \omega_i$ stands for the spacing of the regularized levels ω_i. For an integrable system (Poissonian spectrum) C is zero, and for a chaotic one (GOE-type spectrum) $C = -0.27$ [63].

When the rescaled sequence of levels is available (i.e. $\{\omega_i \mid i = 1, 2, ..., N\}$), then one can also evaluate the least square deviation of the spectral step function $N(\omega)$, from the best straight line $(a\omega + b)$ fitting it in an interval $[\alpha, \alpha + \ell]$ of the length ℓ. It is called the Dyson-Mehta rigidity, given by [63, 122]

$$\Delta_3(\ell; \alpha) = \frac{1}{\ell} \, Min_{a,b} \int_{\alpha}^{\alpha+\ell} [N(\omega) - a\omega - b]^2 \, d\omega \, . \tag{5.15}$$

By replacing the functional form of $N(\omega)$ in Eq.(5.15), one obtains a formula as [123]

$$\begin{aligned} \Delta_3(\ell; \alpha) = \frac{n^2}{16} - \frac{1}{\ell^2}\left[\sum_{i=1}^{n} \tilde{\omega}_i\right]^2 + \frac{3n}{2\ell^2}\left[\sum_{i=1}^{n} \tilde{\omega}_i^2\right] \\ -\frac{3}{\ell^4}\left[\sum_{i=1}^{n} \tilde{\omega}_i^2\right]^2 + \frac{1}{\ell}\left[\sum_{i=1}^{n} (n - 2i + 1)\tilde{\omega}_i\right] , \end{aligned} \tag{5.16}$$

with $\tilde{\omega}_i = \omega_i - (\alpha + \frac{\ell}{2})$, which means one takes the center of the interval as origin. Note that other measures of the spectral rigidity, i.e. Δ_1 and Δ_2, have been also introduced by Dyson and Mehta [62], but Δ_3 has proven to be more useful in RMT.

In Chapter 6, we will use the above information in order to study the chaotic behavior of the two-dimensional triangular Lorentz gas, as well as a classical optical billiard. In particular, we will apply the above-mentioned parameters (i.e., $P(S)$, C and Δ_3) to study the level spacing fluctuations of those systems.

Chapter 6

Level Spacing Statistics of the 2D Lorentz Gas

In this chapter, we develop the method of level spacing analysis for the 2D Lorentz gas, in the finite and the infinite-horizon regimes. We will also apply it to a pseudo-potential system, which is an optical billiard. The goal is to show that universal behavior also exists in such systems of classical chaos. We show that the fluctuation statistics of an action matrix of the Lorentz gas displays a universal property, in agreement with RMT. Such a matrix is constructed by some bouncing trajectories in the billiard zone. This is a signature of a strongly chaotic classical system. Moreover, the distribution of length matrix elements approaches a Gaussian (in the limit of infinitely many collisions), which points to the existence of an underlying central limit theorem.

6.1 The 2D Lorentz gas

The Lorentz gas is a model equivalent to a Sinai billiard system, where the billiard ball moves in an open system of equal-size rigid disks, located on a 2D regular grid. In particular, one considers a triangular lattice, such as Figs.[6.1,6.2]. Such regular lattice of disks is invariant under a discrete group of spatial translations, characterized by the positions of the disk's centers [147]. Therefore, the system can be identified with a unit cell with periodic boundary conditions. Billiards with other geometries can be generally characterized by geometry of the cells (e.g. triangle, square, hexagon, etc.). In this system of rigid circular disks, a large number of point-particles (billiard balls) alternate between free motion and collisions with the scatterers (Fig.[6.1]), exposing irregular and random walk behavior. In general, the geometry

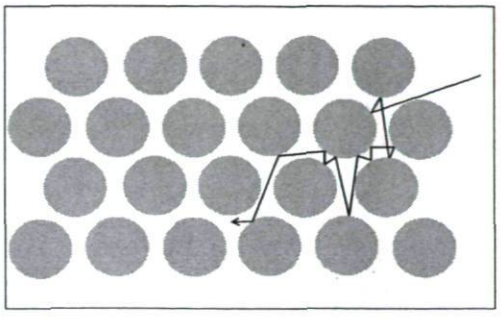

Figure 6.1: The 2D Lorentz gas along with a trajectory of the point-particle.

of the 2D Lorentz gas can be divided into the following types:

(a) The finite-horizon: Free paths between collisions are bounded in a trapping domain and cannot travel long distances, because the scatterers block every direction of motion. Thus the horizon of the point particle is finite, also the diffusion coefficient of the system is positive and finite [28].

(b) The infinite-horizon: The point-particle may move indefinitely with no reflection from disks, because there are wide corridors, which enable them to escape to infinity without collision to hard scatterers. This is possible if the point-particle moves in one of the six directions $\theta = 0, \pi/3, 2\pi/3, \pi, 4\pi/3, 5\pi/3$. In this regime the diffusion coefficient in the lattice is infinite [28]. Note that the Sinai billiard belongs to this class [27, 28].

(c) The localized: The density of the system is higher than in the case of the finite regime. The diameter of obstacles is larger than the distance between centers of disks. In this case, the motion of the point-particle is captured in closed areas composed of three adjacent disks, and the diffusion coefficient of the system is zero (because the point-particle is not able to move beyond its trapping zone).

In summary, the (inverse) density of a system for different regimes is characterized by [120]

$$\begin{cases} \sigma > \sigma_{critic} & \text{infinite-horizon regime} \\ 2 < \sigma \leq \sigma_{critic} & \text{finite-horizon regime} \\ \sigma = 2 & \text{localized regime}, \end{cases} \tag{6.1}$$

where $\sigma = L/R$, with R being the radius of disks and L being the distance between the centers of two adjacent disks, and $\sigma_{critic} = \dfrac{4}{\sqrt{3}} = 2.3094$.

6.1.1 The Lorentz gas and the central limit theorem

First, as a reminder, let us recall the central limit theorem. Let $\{\xi_1, \xi_2, ..., \xi_N\}$ be a sequence of independent and identically distributed random variables with the finite mean $\langle\xi\rangle$. Moreover, this sequence has the sum $S_N = \xi_1 + \xi_2 + ... + \xi_N$, as well as the finite variance σ_N^2. For the simplicity one can also define a useful variable as

$$Z_N = \frac{S_N - N\langle\xi\rangle}{\sigma_N \sqrt{N}} . \tag{6.2}$$

It has been proven that the distribution function of Z_N tends to a standard normal distribution in the limit when $N \to \infty$; That is,

$$P(Z_N \leq z) \to \int_{-\infty}^{z} \frac{1}{\sqrt{2\pi}} \exp\left[-\frac{z^2}{2}\right] dz . \tag{6.3}$$

This behavior is commonly known as the central limit theorem (CLT) [132, 133, 136], which plays a crucial role in describing stochastic phenomena in physics and other areas of science. For instance, it does converge to the Brownian motion, and in particular, it is an evidence of a finite diffusion coefficient (the variance σ_N is proportional to the diffusion constant) [137].

In the case of billiard systems, such as the Lorentz gas with the finite-horizon, the point particle makes a random walk between rigid disks (see Fig.[6.1]). In fact, such a system is classically deterministic system, and each segment of trajectory between two subsequent bounces depends on, and is completely determined by the preceeding segment of trajectory. However, if one computes the correlator between the segment n and the segment $n + k$, such correlation tends to zero, when k becomes large. Thus, two segments of the same trajectory, which are sufficiently distant in terms of travel time or number of intermediate bounces, will statistically become independent. Therefore, such trajectory segments (Λ_n) are a series of random numbers. Because the sum of discrete stochastic numbers still is a random number, hence the whole trajectory length ($\Lambda = \sum \Lambda_n$) would be a random number. Therefore, it can be rigorously shown that the distribution of a sufficiently large ensemble of trajectory lengths becomes a Gaussian distribution, in the limit of many collisions. In other words,

$$P_G(\Lambda) = \frac{1}{\sqrt{2\pi\sigma_n^2}} \exp\left[-\frac{(\Lambda - \langle\Lambda\rangle)^2}{2\sigma_n^2}\right] , \tag{6.4}$$

where $\Lambda = \{\Lambda_1, \Lambda_2, ..., \Lambda_n\}$ behaves as a set of random independent variables, and σ_n^2 is the variance of the distribution. According to the above statement, such a distribution obeys the CLT[1]. This is, indeed, an evidence of chaoticity for the classical Lorentz gas, which has been widely studied theoretically and experimentally [120].

[1] In our simulations, this would be convinced when the initial points of trajectories are randomly distributed on the billiard boundary (see the following sections).

It should be mentioned that for the Lorentz gas, the CLT was proven only for the finite-horizon model [138, 139]. In the case of the infinite-horizon, the CLT has not been proven yet. Furthermore, in this case the standard diffusion coefficient is infinite and there is no convergence to the normal Brownian motion [140].

Let us also remark that Bálint and Gouëzel [141] have shown that the CLT holds for the Bunimovich stadium billiard, as well. They proved that the limit distribution ($N \to \infty$) is a Gaussian, but the scaling factor is not given by the standard expression $\sqrt{N}$, but rather by $\sqrt{N \log N}$. This is consistent with the numerical results of this billiard by Laprise et al. [71], which has been done by studying the statistical behavior of lengths of trajectories.

6.2 Level spacing statistics of the action matrix

Now let us come back to the question posed in Chapter 5: is it possible to apply RMT for describing the dynamical behavior of classical chaotic systems?

In fact, due to the universality of level spacing statistics in quantum chaos, the statistical properties of the energy levels of a quantum system are not related to the details of the dynamical properties of the system. Instead they depend only on the symmetries of the Hamiltonian. Such property did, actually, originate from the Wignerian type of level spacing distribution. This is the so-called Bohigas-conjecture, which was postulated by Bohigas et al. [64], based on computational evidence from the quantum Sinai billiard. But in the case of classical systems, Hamiltonian yields a continuous energy spectrum, and therefore, is unsuitable to play a role such as a Hamiltonian matrix in a quantum system. Thus, one asks what parameter can be used in the case of classical chaos, to play an analogous role as the Hamilton matrix in quantum chaos?

The answer is hidden in the term "symmetry" and the quantity, which contains the same symmetries as the Hamiltonian in the classical regime, is the action. Because the level spacing in quantum chaos is universal, therefore it is reasonable to expect that we will be able to define a level spacing from a finite dimensional matrix, whose elements are given by the action. Such level spacing should have the same properties as the energy level spacing in quantum chaos. Hence, we may consider the action of a system and do the same analysis in a quantum model, in order to study the chaotic dynamics of a classical system. This means that instead of a matrix representation of the Hamiltonian, one may construct a Hermitian matrix of the action, and apply RMT spectral analysis to the spectrum of such a matrix.

According to this, we propose a so-called action matrix whose elements are the values of

the action, evaluated by the Euler-Lagrange equation. In fact, the solutions of this equation are some trajectories, specified by some initial and final boundary points which, we assume, are taken from a finite set of nodes. Thus, with each pair of boundary points, say Q_{in} and Q_{fi}, we associate a trajectory Q^{traj} taking the length Λ and the action S, given by

$$\begin{aligned} \Lambda[Q^{\text{traj}}] &= \int_{Q_{\text{in}}}^{Q_{\text{fi}}} ds\Big|_{Q=Q^{\text{traj}}} , \\ S[Q^{\text{traj}}] &= \int_{Q_{\text{in}}}^{Q_{\text{fi}}} dt\, \mathscr{L}(Q(t), \dot{Q}(t), t)\Big|_{Q=Q^{\text{traj}}} . \end{aligned} \tag{6.5}$$

Considering a finite set of discrete points $\{Q_1, Q_2, ..., Q_N\}$, we find a classical trajectory Q_{ij}^{traj}, connecting each pair of Q_i and Q_j (See the left panel of Fig.[6.4] as an example). These trajectories are generated by a point-particle, which moves between Q_i and Q_j in a zig-zag pattern. For each trajectory we can evaluate its length and action [2]

$$S_{ij} = S[Q_{ij}^{\text{traj}}] \quad , \quad \Lambda_{ij} = \Lambda[Q_{ij}^{\text{traj}}] . \tag{6.6}$$

Notice that the velocity of the point-particle is considered to be unity, thus we eliminate it from the above quantities. S_{ij} and Λ_{ij} constitute the elements of the action and the length matrices $S = [S_{ij}]_{N\times N}$ and $\Lambda = [\Lambda_{ij}]_{N\times N}$, which are real and symmetric. Therefore, the matrices S and Λ have discrete spectra with real eigenvalues. This is in a close analogy with the energy spectrum of the Hamiltonian, which is the tool for level spacing statistics in a chaotic quantum system.

6.3 Level spacing fluctuations of the Lorentz gas

Now let us consider a 2D Lorentz gas of a single point particle, moving in an array of identical hard disks. Fig.[6.2] shows an elementary triangular cell of such a lattice, as well as the trapping region Ω for the single particle. The dynamical behavior of the system depends on

[2] In fact, the reason for using trajectories originates from the Alekseev-Brudno theorem [142]. This theory indicates that in the algorithmic theory of dynamical systems, the information $I(\tau)$ concerning a segment of a trajectory with temporal length τ, is defined by [143]

$$\lim_{|\tau|\to 0} \frac{I(\tau)}{|\tau|} = KSE ,$$

where KSE denotes the Kolmogorov-Sinai entropy, which is positive when the Lyapunov exponent $\bar{\lambda}$ is also positive. This means that prediction of a new segment of a chaotic trajectory requires some extra information proportional to the length of the segment, and does not depend on the previous length of the trajectory. In such situation, the information $I(\tau)$ takes a random behavior and cannot be drawn from the observation of the history of the motion. However, in the case of sufficiently short time intervals, one can predict the behavior of a system, even a chaotic one.

the density of the gas, given by σ^{-1}. We are interested in studying the chaotic behavior of the system in both the finite-horizon and the infinite-horizon regimes.

To this end, we choose a sequence of initial and final nodes $\{x_1, x_2, ..., x_N\}$, regularly distributed on the border $\Gamma \equiv \partial\Omega$ of the moving region (see Fig.[6.3]). We ignore any random positioning of the boundary points to ensure that the chaotic behavior of the system has a dynamical origin. In addition, due to the symmetry of the system, we take the boundary nodes on the one-sixth of the border and on the convex part. The classical trajectory of the

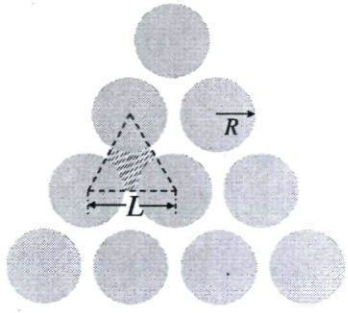

Figure 6.2: Schematic representation of the Lorentz gas in a triangular symmetry.

point-particle between two boundary nodes x_i and x_j is constructed through the elastic collisions on the edge of the trapping domain (see Fig.[6.4], left panel). The trajectory segments between successive collisions to the hard disk scatterers are straight lines. The exact number of rebounds in our numerical calculations, however, is the number of collisions only on rigid disks, thus we do not count the collisions on the straight lines connecting the centers of disks. By constructing all possible trajectories between boundary points, corresponding to a specific number of collisions, we construct a time-reversal symmetric matrix Λ, whose elements are the geometrical lengths $\{\Lambda_{ij} \mid i, j = 1, 2, ..., N\}$. From this matrix we perform the level spacing analysis on the length spectrum. Note that, when the point-particle moves with a constant velocity, and therefore a constant kinetic energy, then the Lagrangian is proportional to the length of the trajectory. This means that the action matrix is equivalent to the length matrix through the equation[3]

$$[S_{ij}]_{N\times N} = \sqrt{mE/2}\,[\Lambda_{ij}]_{N\times N}\,. \tag{6.7}$$

According to this, we can compute the spectrum of the length matrix Λ in behalf of the action matrix S. As discussed in Section 6.1.1, the distribution $P(\Lambda)$ of length matrix elements for a sufficiently large number of rebounds tends to a Gaussian probability distribution, provided

[3]Notice that from $S = \int \mathscr{L}(q(t), \dot{q}(t), t)\, dt$, we have

$$S = \sum_{n=1}^{N} \frac{1}{2} m\, v_n^2\, t_n = \sum_{n=1}^{N} \frac{1}{2} m v_n\, \lambda_n = \sqrt{mE/2} \sum_{n=1}^{N} \lambda_n = \sqrt{mE/2}\,\Lambda\,,$$

where the velocity of the particle is constant ($E = 1/2\, mv_n^2 = 1/2\, mv^2$).

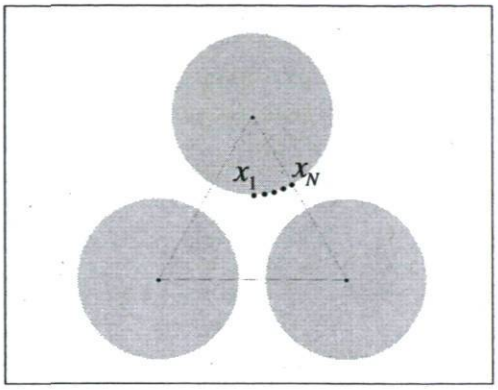

Figure 6.3: Regular distribution of nodes $x_1, ...x_N$ on the boundary of the trapping area.

that the system is chaotic. Such behavior of the point particle has been also proven by the CLT [138, 141]. In this limit, the length matrix Λ itself becomes a GOE matrix [46] (after a suitable normalization). To check this and see how the matrix elements behave, we computed the motion of the moving-particle in the trapping area, for a sufficiently large number of rebounds, namely $N_{reb} = 3000$ [144]. The distribution of trajectory segments for a finite-horizon regime with the density $\sigma = 2.25$ is presented in Fig.[6.4] (right panel). The Gaussian form of this distribution says that the CLT holds for this system in the limit of $n \to \infty$. This is sufficient to guarantee that the level fluctuations $P(s)$ and spectral rigidity $\Delta_3(\ell)$, obtained from the matrix Λ, also show GOE behavior [62].

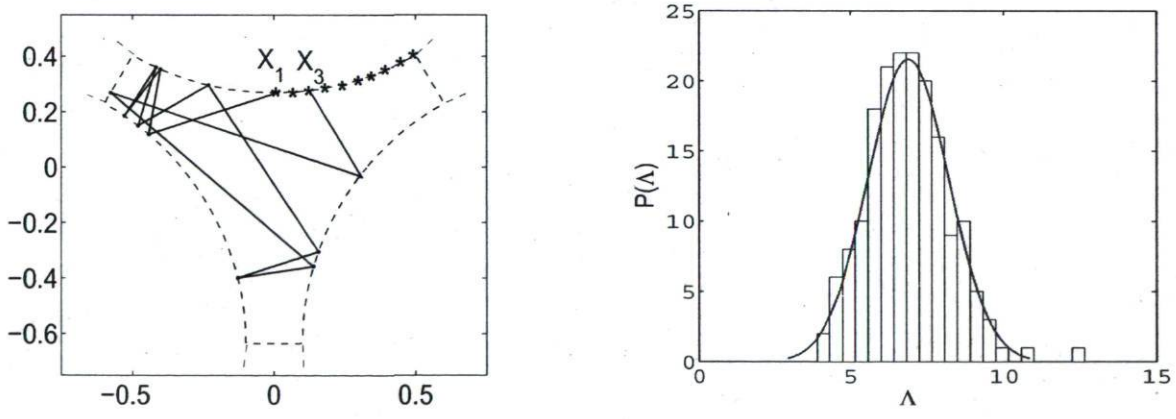

Figure 6.4: Left panel: A sample trajectory of the point-particle between two boundary nodes in the trapping zone. The number of rebounds from disks is $N_{\text{reb}} = 10$. Right panel: Distribution $P(\Lambda)$ of the length matrix elements for the finite-horizon model with $\sigma = 2.25$ and $N_{\text{reb}} = 3000$ [144].

6.4 Estimation of numerical errors

To estimate the numerical errors, we construct a trajectory ζ from a given initial point x_0 to an arbitrary point x'' on the boundary of the capturing region (Fig.[6.2]). We do this for a specific number of rebounds, N_{reb}. Thereafter, we perform a time-reversal procedure, such that the point particle starts its motion from x'', and following the same number of rebounds, it arrives at some x_0'. Then, a measure of errors is given by $\Delta x \simeq |x_0' - x_0|$. Fig.[6.5] explains the behavior of relative error versus the number of rebounds, for the finite-horizon regime of the Lorentz gas. One can observe that relative errors follow an exponential law

$$\langle \text{err} \rangle \sim \exp\left[\alpha_1 N_{\text{reb}} + \alpha_2\right] , \tag{6.8}$$

for the number of rebounds $N_{\text{reb}} \leq 40$, where $\alpha_1 = 0.397$ and $\alpha_2 = -16$. The linear part of this graph denotes a maximum error (100%) for $N_{\text{reb}} \geq 40$. We consider $N_{\text{reb}} \sim 20$, that allows us to retain at least 8 digits of precision for the measurement of the level spacing analysis.

The exponential behavior of errors is related to the positive Lyapounov exponent of the system, which determines the chaoticity of the system. Comparing this scheme of errors for the Lorentz gas with that for a circular stadium billiard (as a regular system) shown in Fig.[6.6], one finds this exponential behavior of errors as another fingerprint of chaos. Moreover, the estimation of numerical errors ensures that the chaoticity of the system originates from the dynamics of the system, and not from the numerical noise.

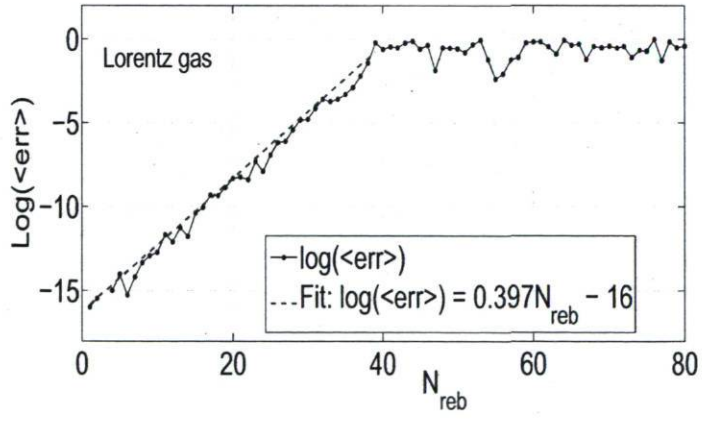

Figure 6.5: Lorentz gas: relative errors as a function of number of rebounds for the finite-horizon case ($\sigma = L/R = 2.25$) [144].

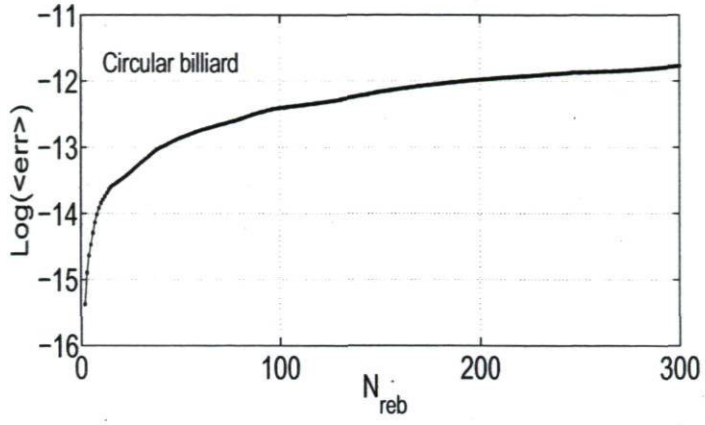

Figure 6.6: Logarithm of relative error as a function of number of rebounds for a circular stadium billiard. The $\log(\langle \text{err} \rangle)$ is not a linear function of N_{reb}, i.e., the behavior of errors $\langle \text{err} \rangle$ is not exponential for this integrable system [144].

6.5 The finite versus the infinite-horizon regime

In the case of the finite-horizon regime we choose $\sigma = 2.25$, and we consider a sequence of $N = 40$ boundary nodes, as well as $N_{\text{reb}} = 15$ collisions with the hard disks of the system. Fig.[6.7] (left panel) displays the NNS fluctuations $P(s)$, constructed from the unfolded spectrum of the length matrix Λ. As one observes, the distribution $P(s)$ takes a Wignerian form which is consistent with the prediction of RMT for fully chaotic systems, that is GOE behavior [64].

Another statistical quantity which we have computed, is the spectral rigidity $\Delta_3(\ell)$ of the length matrix Λ (shown in Fig.[6.7], right panel). The result confirms again the GOE behavior of the system [144].

The value $C = -0.27$ of the correlation coefficient[4] between nearest neighbor level spacings, is another characteristic of the GOE statistics in chaos [63, 146]. For the Lorentz gas, we obtained this value, used as the input for the unfolding procedure. In the infinite-horizon regime, the density of the gas, $\sigma > 4/\sqrt{3}$, allows the point-particle to travel long distances without collision to hard disk repellers. We consider a transition from the finite-horizon with the density $\sigma = 2.25$ to the infinite-horizon regime with $\sigma = 2.5$. The results of $P(s)$ and $\Delta_3(\ell)$ for $\sigma - 2.5$ are presented in Fig.[6.8]. One can observe that the NNS fluctuations of the system basically do not change, meaning that the universality of chaotic properties holds during this transition. Such a behavior of the Lorentz gas has been demonstrated through

[4]From a physical point of view, the negative correlation between spacings indicates the rigidity of the GOE spectrum. That is, when a small spacing is observed, the adjacent spacing tends to be higher [145].

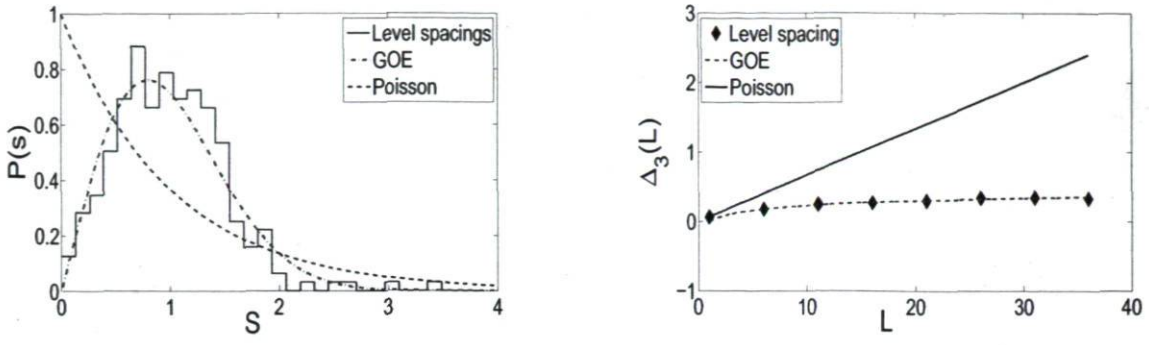

Figure 6.7: Lorentz gas: level spacing distribution $P(s)$ for the finite-horizon model (σ = 2.25) (left panel). Number of boundary points N = 40 and number of rebounds N_{reb} = 15. The Wignerian shape of $P(s)$ is a characteristic of chaos in the system. Right: spectral rigidity $\Delta_3(\ell)$ for the finite-horizon model [144].

the computation of the average Lyapunov exponent for a triangular symmetry [147]. Furthermore, the length $P(\Lambda)$ is shown in Fig.[6.9], indicating some deviations from a Gaussian. These deviations come from the long free paths of the moving-particle, which are due to the existence of wide channels between hard disks in the open regime. Although there is no any theoretical proof of the CLT for this model of the Lorentz gas, nevertheless, the approximate similarity between $P(\Lambda)$ and the Gaussian function may be a hint to the validity of limit theorem for the Lorentz gas with the infinite-horizon. However, this subject requires more extensive theoretical and numerical investigations.

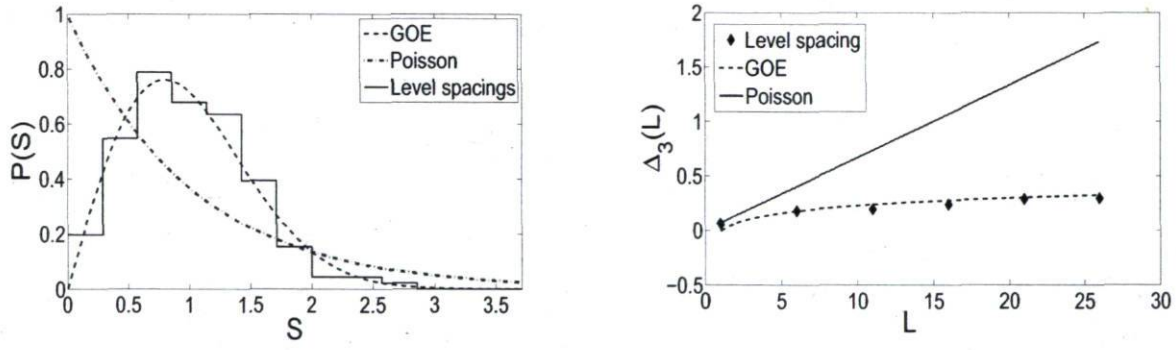

Figure 6.8: Lorentz gas: the infinite-horizon regime for σ = 2.5. Left panel: Level spacing distribution $P(s)$ of the length spectrum. Right panel: Dyson-Mehta rigidity $\Delta_3(\ell)$ of the length matrix. Number of rebounds N_{reb} = 15 and number of boundary nodes N = 40 [144].

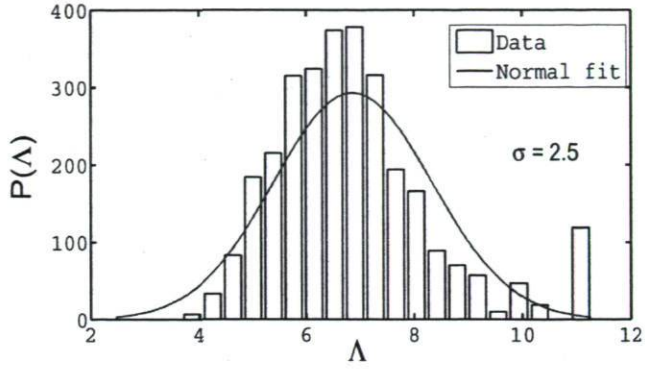

Figure 6.9: Lorentz gas: the infinite-horizon regime for $\sigma = 2.5$. Distribution of length matrix elements $P(\Lambda)$. number of boundary nodes $N = 40$ for $N_{\text{reb}} = 3000$ [144].

6.6 Statistical fluctuations of potential systems

In this part, we would like to address the question if a universal behavior in classical chaos will also persist in the presence of a potential in chaotic systems. As a first step in this direction, here we consider a classical model of an optical billiard, consisting of some zones with different optical properties (refraction indices). At the interface of such zones, Descartes-Snell's law enforces a change of direction and velocity of the beam of light. Thus this optical system is similar (but not equivalent) to a potential system where, however, the change of velocity and direction follows Newton's laws. Technically, we construct spectra from a matrix of time-of-travel, corresponding to a set of trajectories. As a result we find that this chaotic optical billiard shows also universal behavior [148].

6.6.1 Optical stadium billiard

Let us consider a 2D optical stadium billiard [148]. The shape of its outer boundary is the same as the Bunimovich stadium [29], which is a fully chaotic classical billiard model. Its interior region consists of several concentric areas, arranged like tracks in a track and field stadium (see Fig.[6.10], left). The outer stadium boundary is a reflecting wall and behaves like a potential barrier. Each track corresponds to a zone of some refraction index η. The refraction index increases by increments from the center to the outer boundary of the stadium. The left panel of Fig.[6.11] shows a typical trajectory between two boundary points. The refraction index is given by a step function, with an envelope given by $\eta(r) = \eta_c + (r/r_{max})^2$. Here η_c denotes the refraction index of the central area, and r_{max} stands for the distance of the outer boundary to the center of the stadium. Fig.[6.10] (right panel) shows the distribution of η across a section of the billiard, including $N_\Gamma = 5$ zones with $\eta_c = 2$ and $r_{max} = 10$ for the

azimuthal angle $\phi = 0$.

It should be noted from the experimental point of view that, a real optical billiard obeys the laws of quantum mechanics (wave optics). This means that light is emitted from a point source as a spherical wave. Heisenberg's uncertainty principle holds with respect to position and momentum. Wave optics is the valid description in the regime $\lambda \sim R$, where λ is the wave length and R is the spatial extension of the system. On the other hand, ray optics (geometrical optics) is valid in the regime $\lambda \ll R$. Ray optics also describes the propagation via the wave vector of wave fronts. Such light ray satisfies the Fermat's principle, during the transition between two different refraction zones. Here we assume that we are in the regime of geometrical optics, and we treat the propagation of light in terms of ray optics. Thus our model can be viewed as a classical billiard model, where, however, optical laws determine the transition between different optical zones. Then a beam of light propagates along an optical path, where the length and time-of-travel are given by

$$\begin{aligned} \Lambda &= \int d\ell = \sum_i \ell_i \,, \\ T &= \int d\ell \frac{1}{v} = \int d\ell \frac{\eta}{c} = \frac{1}{c} \sum_i \ell_i \eta_i \,. \end{aligned} \tag{6.9}$$

Here, c and $\eta_{vac} = 1$ denotes the speed of light and refraction index in the vacuum, respectively. In addition, η_i and ℓ_i stand for refraction index and geometric path length, respectively, in zone i (note that a trajectory may visit a given zone several times). According to Fermat's principle, light rays propagate along optical paths of minimal travel time. An important consequence of this principle is Snell-Descartes' law

$$\frac{sin\theta_1}{sin\theta_2} = \frac{\eta_2}{\eta_1} = \frac{v_1}{v_2} \,, \tag{6.10}$$

which means that the direction and the velocity of the light ray change at the boundary between different optical media. Therefore, this kind of billiard resembles a potential system, where the magnitude and the direction of velocity also change as a function of the local potential. To construct the matrix of time-of-travel, likewise we did for the Lorentz gas, here we also take a set of equidistantly located boundary points $x_i, i = 1, \ldots, N_{\text{bound}}$, located on a quarter of the outer billiard boundary (see Fig.[6.10] left). The classical trajectory of the light ray between the boundary points x_i and x_j is constructed by taking into account Snell-Descartes' law at the boundary between zones of different refraction indices and the law of reflection at the outer boundary. We classify trajectories by the number of rebounds N_{reb}. For a given pair of boundary points x_i, x_j and number of rebounds N_{reb}, we construct the trajectory by choosing an initial angle α with respect to the normal of the boundary at the starting point. This will yield an arrival point, say x_f. Then we make a search in the initial angle α, until $|x_f - x_j| < \delta$ where δ is an acceptable error tolerance. This gives an acceptable trajectory. In fact, for a given pair of boundary points x_i, x_j and given number of rebounds N_{reb}, there are

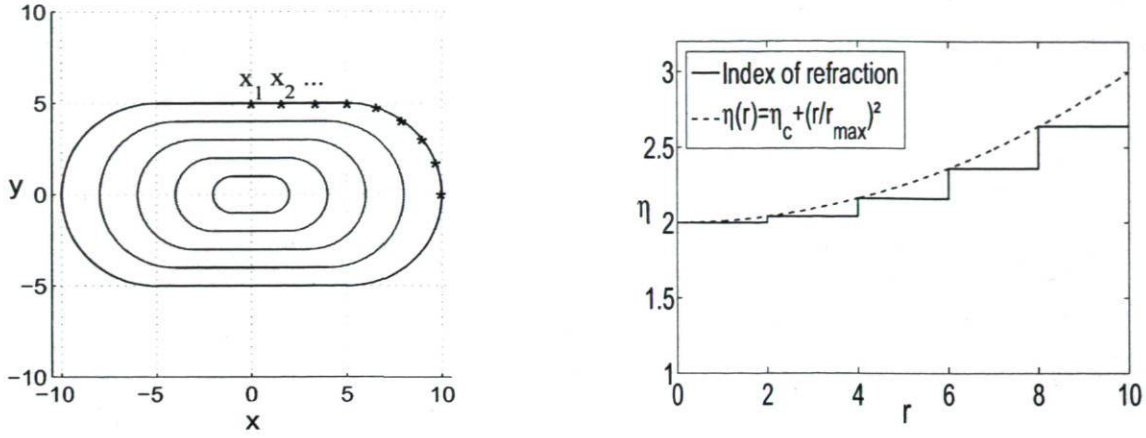

Figure 6.10: Optical billiard: 2D optical stadium billiard composing $N_\Gamma = 5$ zones of different refraction indices η (left panel). Right panel: the refraction index (solid line) as a function of radius for azimuthal angle $\phi = 0$ [148].

many trajectories, and its number increases nonlinearly when N_{reb} is increased. We find those trajectories by making a sweep in the initial angle α (by increments of $\Delta\alpha = \pi/4 \times 10^{-4}$), and we have constructed a set of $N_{traj} = 30$ trajectories for each pair of boundary points. For each pair x_i, x_j and a corresponding trajectory Λ_{ij}, we compute the time-of-travel according to Eq.(6.9), yielding a matrix element $\mathcal{T}_{ij}$] of the time-of-travel matrix $\mathcal{T}$. Due to the time-reversal symmetry, the matrix $\mathcal{T}$ is symmetric, and all matrix elements are positive.

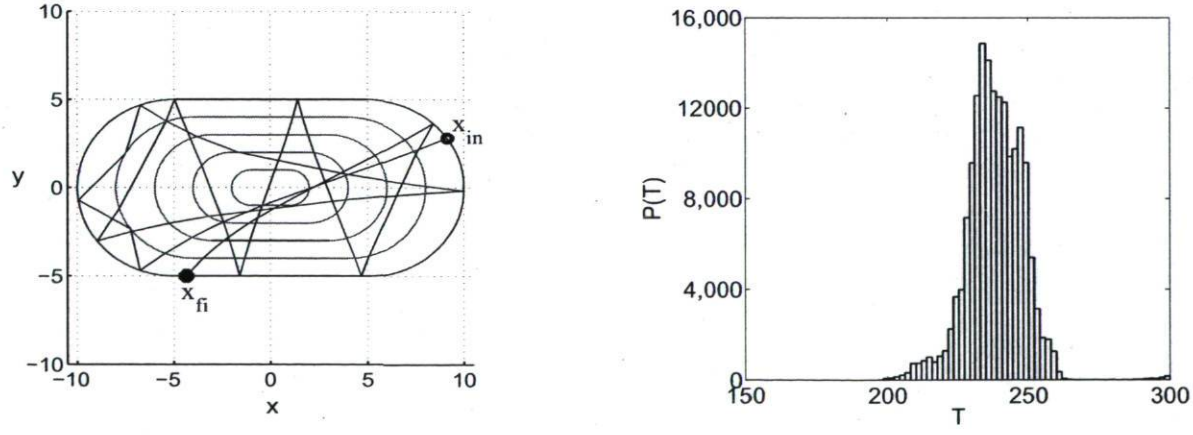

Figure 6.11: Optical billiard: 2D optical stadium billiard with typical trajectory between points x_{in} and x_{fi} located on the outer boundary (left panel). Distribution of matrix elements $P(\mathcal{T}_{ij})$ from time-of-travel matrix $\mathcal{T}$. The number of rebounds is $N_{\text{reb}} = 8$ (right panel) [148].

6.6.2 Level spacing analysis and numerical results

Here by analogy to the calculations for the Lorentz gas, we compute the spectrum of the matrix $\mathcal{T}$, carry out the spectral unfolding, and construct the level spacing distribution $P(s)$ as well as the spectral rigidity Δ_3 [148]. We choose $N_{\text{reb}} = 8$ with a relative error around 10^{-10} for our numerical simulations.

In the classical Bunimovich stadium billiard, chaotic behavior becomes more apparent, when increasing the number of rebounds at the outer boundary. Qualitatively, the same behavior is expected to occur in the optical billiard considered here. We consider $N_{\text{bound}} = 65$ boundary points located on a quarter of the stadium boundary (see Fig.[6.10] left). Fig.[6.11] (right) shows the distribution $P(\mathcal{T}_{ij})$ of matrix elements of $\mathcal{T}$. The shape of the curve is a deformed Gaussian. If the time-of-travel between two subsequent collisions would be a random number, and if two subsequent time-of-travel data were statistically independent [71, 141], then the CLT would predict a Gaussian shape for $P(\mathcal{T}_{ij})$. Such condition, of course, does not hold here. The deviation of $P(\mathcal{T}_{ij})$ in shape from a Gaussian can be interpreted as a qualitative measure of how much (in temporal length) the sections of trajectories differ in behavior from a random walk.

From the unfolded spectrum of the time-of-travel matrix $\mathcal{T}$ (with $N_{\text{bound}} = 65$), we compute the spectral level spacing distribution $P(s)$ and the spectral rigidity Δ_3 (see Fig.[6.12]). One observes that $P(s)$ follows a Wignerian distribution, and the spectral rigidity Δ_3 shows a GOE-type behavior, both consistent with RMT. We obtain a correlation coefficient $C = -0.27$ which is another signature for the Wignerian type of the level spacing distribution. These results suggest that this optical stadium billiard model is fully chaotic and its level spacing fluctuations follow universal behavior. It should be noted that these distributions represent a statistical average from data of $N_{\text{traj}} = 30$ independent sets of time-of-travel matrices $\mathcal{T}$. Such number of levels gives sufficiently reliable statistics (it should be recalled that Bohigas et al.[64] considered nuclear spectra from about 30 different nuclei in their conjecture of universality).

6.7 Synopsis

In this chapter we showed that the chaotic behavior of the 2D Lorentz gas can be described by RMT, which is also the case for a chaotic optical billiard. By tracing the random-walk motion of a point-particle, separately in both systems, we computed matrices of the lengths of trajectories of the particle. By statistical analysis of the spectra of those matrices, we found

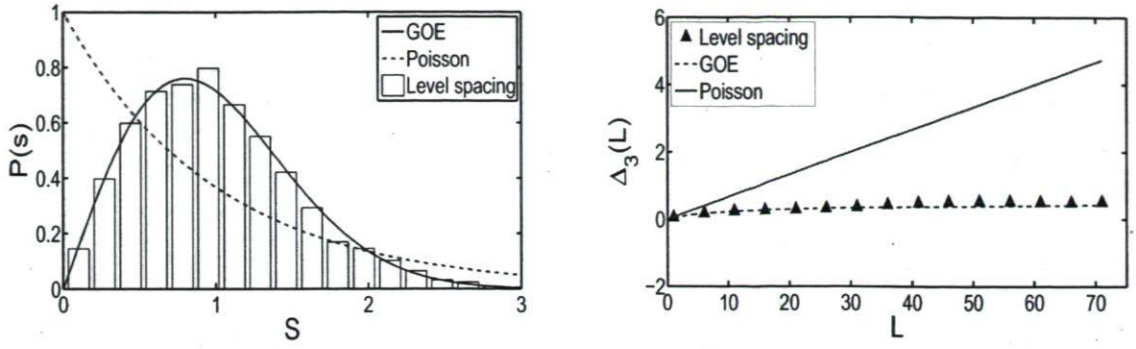

Figure 6.12: Optical billiard: Nearest-neighbor level spacing distribution $P(s)$ for $N_{\text{bound}} = 65$ boundary nodes and $N_{\text{reb}} = 8$ rebounds (left panel). Correlation coefficient $C = -0.27 \pm 10^{-10}$ is in agreement with GOE behavior. Spectral rigidity $\Delta_3(L)$ (right panel) [148].

that the spectral properties of these systems exhibit a GOE-behavior, i.e. they are universal. Furthermore, they (particularly the bounded model of the Lorentz gas) follow a random-walk motion which confirms the CLT.

Chapter 7

Diffusive Properties of the Lorentz Gas

In this chapter, we discuss the diffusion of the Lorentz gas. It is a transport property in dynamical systems, which has attracted a remarkable interest in various domains of microscopic and macroscopic physics.

The diffusion properties of the Lorentz gas have been studied in several approaches in the literature. For example, Gaspard and Nicolas [149] obtained the dependency of the diffusion coefficient on the escape rate of the point-particle from a limited region of hard disks. The escape rate was computed in terms of the Kolmogorov-Sinai entropy and the positive Lyapunov exponents. Through these two dynamical parameters, they determined a fractal set of trajectories of the particle (called "repellers"), trapped in a restricted region. The results for non-equilibrium statistical mechanics presented in Ref. [149], showing the relation between the diffusion, the dynamical randomness and the sensitivity to initial conditions.

Also, Machta and Zwanzig [151] investigated the self-diffusion process of a point-particle in a Lorentz gas with triangular symmetry. Their method was based on the idea that the exact motion of the particle can be treated as a random walk between triangular trapping regions (see Fig.[6.2]). They hypothesized that in high densities, where the test-particle bears a large number of collisions in trapping cells, the sequence of traps visited by the particle is a Markov chain. By the assumption of ergodicity of the periodic Lorentz gas in high densities [138, 150], they computed the average time spent in cells and, by this parameter, they estimated the diffusion coefficient of the system in terms of the width of channels between neighboring disks [151]. Their numerical simulations and analytical results were in a good agreement.

In addition to the above methods, Borgonovi et al. [152] explored the diffusion in classical chaotic billiards via angular momentum. They studied the diffusive process in angular momentum for the Bunimovich stadium, by calculating this quantity of an ensemble of 10^4

moving particles, with random locations on the boundary of the stadium. In order to evaluate the diffusion constant $\mathcal{D}$, they computed the variance of angular momentum $\Delta\hat{L}^2$ of particles as a function of the number of collisions N_{col} . Their results show that $\Delta\hat{L}^2$ increases diffusively with N_{col}, compatible with $\Delta\hat{L}^2 = \mathcal{D}\, N_{\text{col}}$. They suggest that the diffusion in terms of angular momentum may be interesting for some optical resonators [152].

On the other hand, perhaps the most common scheme for the diffusion coefficient is given by Einstein formula [153], which is based on the context of the Brownian motion. It shows a linear increase of the variance of the particle's positions, indicating that the asymptotic behavior of the particle trajectories follows the CLT, and is a signature of a random walk (Brownian motion). Later, Green and Kubo [153] found that the Einstein equation can also be represented by the particle's velocity auto-correlation function. In what follows, we refer to the Einstein-Green-Kubo equation for closed and open regimes of the Lorentz gas.

7.1 Behavior of the diffusion coefficient in the finite and the infinite-horizon regimes

To show how the diffusive process behaves in closed and open systems, we take a brief look on the most general formulation of transport coefficients of the Lorentz gas (e.g. the Diffusion constant). It is the Einstein-Green-Kubo formulation [154, 155], which is basically a temporal correlation function method. In that approach, which relates the diffusion constant to the diffusion equation, one obtains

$$\left\langle |\Delta\mathbf{r}(t)|^2 \right\rangle \sim 2\mathrm{d}\, \mathcal{D}\, t\,, \tag{7.1}$$

where t is the time, d is the space dimension, $\mathcal{D}$ denotes the diffusion coefficient, and $\left\langle |\Delta\mathbf{r}(t)|^2 \right\rangle = \left\langle |\mathbf{r}(t) - \mathbf{r}(0)|^2 \right\rangle$ indicates the mean square displacement of particles.

In fact, Eq.(7.1) is a result of the Fokker-Planck equation together with the diffusion equation for the Brownian particles in fluids [137]. Here let us illustrate this in some detail.

The Fokker-Planck equation (as a special case of the Chapmann-Kormogorov equation [137]) in one dimension is given by

$$\frac{\partial P(x,t)}{\partial t} = -\frac{\partial}{\partial x}A(x)P(x,t) + \frac{1}{2}\frac{\partial^2}{\partial x^2}B(x)P(x,t)\,, \tag{7.2}$$

where $P(x,t)$ is a probability density function in the range $y \in (-\infty, +\infty)$, and x stands for the position of particles. The coefficients $A(x)$ and $B(x) > 0$ can be any real differentiable

function. For the Markov processes, these two coefficients are characterized by

$$A(x) = \frac{\langle \Delta x \rangle}{\Delta t} \quad , \quad B(x) = \frac{\left\langle (\Delta x)^2 \right\rangle}{\Delta t} \, . \tag{7.3}$$

In the case of the Brownian motion, the Brownian particle makes random walks and these random jumps may have any length, but the probability for large jumps falls off rapidly. Furthermore, the probability is symmetrical and independent of the starting point [137]. Accordingly,

$$A = \frac{\langle \Delta x \rangle_x}{\Delta t} = 0 \quad , \quad B = \frac{\left\langle (\Delta x)^2 \right\rangle_x}{\Delta t} = \text{const.} \, . \tag{7.4}$$

Hence, the Fokker-Planck equation for the random walk transition is:

$$\frac{\partial P(x,t)}{\partial t} = \frac{B}{2} \frac{\partial^2 P(x,t)}{\partial x^2} \, , \tag{7.5}$$

which has the same functional form as the diffusion equation for the Brownian particles in fluids, i.e.

$$\frac{\partial P(x,t)}{\partial t} = \mathcal{D} \frac{\partial^2 P(x,t)}{\partial x^2} \, . \tag{7.6}$$

comparing the last two equations one concludes that

$$\mathcal{D} = \frac{\left\langle (\Delta x)^2 \right\rangle_x}{2\Delta t} \, , \tag{7.7}$$

which is known as the Einstein relation for diffusion constant (in one dimension).

7.1.1 The Green-Kubo formula

In general, the displacement of particles can be represented by [133, 155]

$$\mathbf{r}(t) - \mathbf{r}(0) = \int_0^t \mathbf{v}(t') dt' \, . \tag{7.8}$$

Therefore from Eq.(7.1) one has:

$$\mathcal{D}(t) = \frac{1}{2t\,\mathrm{d}} \int_0^t \int_0^t \langle \mathbf{v}(t').\mathbf{v}(t'') \rangle \, dt' dt'' =$$
$$\frac{1}{\mathrm{d}} \int_0^t \langle \mathbf{v}(0).\mathbf{v}(\tau) \rangle \, d\tau - \frac{1}{t\mathrm{d}} \int_0^t \langle \mathbf{v}(0).\mathbf{v}(\tau) \rangle \, \tau d\tau \, , \tag{7.9}$$

where an integration by parts has been performed in the second part. In the limit of $t \to \infty$, one evaluates the diffusion coefficient as

$$\mathcal{D} = \lim_{t\to\infty} \frac{1}{\mathrm{d}} \int_0^t \langle \mathbf{v}(0).\mathbf{v}(\tau) \rangle \, d\tau \equiv \lim_{t\to\infty} \frac{\left\langle |\mathbf{r}(t) - \mathbf{r}(0)|^2 \right\rangle}{2t\,\mathrm{d}} \, . \tag{7.10}$$

which is called the Einstein-Green-Kubo formula.

In a discrete dynamics, one can replace the continuous-time t by the number n of collisions to the system's scatterers. Hence the discrete form of the above formula is given by

$$\mathcal{D} = \lim_{n\to\infty} \frac{\left\langle |\mathbf{r}_n - \mathbf{r}_0|^2 \right\rangle}{2n\,\mathrm{d}} = \frac{1}{2\mathrm{d}} \left\langle |\Delta\mathbf{r}_0|^2 \right\rangle + \frac{1}{\mathrm{d}} \lim_{n\to\infty} \sum_{i=1}^{n} \langle \Delta\mathbf{r}_0 . \Delta\mathbf{r}_i \rangle \ , \tag{7.11}$$

where the relation

$$\mathbf{r}_n - \mathbf{r}_0 = \sum_{i=0}^{n-1} (\mathbf{r}_{i+1} - \mathbf{r}_i) = \sum_{i=0}^{n-1} \Delta\mathbf{r}_i \tag{7.12}$$

has been utilized [155]. Note that $\Delta\mathbf{r}_0$ is the displacement of the particle before its first collision.

7.1.2 Some general aspects

Bunimovich and Sinai [138] found that in the finite-horizon regime, the statistical behavior of trajectories is such that the displacement $\mathbf{r}(t) - \mathbf{r}(0)$ follows the CLT. This means that the distribution

$$\varrho_{\mathrm{fin}} = \lim_{t\to\infty} \frac{|\mathbf{r}(t) - \mathbf{r}(0)|}{\sqrt{t}} \tag{7.13}$$

is a Gaussian, and

$$f(\xi) = \lim_{t\to\infty} \frac{|\mathbf{r}(\xi t) - \mathbf{r}(0)|}{\sqrt{t}} \tag{7.14}$$

resembles a Brownian motion. The discrete version of the distribution ϱ_{fin} becomes

$$\varrho_{\mathrm{fin}} = \lim_{n\to\infty} \frac{|\mathbf{r}_n - \mathbf{r}_0|}{\sqrt{n}} \ . \tag{7.15}$$

On the other hand, the situation for the case of the infinite-horizon is different. In this regime, according to numerical evidence [156], the velocity auto-correlation function is characterized by [155]

$$\langle \mathbf{v}(0), \mathbf{v}(t) \rangle \sim \frac{const.}{t} \ . \tag{7.16}$$

Consequently,

$$\mathcal{D} = \lim_{t\to\infty} \frac{\left\langle |\mathbf{r}(t) - \mathbf{r}(0)|^2 \right\rangle}{2t\,\mathrm{d}} \sim const. \log t \ . \tag{7.17}$$

This shows that in the limit of $t \to \infty$, the diffusion coefficient goes to infinity, which reflects a so-called "super-diffusive" behavior of trajectories $\mathbf{r}(t)$. The direct conclusion of Eq.(7.17) is that the diffusion coefficient in the infinite-horizon regime becomes a finite value, provided that one normalizes this equation through dividing it by a factor $\log t$. Bleher [155] based

on the numerical results by Friedman et al. [156], proved that for a periodic system with the infinite horizon, the distribution

$$\varrho_{\text{inf}} = \lim_{t\to\infty} \frac{|\mathbf{r}(t) - \mathbf{r}(0)|}{\sqrt{t \log t}} \tag{7.18}$$

exists, and it is a Gaussian distribution. This logarithmic normalization yields a so-called super-diffusion coefficient $\widetilde{\mathcal{D}}$ as following

$$\widetilde{\mathcal{D}} = \frac{1}{2\text{d}} \left\langle \left| \lim_{n\to\infty} \frac{\mathbf{r}_n - \mathbf{r}_0}{\sqrt{n \ln n}} \right|^2 \right\rangle , \tag{7.19}$$

which is a discrete formalism in terms of the number n of bounces.

7.2 Diffusion coefficient via the length of trajectory

Here we discuss the diffusion coefficient in terms of the trajectory's length, within a trapping zone between three disks. In Chapter 6 we saw that in the finite-horizon regime, the distribution $P(\Lambda)$ of length of trajectories follows the CLT, which is also the case for random walk and Brownian motion [133]. Following such a random walk, the length of a trajectory after N_{reb} rebounds is simply given by

$$\Lambda = \sum_{n=1}^{N_{\text{reb}}} \lambda_n , \tag{7.20}$$

where λ_n denotes the free path length between successive collisions. In fact, the so-called steps lengths λ_n are random numbers from a probability distribution function $P(\lambda)$ [133]. In this context, the CLT defines a normal diffusion constant $\mathscr{D}$, given by [133, 134]

$$\mathscr{D} = \frac{< \lambda^2 > - < \lambda >^2}{2\,\tau} , \tag{7.21}$$

where $< \lambda >$ and $< \lambda^2 >$ are the first two moments of $P(\lambda)$ [1] , and τ is the travel time along the average step length $\langle\lambda\rangle$ (notice that $\lambda = \langle\lambda_n\rangle$, and $\tau = \langle\tau_n\rangle$). Due to the elastic collisions with scatterers, the value of the point-particle's velocity u is constant, which is defined by

$$u = \frac{\langle\lambda_n\rangle}{\tau_n} \equiv \frac{\lambda}{\tau} . \tag{7.22}$$

This velocity is usually assumed to be unity [120].

[1] The moments of λ are determined from $P(\lambda)$, through[133]:

$$< \lambda^n > = \int_{-\infty}^{+\infty} d\lambda\, \lambda^n\, P(\lambda)$$

Now let us consider the variance of the total length Λ. Then one can write [135]

$$< \Lambda^2 > - < \Lambda >^2 = \sum_{m=1}^{N_{\rm reb}} \sum_{n=1}^{N_{\rm reb}} [\langle \lambda_m \lambda_n \rangle - \langle \lambda_m \rangle \langle \lambda_n \rangle] = \sum_{m=1}^{N_{\rm reb}} \sum_{n=1}^{N_{\rm reb}} C_{mn} \,, \tag{7.23}$$

where C_{mn} stands for the correlation function of the lengths λ_m and λ_n . By assuming that λ_n's are uncorrelated, one has [135]

$$C_{mn} = \left[< \lambda^2 > - < \lambda >^2 \right] \delta_{mn} \,. \tag{7.24}$$

and therefore

$$< \Lambda^2 > - < \Lambda >^2 \equiv N_{\rm reb} \left[< \lambda^2 > - < \lambda >^2 \right] \,. \tag{7.25}$$

Then, by the use of Eq.(7.21) this leads to

$$< \Lambda^2 > - < \Lambda >^2 = 2 \mathscr{D} N_{\rm reb} \, \tau \,. \tag{7.26}$$

As a consequence, the diffusion constant is characterized by the variance of trajectory's length as

$$\mathscr{D} = \frac{Var(\Lambda)}{2T} \,, \tag{7.27}$$

where T is the total travel-time (i.e., $T = N_{\rm reb} \, \tau$). Since the total time T is proportional to both $< \Lambda >$ and $N_{\rm reb}$, therefore, we can define an effective diffusion constant as [2]

$$\mathscr{D}_\Lambda \sim \frac{Var(\Lambda)}{N_{\rm reb}} \,, \tag{7.28}$$

or equivalently

$$\mathscr{D}_\Lambda \sim \frac{Var(\Lambda)}{\langle \Lambda \rangle} \,. \tag{7.29}$$

7.2.1 Diffusion in the finite-horizon and localized regimes

For the practical evaluation of the diffusion parameter $\mathscr{D}_\Lambda$, we construct an ensemble of trajectories, starting from a sequence of boundary nodes, chosen as random points, as well as a given number of collisions at the boundary of moving zone. Here, we take a set of rebound numbers $N_{\rm reb} = \{10, 20, ..., 70\}$, and we separately compute the average variance of the length of trajectories $\langle Var(\Lambda) \rangle$. We consider a range of values for σ in the finite-horizon regim, i.e. $\sigma = \{2.01, \; 2.05, \; 2.10, \; 2.15, \; 2.20, \; 2.25, \; 2.30\}$.

From the results, we observe that in the case of the finite-horizon, $Var(\Lambda)$ behaves as a linear function of the number of rebounds $N_{\rm reb}$ (See the left part of Fig.[7.1]). A similar

[2] We eliminate the constant parameters such as the velocity u of the point-particle, the mean free time τ and the pre-factor 2, because we look for the general behavior of the diffusion parameter.

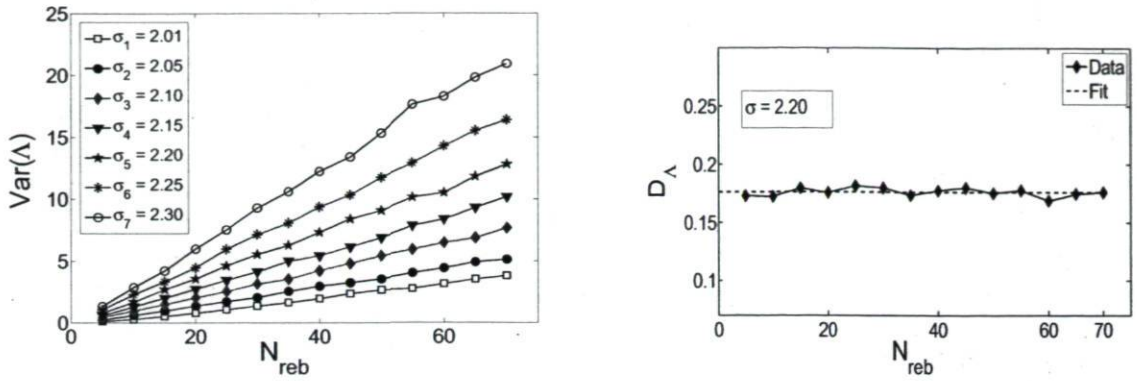

Figure 7.1: The finite-horizon regime. Left panel: Variance $Var(\Lambda)$ versus the number of rebounds for a variety of σ values. The linear behavior is consistent with the global behavior of the diffusion coefficient of the closed Lorentz gas. Right panel: Diffusion coefficient in the finite regime (for $\sigma = 2.20$) in terms of the number of collisions, indicating small fluctuations around a constant value [72, 144].

behavior shows up when we plot $Var(\Lambda)$ versus the average length $\langle\Lambda\rangle$ (not shown here). This linearity suggests a finite value to the tangent of this curve, which is proportional to $\mathscr{D}_\Lambda$. This is consistent with the results of the Einstein-Green-Kubo, as well as Machta-Zwanzig [151] formulae, and also the results of Borgonovi et al. [152]. In addition, it shows that the diffusion coefficient $\mathscr{D}_\Lambda$ does not depend on N_{reb} (or $\langle\Lambda\rangle$) in the finite-horizon regime. Fig.[7.1] (right panel) confirms this for $\mathscr{D}_\Lambda$, showing small fluctuations around a constant value.

In the localized (dense packing) regime, on the other hand, essentially there is no diffusion. The reason is that the moving-particle is unable to travel beyond the trapping zone (Fig.[7.2]). Hence the diffusion coefficient is nearly zero, as shown in Fig.[7.3].

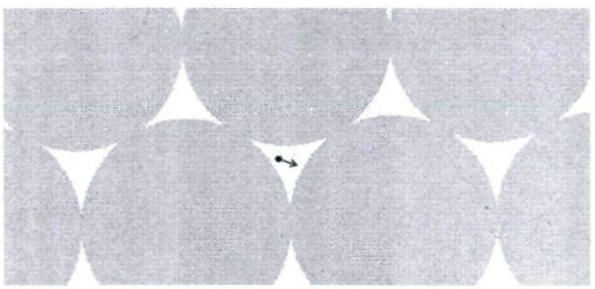

Figure 7.2: The moving zone between adjacent disks in the case of the localized regime of the 2D Lorentz gas. The point particle is trapped in this zone.

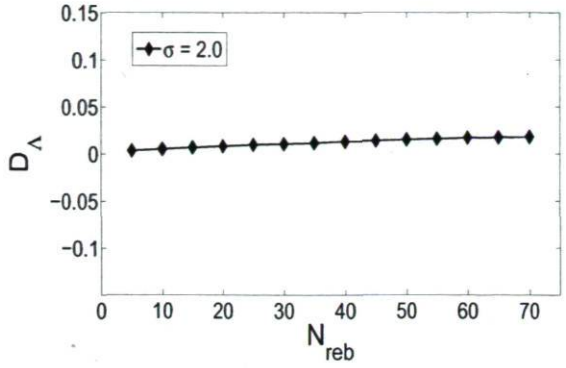

Figure 7.3: Diffusion in the localized regime. The diffusion coefficient D_Λ is near zero, indicating that no diffusion occurs in this case of the Lorentz gas [144].

7.2.2 The infinite-horizon and diffusion

In the case of the infinite-horizon, the situation of the length variance $Var(\Lambda)$ is different. As Fig.[7.4] (left panel) shows, for densities distant from the finite horizon regime (e.g. σ = 2.70, 2.90 in this figure), the behavior of $Var(\Lambda)$ is governed by large noise. It rapidly diverges to large values, in a fluctuating fashion. Therefore, one cannot extract a diffusion parameter $\mathscr{D}_\Lambda$ from such a behavior. The reason is that, in this regime the point-particle can

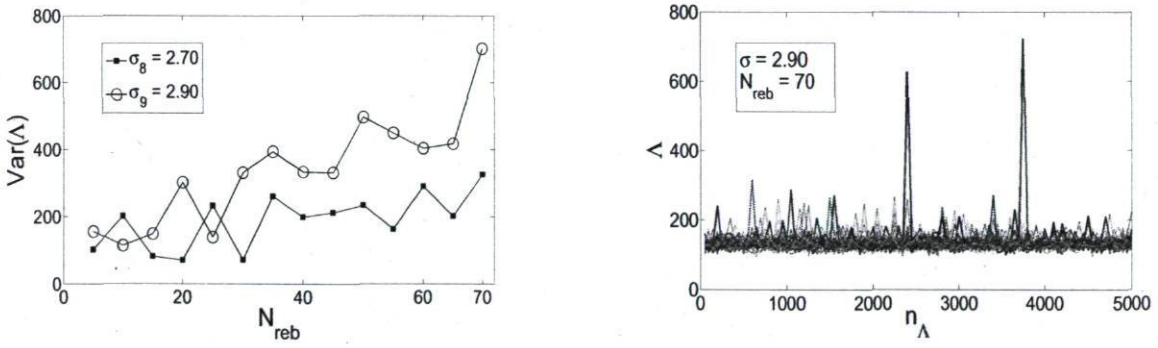

Figure 7.4: The infinite-horizon regime. Left: Variance of trajectory's length with respect to the number of rebounds. Right: Length of trajectories for σ = 2.9 and N_{reb} = 70. In a number of n_Λ = 5000 trajectories (a set of 50 boundary points with 100 number of trajectories for each initial point) there are a few large spikes (e.g. two values of $\Lambda > 600$ while $\langle\Lambda\rangle \sim 135$), which create large fluctuations in Var(Λ) [144].

travel large distances (in comparison to to the finite-horizon case) in some corridors, without colliding with hard disks. In our simulation, such a behavior of the particle is manifested by the numerous collisions with the straight parts of the boundary. For instance, Fig.[7.5] shows a trajectory in the case of σ = 3.0. In this example, the number of bounces with disks scatterers (curved sections) is fixed to be N_{reb} = 8 . Nevertheless, the point-particle

also collides 22 times with the straight walls. As consequence, such behavior generates

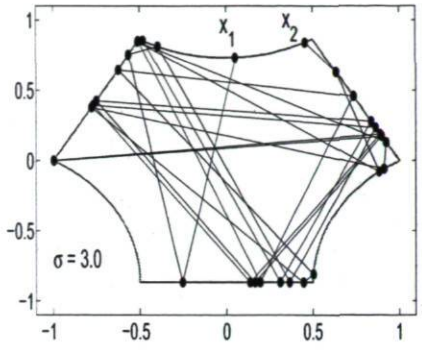

Figure 7.5: The infinite-horizon regime: a sample trajectory of the moving-particle for σ = 3.0 and N_{reb} = 8 (collisions with disks), between the initial and final points x_1 and x_2. The high number of collisions with the straight parts (in comparison to the finite-horizon case), is the reason of large spikes in Var(Λ), shown in Fig.[7.4].

some large spikes in Λ (see Fig.[7.4], right panel), which is the source of fluctuations in the length variance. In order to minimize such (physical) noises and study the global behavior of $Var(\Lambda)$, one needs to consider large ensembles of the length of trajectories. Such ensembles, however, must contain a huge number of members (i.e., Λ's), for computing their variance through a statistical averaging approach.

As discussed in Section 7.1.2, when going from the finite to the infinite horizon regime, it has been conjectured that the Lorentz gas undergoes a change in behavior [155, 156, 157, 158]. In particular, the normal diffusion has been predicted to switch to the anomalous diffusion, where the variance of position (versus the number of rebounds) scales with a logarithmic normalization factor (see Eqs.(7.17,7.19)). It would be interesting to verify this hypothesis for the triangular periodic Lorentz gas, using the length of trajectories. Let us mention that such a behavior of the diffusion constant has been also theoretically predicted for the Bunimovich stadium billiard via mathematical approaches [132]. It has been numerically shown by studying the variance of the length of trajectories [72]. However, at the present time we are working on this hypothesis for the Lorentz gas, to verify if any logarithmic behavior of the length variance $Var(\Lambda)$ exists or not.

Chapter 8

Remarks and Discussion

Part I In the first part, we studied the $U(1)_{2+1}$ lattice gauge theory (LGT) by characterizing the spectrum of that model via the Monte Carlo Hamiltonian (MCH). In general, the construction of a Hamiltonian in LGT raises the following points:

(a) Although there exists the Kogut-Susskind lattice Hamiltonian, the problem is how to compute physical observables, such as energy spectra, etc. We suggest here the approach of constructing an effective Hamiltonian. This is meant to be a Hamiltonian which describes physics in a finite window (e.g. a window of low energy). This has some analogy to the idea of the Wilson-Kadanoff renormalization group, where a renormalized Hamiltonian is constructed, which is valid for some critical point.

(b) In conventional Hamiltonian methods familiar in nuclear physics, condensed matter, particle physics and generally in many-body physics, it is customary to consider a given Hamiltonian $\mathcal{H}$ and compute matrix elements $\langle \Psi_i | \mathcal{H} | \Psi_j \rangle$ from such a Hamiltonian. In contrast, here we consider a function of the Hamiltonian, i.e. $\exp[-\mathcal{H}T/\hbar]$. This has the following advantages: First, $\mathcal{H}$ is mathematically a more singular object than $\exp[-\mathcal{H}]$. This can be seen in the simple quantum mechanical example of the electric Hamiltonian $\mathcal{H}^{\text{elec}}$. The matrix element $\langle y | \mathcal{H} | x \rangle$ is a derivative of a δ-function, while the matrix element $\langle y | \exp[-\mathcal{H}] | x \rangle$ is a smooth, differentiable and rapidly falling-off function. This means that the non-linear exponential function smoothes out the singularities of an operator. Second, matrix elements of the exponential function $\exp[-\mathcal{H}T/\hbar]$ can be evaluated by using the path integral. Third, in comparison to $\mathcal{H}$, the operator function $\exp[-\mathcal{H}T/\hbar]$ contains a parameter T, which is redundant for the physical spectrum, i.e., one should obtain the same spectrum of $\mathcal{H}$, using any value of T. However, in numerical simulations this is not quite so. The results do depend on the value of T. They depend also on physical parameters, such as coupling, lattice size and lattice spacing and so on. They as well depend on approximation parameters, such as

the number of equilibrium configurations used in the path integral, the size of the stochastic basis, etc. Last but not least, they depend on the internal precision of computers. Here we can turn the dependence on T into an advantage: the T-dependence of the energy spectrum (or better of a number of low lying energy eigenvalues) can serve as a measure of error of the calculation. In the best case, the energy eigenvalues become T independent. This happens in the so-called scaling windows. In the worst case, they are strongly T-dependent, meaning that these results are unphysical.

(c) Stochastic basis. In our opinion, the construction of a suitable basis is the most important step in order to compute physics from a Hamiltonian. Such a basis is built on two principles: first a random selection of basis states and second, a physical principle to guide the search. The so-called stochastic basis is built in close analogy to the equilibrium path configurations computed via the method of Monte Carlo with importance sampling, in order to solve Lagrangian LGT.

(d) In contrast to the Lagrangian LGT, where gauge symmetry is manifestly conserved in the path integral via the group measure as well as the Wilson action, in the Hamilton formulation, the gauge invariance of states and amplitudes has to be imposed via Gauss' law. Technically, much work is required to construct such a gauge invariant states. One expands the link Bargmann states into irreducible representations, using the Peter-Weyl theorem. Gauge invariant states are then constructed by doing the group integral of local gauge transformations at each vertex. As a result one enforces Gauss' law at each vertex. Here, we have shown how this can be done in the case of U(1) gauge theory. This can be generalized to non-Abelian gauge symmetry. For example, Burgio et al. [107] have shown how to construct a gauge invariant Hilbert space for the gauge group SU(2).

(e) By working on some small size lattices, we have shown that the MCH with stochastic basis works well in $U(1)_{2+1}$ LGT. We have verified that the MCH is able to provide the spectrum and the corresponding wave functions in some finite energy window, which is a hard problem in the Lagrangian lattice approach. Moreover, physical observables such as thermodynamical functions can be easily computed from energy windows of the MCH, while it is difficult via traditional Lagrangian formulation. In addition to the previous applications of this method in quantum mechanics and scalar field theory, we claim that U(1) LGT is another signature of advantages of this technique.

(f) We believe that the physical observables on larger lattices can also be measured in the MCH approach. This requires using powerful parallel algorithms for the computation of the electric transition amplitudes, and reducing statistical errors of the Monte Carlo with importance sampling (in the evaluation of ratios of path integrals), by use of adequate computational resources.

Part II In the second part, we studied the chaotic behavior of the classical 2D Lorentz gas via random matrix theory. We develop the level spacing statistics by constructing a length matrix of some trajectories of a point-particle, confined in a lattice of fixed rigid disks with a triangular symmetry. Via this matrix, which is symmetric and Hermitian, we compute the NNS distribution $P(s)$, the spectral rigidity $\Delta_3(\ell)$, as well as the spacing auto-correlation function of the system. The numerical experiments with 2D Lorentz gas in the case of the finite horizon, led us to the following observations:

(i) For a given pair of boundary points, the numerical errors take an exponential behavior as a function of the number of rebounds of the moving-particle with hard scatterers. Such behavior is not found in the integrable systems. Therefore, it can be considered as a signature of chaos in chaotic systems.

(ii) The distribution $P(s)$ of nearest neighbor level spacing (NNS) fluctuations, obtained from eigenvalues of the length matrix Λ, indicates a Wignerian distribution. This is consistent with the GOE behavior predicted by the random matrix theory.

(iii) The spectral rigidity $\Delta_3(\ell)$ and the correlation function C, also obtained from the spectrum of length matrix Λ, are in agreement with GOE statistics, as well.

(iv) In comparison to the functions $P(s)$ and $\Delta_3(\ell)$, where unfolding has eliminated much physical information about the system, more information is maintained in the distribution $P(\Lambda)$ of length matrix elements. For example, it was found to tend to a Gaussian, in the limit $N_{\text{reb}} \to \infty$ (i.e. for macroscopic times), which is also the case for the random walk model (Brownian motion). Such behavior is predicted by rigorous mathematical results on the central limit theorems (CLT), in the case of the periodic Lorentz gas [138, 139], and in the case of the stadium billiard [141]. Furthermore, there is numerical evidence for such behavior from the modeling of the cardioid billiard [72]. From the modeling point of view, answering such a question is computationally quite expensive, because increasing the number of rebounds requires to increase the internal arithmetic precision (i.e. the scale of arithmetic resolution). If one would find that $P(\Lambda)$ ultimately becomes a Gaussian, then it would mean that presumably more classically chaotic systems show the CLT behavior than those few where rigorous proofs exist.

(v) In the case of the infinite-horizon, the NNS distribution $P(s)$ and the Dyson-Mehta rigidity $\Delta_3(\ell)$ obey the GOE-statistics, denoting the chaoticity of the system. But, the length distribution $P(\Lambda)$ exhibits some deviations from a Gaussian form, which arises from long free paths of the moving-particle. Such difference with the Gaussian function indicates that $P(\Lambda)$ does not follow the standard CLT. However, its resemblance to the normal distribution says that possibly there is a limit theorem in this regime of the Lorentz gas.

(vi) We have also studied a 2D billiard, composed by optical media located in a Bunimovich stadium. Such a model is similar to a chaotic potential system. We have computed the time-of-travel matrix and its spectrum and performed a statistical fluctuation analysis. Likewise the Lorentz gas, for this system we found that the nearest-neighbor spacing distribution, spectral rigidity and the correlation coefficient are consistent with the GOE-statistics, consistent with random matrix theory. In addition, the histogram $P(\mathcal{T}_{ij})$ of the travel-time matrix elements is close to a Gaussian.

(vii) The above conclusions for $P(\Lambda)$, $P(s)$, $\Delta_3(\ell)$, as well as the auto-correlation function C, results out a universal behavior of the two classical systems in question (i.e. the Lorentz gas and the optical billiard). All the work establishing universality in classical chaos via correlation functions of periodic orbits, is based on classical periodic orbits (for example, see Ref. [70]). However, in our study of classical chaotic billiards, universality can be also observed based on non-periodic bouncing trajectories.

If one considers classically chaotic billiards in the regime of universality, where $P(\Lambda)$ asymptotically approach a Gaussian and Λ becomes a random matrix from a GOE, then one can compute physical observables. For example, we studied the diffusion coefficient of the Lorentz gas using the trajectory length of the point-particle. We computed the variance of length $\Delta\Lambda^2$ of trajectories, and achieved the following observations:

(a) In the finite-horizon (bounded) regime, we found that there is a linear relation between the variance of length, and the number of collisions of the particle with rigid scatterers. Due to this property, we can define a normal diffusion in the case of the finite-horizon model. It is compatible with the global behavior of the customary diffusion coefficient obtained from other formulations, such as Green-Kubo [120, 155] and Machta-Zwanzig [151] formulas.

(b) In the localized regime, the variance of the trajectory length is roughly zero. This means that in this case essentially there is no diffusion. This confirms that the particle is caught in the trapping zone and is unable to leave this area.

(c) For the infinite-horizon, due to numerical fluctuations originated from long free motions, the variance displays an irregular feature with respect to the number of bounces. As discussed in chapter 7, theoretically the standard diffusion constant in this regime goes to infinity, but based on theoretical predictions it should be a finite value (anomalous diffusion) after a logarithmic correction. In Ref. [72], we have numerically justified that the Bunimovich stadium billiard displays such a behavior. However, for the Lorentz gas, there is no conclusive numerical evidence in literature related to this subject, and also our present computational tools have not yet allowed us to make a definitive statement on a logarithmic behavior. Nevertheless, this may be a subject of further research.

Appendix A

Peter-Weyl Theorem

Invariant subspaces: Suppose R is a representation of a gauge group G on a vector space $\mathcal{V}$, and $\mathcal{V}^S$ is a subspace of $\mathcal{V}$. The subspace $\mathcal{V}^S$ is invariant with respect to $R(g)$ if and only if $R(g)\mathcal{V}^S \subset \mathcal{V}^S$ for all $g \in G$. For any R, the vector space $\mathcal{V}$ itself and the subspace $\{0\}$, are trivially invariant [159].

Irreducible representations: If an invariant subspace $\mathcal{V}^S$ contains just trivial invariant subspaces, then it is a minimal or proper subspace. In such case, the corresponding representation $R(g)$ on $\mathcal{V}$ is called "irreducible" [108, 159]. In other words, it is a representation with the lowest possible dimension. Every representation can be characterized as a direct sum of irreducible representations. This means that there is at least one trivial invariant subspace $\mathcal{V}^S$. For example, one can refer to any representation of G on a non-zero one-dimensional complex vector space, in which there is no place for any subspace between $\{0\}$ and $\mathcal{V}$.

As another example, let us consider the rotation group SO(2), which is characterized by the rotational operator $U(\phi)$ on a finite-dimensional vector space $\mathcal{V}$. For an infinitesimal angle ϕ, the rotation operator is given by

$$U(\phi) = e^{-i\phi J} \,. \tag{A.1}$$

where J is the angular momentum operator. Now, for any integer vector $|m\rangle$ in a trivial invariant subspace of SO(2) and considering $J|m\rangle = m|m\rangle$ one writes

$$U(\phi)|m\rangle = e^{-im\phi}|m\rangle \,, \tag{A.2}$$

where m is an integer number.

According to the theorem 6.4 in Ref. [108], the single valued irreducible representations of SO(2) are given by $J = m$, where m is any integer. These representations are identified by

$$U(\phi) = e^{-im\phi} \,. \tag{A.3}$$

For instance, when $m = 0$, then $U(\phi) = 1$ which is the identity representation. In the case of $m = \pm 1$, one has $U(\phi) = e^{\pm i\phi}$ which covers once the unit circle in the clockwise for $m = +1$ (and the opposite direction for $m = -1$) for the rotation over group space ($\phi : 0 \to 2\pi$).

Peter-Weyl theorem: If G is a compact Lie group, then the matrix elements of finite dimensional irreducible representations of G form a complete set of orthogonal vectors in the space $L^2(G)$[1], i.e. they construct a Hilbert basis for $L^2(G)$ [159].

Notice that

$$\int_G [d\mathscr{G}]\, |\Phi(\mathscr{G})|^2 < +\infty \,, \qquad \mathscr{G} \in G \,, \tag{A.4}$$

and the inner product is

$$\langle \Phi |\, \Psi \rangle \;=\; \int_G [d\mathscr{G}]\, \Phi(\mathscr{G})\, \overline{\Psi}(\mathscr{G}) \,, \quad \Phi, \Psi \in L^2(G) \,, \tag{A.5}$$

where $[d\mathscr{G}]$ is the normalized invariant group measure. A complete proof of this theorem can be found in Ref. [159]. Here we bring a few examples of this theorem.

The irreducible representation matrices $D^{\mu}(\mathscr{G})$[2] of the groups SU(2), SO(2) and SO(3) form a complete basis in the space of square integrable functions.

In the case of SU(2) the orthonormality condition

$$(2j+1) \int [d\mathscr{G}]\, D^{\dagger}_{j}(\mathscr{G})^{m}_{n}\, D^{j'}(\mathscr{G})^{n'}_{m'} = \delta^{j'}_{j}\; \delta^{n'}_{n}\; \delta^{m}_{m'} \tag{A.6}$$

holds for the irreducible representation matrices $D^{j}(\mathscr{G})$ [108]. Beside this orthonormal property, the rotation matrices $D^{j}(\mathscr{G})^{m}_{n}$ construct a complete basis in the space of square integrable functions $\Phi(\mathscr{G})$ defined on the group manifold:

$$\Phi(\mathscr{G}) = \sum_{j\, m\, n} \Phi^{n}_{j\, m}\, D^{j}(\mathscr{G})^{m}_{n} \,. \tag{A.7}$$

---

[1] $L^2(G)$ denotes on the infinite dimensional Hilbert space of square integrable functions Φ defined on the group manifold.

[2] In the case of finite-dimensional representaton, by choosing a set of basis vectors $|e_i\rangle$ on the vector space $\mathcal{V}$ the operators $R(\mathscr{G})$ are realized as $n \times n$ matrices $D^{\mu}(\mathscr{G})$ in the μ-representation, where $U(\mathscr{G})\,|e_i\rangle = |e_i\rangle\, D^{\mu}(\mathscr{G})^{j}_{i}$, $\mathscr{G} \in G$, $i, j = 1, ..., n$. The orthonormality condition of these matrices is $\dfrac{n_\mu}{n_G} \displaystyle\sum_{\mathscr{G}} D^{\dagger}_{\mu}(\mathscr{G})^{k}_{i} D^{\nu}(\mathscr{G})^{j}_{l} = \delta^{\nu}_{\mu} \delta^{j}_{i} \delta^{k}_{l}$, where n_G is the order of group and n_μ is the dimension of the μ-representation.

According to Eq.(A.6) one obtains

$$\Phi^n_{j\,m} = (2j+1)\int [d\mathscr{G}]\, D^\dagger_j(\mathscr{G})^n_m\, \Phi(\mathscr{G})\,. \tag{A.8}$$

Combining this equation with Eq.(A.7) yields

$$\sum_{j\,m\,n}(2j+1)\, D^j(\mathscr{G})^m_n\, D^\dagger_j(\mathscr{G})^n_m = \delta(\mathscr{G}-\mathscr{G}')\,. \tag{A.9}$$

As a special case, if one considers the parametrization of SU(2) in terms of the Euler angles, then

$$\delta(\mathscr{G}-\mathscr{G}') = 16\pi^2\,\delta(\alpha-\alpha')\,\delta(\cos\beta-\cos\beta')\,\delta(\gamma-\gamma')\,. \tag{A.10}$$

The rotation operators $U^n(\phi)$ of the compact group SO(2) also fulfills the orthonormality and completeness relations (Theorem 6.6 in Ref. [108])

$$\begin{aligned} &\frac{1}{2\pi}\int_0^{2\pi} d\phi\; U^\dagger_n(\phi)\, U^m(\phi) = \delta^m_n && \text{(orthogonality)} \\ &\sum_n U^n(\phi)\, U^\dagger_n(\phi') = \delta(\phi-\phi') && \text{(completeness)}\,. \end{aligned} \tag{A.11}$$

The situation is similar to the gauge group U(1), because it is locally isomorphic [3] to the group U(1). Notice that when $U^n(\phi) = e^{-in\phi}$, the above theorem is equivalent to the Fourier transform of periodic functions.

In the case of the group SO(3) one can also obtain the completeness relation of spherical harmonics $Y_{l\,m}$ over the space of square integrable functions defined on the unit sphere as

$$\sum_{l\,m} Y_{lm}(\theta,\phi)\, Y^\star_{lm}(\theta',\phi') = \delta(\cos\theta-\cos\theta')\,\delta(\phi-\phi')\,. \tag{A.12}$$

The orthonormality relation also holds for the spherical harmonics:

$$\int d(\cos)\, d\phi\; Y^\star_{lm}(\theta,\phi)\, Y_{l'm'}(\theta,\phi) = \delta_{ll'}\,\delta_{mm'}\,. \tag{A.13}$$

Peter-Weyl theorem for group SU(N) : In general, this is also true for gauge group SU(N). The irreducible representations in the notation of Young diagrams are identified by a partition and are denoted by

$$\{\nu\} \equiv \{\nu_1;\ldots;\nu_{N-1}\}\,, \text{where } \nu_1 \geq \cdots \geq \nu_{N-1}\,. \tag{A.14}$$

[3] Two groups G and G' are said to be isomorphic if there exists a one-to-one correspondence between their elements, which preserves the law of group multiplication. In other words, if $\mathscr{G}_i \in G$, $\mathscr{G}'_i \in G'$ and $\mathscr{G}_1\mathscr{G}_2 = \mathscr{G}_3 \in G$, then $g'_1 g'_2 = g'_3 \in G'$ and vice versa [108].

The numbers $\{\nu\}$ are integer, and it is convenient to define the number

$$n = \sum_{i=1}^{N-1} \nu_i \,. \tag{A.15}$$

Elements of the group manifold can be conveniently parameterized by

$$\mathcal{G} = \exp\left[i \sum_{j=1}^{N^2-1} \hat{\tau}_j \phi_j / 2 \right] , \tag{A.16}$$

where $\hat{\tau}_1, \ldots, \hat{\tau}_{N^2-1}$ denote the group generators in the fundamental representation. A group element $\mathcal{G}$ in the irreducible representation, characterized by index $\{\nu\}$, is given by a matrix

$$D^{\{\nu\}}_{ab}(\mathcal{G}) \,, \tag{A.17}$$

where a, b are the matrix indices running from 1 to the dimension $|\nu|$ of the irreducible representation.

In order to compute the transition amplitude of the electric Hamiltonian, one can use the following corollary of the Peter-Weyl theorem. Let $\hat{C}$ denote the quadratic Casimir operator,

$$\hat{C} = \sum_{j=1}^{N^2-1} \hat{\tau}_j^2 \,. \tag{A.18}$$

Let C_ν denote the eigenvalue of $\hat{C}$ in irreducible representation $\{\nu\}$. Then as a corollary of the Peter-Weyl theorem, one can express a matrix element of an operator function $f(\hat{C})$ by

$$\begin{aligned}
&\langle \mathcal{G} | f(\hat{C}) | \mathcal{G}' \rangle = \\
&\sum_{\{\nu\}} \sum_{a,b=1}^{|\nu|} \sqrt{|\nu|}\, D^{\{\nu\}}_{ab}(\mathcal{G}^{-1})\, f(C_\nu)\, \sqrt{|\nu|}\, D^{\{\nu\}}_{ba}(\mathcal{G}') = \\
&\sum_{\nu} |\nu|\, f(C_\nu)\, Tr[D^{\{\nu\}}(\mathcal{G}^{-1}\mathcal{G}')] = \\
&\sum_{\nu} |\nu|\, f(C_\nu)\, \chi^{\{\nu\}}(\mathcal{G}^{-1}\mathcal{G}') \,.
\end{aligned} \tag{A.19}$$

The sum over $\{\nu\}$ runs over all partitions $\{\nu\} \equiv \{\nu_1; \ldots; \nu_{N-1}\}$ with $\nu_1 \geq \cdots \geq \nu_{N-1}$ and

$$\chi^{\{\nu\}}(\mathcal{G}) = Tr[D^{\{\nu\}}(\mathcal{G})] \tag{A.20}$$

denotes the group character. The Eq.(A.19) can be used to compute the transition amplitude under evolution of a Hamiltonian in the SU(N) gauge theory.

Appendix B

Numerical Algorithms of LGT

In general, the algorithms used in lattice gauge theory (LGT) simulations are classified into two main categories; deterministic and stochastic [160]. Both algorithms are suitable for problems in general forms and do not depend on structures and details of systems under consideration. In the case of stochastic algorithms, the usual strategy is to apply the Monte Carlo technique, while in deterministic methods people often employ the microcanonical algorithm [160, 161, 162]. In the microcanonical algorithm (which is also called the molecular dynamics method), the temperature changes during the updating of a system, but its total energy remains constant. On the other side, the energy of the system varies in the Monte Carlo algorithm, while its temperature is fixed. The Monte Carlo algorithms stochastically move through configuration space, while the microcanonical algorithm moves deterministically. Even to have more efficiency, one can combine both methods together in such a way that via the Monte Carlo procedure system tends to an equilibrium state at a special temperature, thereafter one tries to employ microcanonical algorithm to evolve system, in order to measure physical observables [160, 163]. Below, we briefly demonstrate both methods.

B.0.3 The Monte Carlo algorithm

The main hypothesis of the Lagrangian LGT generally is that the physical observables can be evaluated via

$$< \hat{O} > = \frac{1}{\mathcal{Z}} \int [d\phi]\, \hat{O}[\phi]\, e^{-S[\phi]}\,,$$
$$\mathcal{Z} = \int [d\phi]\, e^{-S[\phi]} \quad , \quad S[\phi] = \beta_0 V[\phi]\,, \tag{B.1}$$

where β_0 in the action $S[\phi]$ is the bare coupling constant of gauge theory, $\mathcal{Z}$ is the partition function of field theory, and $[\phi]$ denotes gauge and fermionic fields. This is, indeed, equivalent to the formulation of a canonical ensemble in classical statistical mechanics. The standard way to determine the expectation value in Eq.(B.1), is to use the Monte Carlo method.

During the Monte Carlo process in the LGT simulations, the values of all lattice links are updated through a random procedure, until they produce physical and meaningful field configurations. In fact, this process constructs a set of configurations ϕ through a Morkov chain. In this case when a system arrives in a statistical equilibrium state, then the probability of finding each configuration in the Markov chain is proportional to the Boltzmann weight factor

$$P_B(\phi) \equiv \exp\left[-S(\phi)\right] , \tag{B.2}$$

where $S(\phi)$ is the action of the LGT.

In order that the system attains the statistical equilibrium, the probability of changing a configuration ϕ into a new ϕ' is equivalent to the probability of converting ϕ' back to ϕ. This is called the "*detailed balance*" [2], which should be the case in each step of the Monte Carlo procedure. It is mathematically characterized by

$$P(\phi)\, T(\phi \to \phi') \;=\; P(\phi')\, T(\phi' \to \phi) . \tag{B.3}$$

The factor $T(\phi \to \phi')$ specifies the transition probability from ϕ to ϕ', which is defined by

$$T(\phi \to \phi') = min\left\{1, \frac{P(\phi')}{P(\phi)}\right\} \equiv min\left\{1, \exp\left[-\Delta S\right]\right\} . \tag{B.4}$$

Therefore, in order to update the system from a configuration ϕ into another configuration ϕ', first one computes the change in action as

$$\Delta S \;= S(\phi') - S(\phi) . \tag{B.5}$$

Then, if $\Delta S \;\leq\; 0$, the change is accepted and ϕ is replaced by ϕ'. Otherwise, if $\Delta S \;>\; 0$, the new configuration is accepted with the probability $\exp[-\Delta S]$. One can do this by generating a psudo-random number r in the interval (0, 1] with a uniform distribution. Now, if $\exp[-\Delta S] > r$, then ϕ' is accepted as a new configuration, otherwise it is rejected and the old configuration ϕ is conserved. Finally, one obtains a set of equilibrium configurations allowing one to measure the partition function and expectation values of observables. This procedure of constructing a sequence of system configurations is known as the Metropolis algorithm [115], which we use it in the Monte Carlo method with importance sampling to evaluate ratios of path integrals.

B.0.4 The microcanonical algorithm

One can formulate the Euclidean LGT in terms of microcanonical ensemble approach in statistical mechanics [162]. For this purpose, one can involve the canonical momentum variables Π in the Eq.(B.1) without impressing the expectation value of the observable $\hat{O}[\phi]$ as a function of ϕ. In fact, by adding these degrees of freedom, the configuration space is enlarged without changing the physics of the problem in question. Therefore, one can write [162]

$$< \hat{O} > = \frac{1}{\mathcal{Z}} \int [d\phi] \int [d\Pi]\, \hat{O}[\phi]\, e^{-\beta_0 \left(V[\phi]+K[\Pi]\right)} ,$$
$$\mathcal{Z} = \int [d\phi] \int [d\Pi]\, e^{-\beta_0 \left(V[\phi]+K[\Pi]\right)} , \tag{B.6}$$

where $K[\Pi]$ (i.e. the kinetic energy), is a functional of the canonical momentum Π, and $V[\phi]$ plays the role of potential energy. This is still a canonical formulation of LGT.

On the other hand, in a microcanonical ensemble, the total energy of the system in Eq.(B.6) is conserved. Thus, by considering the Hamiltonian $H(\phi, \Pi) = V[\phi] + K[\Pi]$, the dynamics of such a closed system is governed by Hamilton's equations.

$$\dot{\Pi} = -\frac{\partial V}{\partial \phi} \quad , \quad \dot{\phi} = \frac{\partial K}{\partial \Pi} . \tag{B.7}$$

The solution of this equation is a trajectory in the 2N-dimensional phase space $\{\phi, \Pi\}$. Along that trajectory, one can compute the expectation value of any observable $\hat{O}(\phi, \Pi)$, given by [162]

$$< \hat{O} > = \lim_{t \to \infty} \frac{1}{t} \int_0^t dt'\, \hat{O}[\phi(t'), \Pi(t')] , \tag{B.8}$$

where $t \to \infty$ stands for the thermodynamic limit.

In the case of U(1) LGT, Callaway et al. [162] computed the average kinetic energy $\langle K \rangle$ as well as the average action $\langle S \rangle = \beta_0 \langle V \rangle$ from the microcanonical approach. For example, for the kinetic energy they obtained

$$\langle K \rangle = \frac{N_{\text{indep}}}{2\beta_0} , \tag{B.9}$$

where N_{indep} denotes on the number of linearly independent variables among the N_{link} gauge field variables. Due to the local gauge symmetry in the theory, N_{indep} is lower than N_{link} [162, 163]. In the case of a large d-dimensional lattice, when the number of link variables goes to infinity (i.e. the thermodynamic limit), then the number of independent variables is given by [162, 163]

$$N_{\text{indep}} = \left[\frac{d-1}{d}\right] N_{\text{link}} = (d-1) N_{\text{site}}^4 , \tag{B.10}$$

where N_{site} states the number of lattice sites in each direction.

B.0.5 Updating a lattice configuration

The microcanonical technique is mostly used for the fermion-gauge-scalar models where a huge CPU time is required for constructing lattice configurations, especially due to the presence of fermions on lattice sites. However, in our simulations we only consider a pure gauge theory, hence, a Metropolis algorithm is efficient enough for our numerical computations.

Now, having Metropolis algorithm at hand, we want to construct an ensemble of equilibrium gauge field configurations. All lattice links require identical numerical calculations. But, the problem is that to hold the detailed balance procedure in the Metropolis process, in the case of LGT, one cannot update the adjacent interacting gauge links at the same time because of their mutual interactions. However, in the latticized gauge action one can simultaneously update at least a half of link variables in each direction and preserve the detailed balance. We illustrate this point in two schemes in the following sections.

Here we talk on U(1) LGT, which is the discretized version of quantum electrodynamics. As discussed in Chapter 1, in the compact model of U(1) LGT, the electric field on a link is represented by an angle θ, which is an element of U(1) gauge group. Each link settles along one of the directions in the Cartesian reference frame, and connects adjacent lattice sites. We have used the standard form of the Wilson action, which consists of 1×1 Wilson loops (plaquettes). One can also use the improved forms of the Wilson action, containing larger Wilson loops, in order to economize numerical simulations. This is usually interesting in the lattice QCD simulations in (3+1)-dimension, particularly for working on large lattice sizes. However, this topic is out of scope of our work on $U(1)_{2+1}$ lattice gauge group, and we employ the standard Wilson action [1] for a pure gauge theory.

B.0.6 The even-odd and the linear preconditionings

In this section, we illustrate two algorithms, which enable us to work with lattices in the Cartesian coordinates. They are efficient methods such that allow us to enormously minimize the number of serial calculations needed to perform a Monte Carlo[163, 164] or molecular dynamics updating[119] over all the links of the lattice.

Checkerboard pattern

Here we talk on the even-odd preconditioning [119] method of lattice in (2+1)-D, which is also called the checkerboard masking [164]. Consider the link connecting two lattice sites n and $n + a\hat{\mu}$, where μ generally is one of the Cartesian unit vectors $\hat{x}$, $\hat{y}$, $\hat{t}$, and a points on the lattice spacing. In the case of (3+1)-dimension the direction $\hat{z}$ also joins to these components. As one observes from Fig.[B.1], each plaquette makes a staple containing three links in the plane $\mu - \nu$ and attached to the considered link $U_\mu(n) = e^{i\theta_\mu(n)}$. Actually in each plane $\mu - \nu$, there are two staples around the link in question. This means that in (2+1) Cartesian dimensions, each link is associated with at most four staples. Fig.[B.1] shows such a situation for the temporal link $U_t(n)$ touching with four staples. However, if one talk just about spatial staples, their maximum numbers are two. For example, let us take a look on

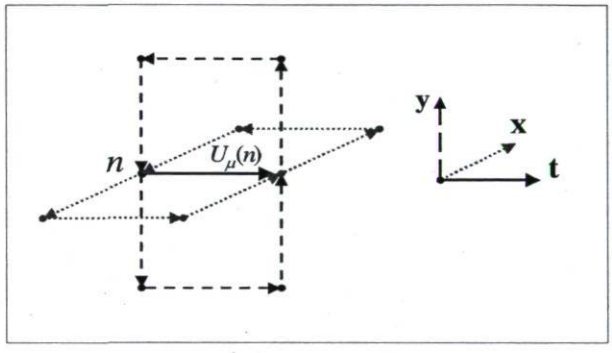

Figure B.1: Four staples around the link variable $U_\mu(n)$ out going from the site n [164]. Note that here $\mu \equiv t$.

all the links in the plane $\mu - \nu$, with the orientation μ. For a moment let us concentrate only on those links which can be updated at the same time without altering the other links. For instance, the link variables in the μ direction, which can be simultaneously updated, are labled by $U_\mu(n)$, $U_\mu(n + a\hat{\mu})$, $U_\mu(n + 2a\hat{\mu})$ and so forth. It is clear from Fig.[B.2] (left panel) that one can imagine a checkerboard, organized by those links. Furthermore, one can observe that each updating link does not take place in the staples around the other updating links. Consequently, a half of the links along the μ axis in the plane $\mu - \nu$ can be updated at the same time [164]. This is the case for every Cartesian orientation.

Linear pattern

Another possibility to renew the lattice links is to use a linear architecture [164] which is equivalent to the previous one. As Fig.[B.2] (right panel) shows, all links are divided into two colors in a linear fashion in this scheme. By analogy to the checkerboard preconditioning,

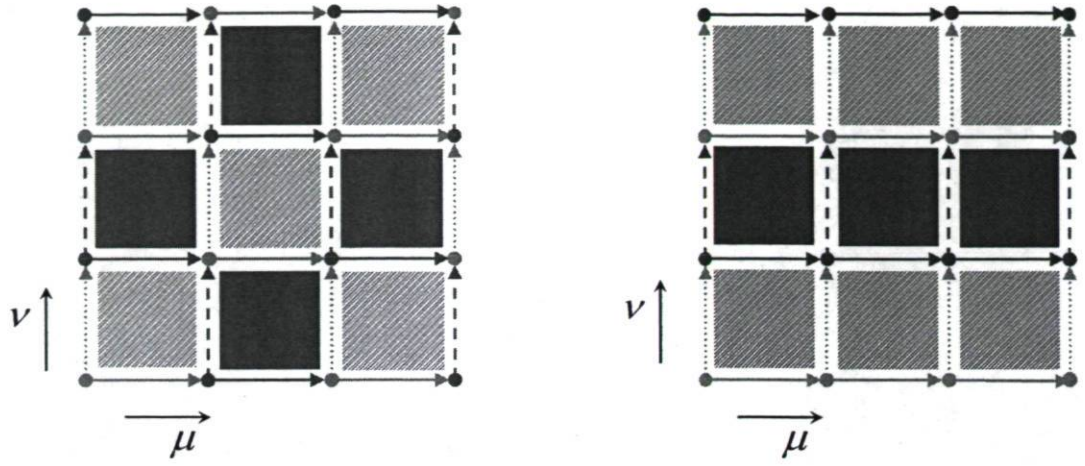

Figure B.2: Left panel: The checkerboard architecture of lattice links. In each direction, the links around plaquettes of the same color are updated simultaneously without effecting the other links. Right panel: The linear scheme of link variables in the plane $\mu - \nu$. The links with the same color in each line can be updated at the same time during a Monte Carlo procedure, without interfering with the other links in this plane.

here also all the links with the same color in a given orientation, e.g. μ, can be updated simultaneously in a linear pattern. The reason of such equal renewing is that each updating link $U_\mu(n)$ does not have any contribution in the staples involving the other links along the considered line. Therefore, likewise in the checkerboard model, the links $U_\mu(n)$, $U_\mu(n + a\hat{\mu})$, $U_\mu(n + 2a\hat{\mu}), \ldots$ are updated at the same time by applying a Metropolis approach for each link. In other words, instead of considering the whole lattice plaquettes in the Wilson action (needed for the Monte Carlo procedure) here one works with elementary plaquettes connected to each link. Furthermore, we use them as the Wilson action in the Metropolis criterion in order to update that link. Since the links are divided into two colors, hence the above procedure must be done in two steps; one for each color. This is true for both checkerboard and linear methods. These techniques are the conventional methods in LGT simulations with the standard, as well as improved actions, and also they can be used for both serial and parallel programming in LGT simulations [164].

Appendix C

Billiard Mapping

According to Ref. [165], let us consider an arbitrary 2D planar billiard system including a point particle, which moves freely inside billiard domain Ω. (see Fig.[C.1]). Starting from an initial position, the point particle successively collides with the boundary of system and constructs a zig-zag trajectory within the billiard zone. In our simulations, the main task is to construct such trajectories and compute the length of those zig-zag paths.

For the sake of simplicity one can work in a polar reference frame. Hence, the perimeter of billiard is described by the function $\Gamma(\theta)$, and the location of particle on the billiard boundary is characterized by the polar angle θ and the radial distance $r(\theta)$ (see Fig.[C.1]). Having a given position of particle (say $A(r_i, \theta_i)$) at hand, one can find its next location on the boundary, e.g. the next collision point $B(r_{i+1}, \theta_{i+1})$. To this end, let us parameterize the trajectory part AB in terms of the polar coordinates. Regarding Fig.[C.1], this segment is given by

$$\rho(\theta) = r(\theta)\frac{\sin(\beta_i - \theta_i)}{\sin(\beta_i - \theta)}\,, \tag{C.1}$$

where β_i determines the tangent of the trajectory AB. Now the point is that the subsequent destination B of the moving particle is, in fact, the intersection of the line $\rho(\theta)$ and the boundary $\Gamma(\theta)$, given by

$$\rho(\theta) - \Gamma(\theta) \equiv r(\theta)\frac{\sin(\beta_i - \theta_i)}{\sin(\beta_i - \theta)} - \Gamma(\theta) = 0\,. \tag{C.2}$$

In practice, and to ignore any indefinite result, one considers

$$\chi(\theta) \;=\; r(\theta)\,\sin(\beta_i - \theta_i) - \Gamma(\theta)\,\sin(\beta_i - \theta)\,, \tag{C.3}$$

as the utility to find the solutions of Eq.(C.2). In the case of billiard boundaries described by differenciable functions $\Gamma(\theta)$, a commonly applied method to find the zeros of such functions are the Newton-Raphson technique [166].

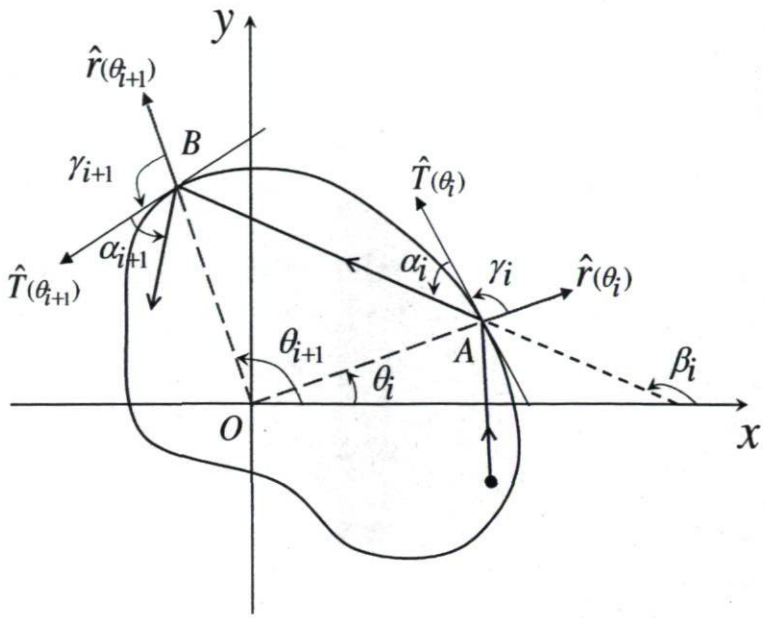

Figure C.1: General scheme of dynamical billiard. The line passing the collision points A and B is described by $\rho(\theta)$, and the radial distances OA and OB are parameterized by $r(\theta)$.

No matter what numerical technique we use, the solution of Eq.(C.3) obviously is the angle θ_{i+1} related to the contact point B. Now, the next step is to determine the angle α_{i+1}, which identifies the angle between the normal vector to the boundary at A and the trajectory segment connecting A and B. From Fig.[C.1] one can conclude that the angle β at the points A and B is given by

$$\begin{aligned} \beta_i &= \theta_i + (\gamma_i + \alpha_i)\,, \\ \beta_i &= \theta_{i+1} + (\gamma_{i+1} - \alpha_{i+1})\,, \end{aligned} \tag{C.4}$$

where

$$\alpha_i \in [0, \pi]\,,\ \beta_i \in [0, 2\pi]\ \text{, and } \gamma(\theta) = \tan^{-1}\left[\frac{\Gamma(\theta)}{\partial_\theta \Gamma(\theta)}\right]. \tag{C.5}$$

In consequence, the angle α_{i+1} is extracted from Eq.(C.4) as

$$\alpha_{i+1} = (\theta_{i+1} - \theta_i) + (\alpha_{i+1} - \alpha_i) - \gamma(\theta_i)\,. \tag{C.6}$$

Through this procedure, when the initial position $P_0(\theta_0, \alpha_0)$ of the billiard ball is available, one can determine its subsequent bouncing points on the boundary, and hereby characterize the whole zig-zag trajectory within the billiard area.

Bibliography

[1] K.G. Wilson, *Phys. Rev. D* **10**, 2445 (1974).

[2] H. J. Rothe, *Lattice Gauge Theories, An Introduction*, World Scientific, 3rd edition (2006).

[3] T. DeGrand and C. DeTar, *Lattice Methods for Quantum Chromodynamics*, World Scientific (2006).

[4] J. Kogut and L. Susskind, *Phys. Rev. D* **11**, 395 (1975).

[5] I. Montvay and G. Münster, *Quantum Fields on Lattice*, Cambrige University Press (1994).

[6] H. Kröger, *Proceedings of the Fourth International Conference on Dynamical Systems and Differential Equations* Wilmington, USA (2002).

[7] K.G. Wilson, *Rev. Mod. Phys.* **47**, 773 (1975).

[8] J. Schwinger, *Phys. Rev.* **125**, 397 (1962).

[9] M. E. Peskin and D.V. Schroeder, *An Introduction to Quantum Field Theory*, Westview press (1995).

[10] H. Jirari, H. Kröger, X.Q. Luo and K.J.M. Moriarty, *Phys. Lett. A* **258**, 6 (1999).

[11] H. Jirari, H. Kröger, C.Q. Huang, J.Q. Jiang, X. Q. Luo and K.J.M. Moriarty, *Nucl. Phys. B (Proc. Suppl.)* **83-84**, 953 (2000).

[12] X.Q. Luo, C.Q. Huang, I.Q. Jiang, H. Jirari, H. Kröger and K.J.M. Moriarty *Nucl. Phys. Proc. Suppl.* **83**, 810 (2000).

[13] X.Q. Luo, H. Xu, J.C. Jiang, Y.L. Wang, D. Chang, Y. Lin and H. Kröger, *Commun. Theor. Phys.(China)* **36**, 7 (2001).

[14] X.Q. Luo, C.Q. Huang, I.Q. Jiang, H. Jirari, H. Kröger and K.J.M. Moriarty *Physica A* **281**, 201 (2000).

[15] X.Q. Luo, J.J. Liu, C.Q. Huang, J.C. Jiang and H. Kröger, *Commun. Theor. Phys.(China)* **38**, 561 (2002).

[16] X.Q. Luo, X.N. Cheng and H. Kröger, *Commun. Theor. Phys.(India), Fundamental Physics 3,* 335 (2007).

[17] Y.Y. Li, X.Q. Luo and H. Kröger, *Sci. China* **G49**, 60 (2006).

[18] H. Kröger, X.Q. Luo and K.J.M. Moriarty, *Math. Comput. Simul.* **62**, 377 (2003).

[19] H. Kröger, X.Q. Luo and K.J.M. Moriarty *Nucl. Phys. Proc. Suppl.* **119**, 508 (2003).

[20] C.Q. Huang, H. Kröger, X. Q. Luo and K.J.M. Moriarty, *Phys. Lett. A* **299**, 483 (2002).

[21] X.Q. Luo, H. Jirari, H. Kröger and K.J.M. Moriarty, *Proceedings of the International Workshop on Nonperturbative Methods and Lattice QCD, World Scientific* 100-111 (2001).

[22] F. Paradis, H. Kröger, X.Q. Luo and K.J.M. Moriarty *Mod. Phys. Lett. A* **22**, 565 (2007).

[23] M. Creutz, *Quarks, Gluons and Lattices*, Cambridge University Press (1983).

[24] M. Creutz, L. Jacobs and C. Rebbi, *Phys. Rept.* **95**, 201 (1983).

[25] K. Nakamura, *Quantum Chaos and Quantum Dots*, Cambridge University Press (2004).

[26] M.V. Berry, *Eur. J. Phys.* **2**, 91 (1981).

[27] Ya.G. Sinai, *Sov. Math. Dokl.* **4**, 1818 (1963).

[28] Ya.G. Sinai, *Russ. Math. Surveys* **35**, 137 (1970).

[29] L.A. Bunimovich, *Funct. Anal. Appl.* **8**, 73 (1974).

[30] T. Tasnadi, *J. Math. Phys.* **39**, 3783 (1998).

[31] A. Krámli, N. Simányi and D. Szász, *Commun. Math. Phys.* **125**, 439 (1989).

[32] B. Gutkin, U. Smilansky and E. Gutkin, *Comm. Math. Phys.* **208**, 65 (1999).

[33] M.F. Andersen, A. Kaplan, N. Friedman and N. Davidson, *J. Phys. B* **35**, 2183 (2002).

[34] H.E. Lehtihet and B.N. Miller, *Physica D* **20**, 93 (1986).

[35] A. Hayli and A. Vidovic, *Lect. Notes Phys.* **430**, 85 (1994).

[36] H.R. Dullin, *Nonliniarity* **11**, 151 (1998).

[37] H.J. Korsch and J. Lang, *J. Phys. A: Math. Gen.* **24**, 45 (1991).

[38] H. Wallis, J. Dalibard and C. Cohen-Tannoudji, *Appl. Phys. B* **54**, 407 (1992).

[39] S. Feldt and J.S. Olafsen, *Phys. Rev. Lett.* **94**, 224102 (2005).

[40] T. Tasnadi, *J. Math. Phys.* **37**, 5577 (1996).

[41] T. Tasnadi, *Comm. Math. Phys.* **187**, 597 (1997).

[42] N. Berglund and H. Kunz, *J. Stat. Phys.* **83**, N.1/2, 81 (1996).

[43] M. Robnik and M.V. Berry, *J. Phys. A: Math. Gen.* **18**, 1361 (1985).

[44] K. Nakamura and T. Harayama, *Quantum Chaos*, Cambridge University Press (1993).

[45] R. Blümel and W.P. Reinhrdt, *Chaos in Atomic Physics*, Cambridge University Press, Cambridge (1997).

[46] H.J. Stöckmann, *Quantum Chaos*, Cambridge Univ. Press, Cambridge (1999).

[47] F. Haake, *Quantum Signatures of Chaos*, Springer, Berlin (2001).

[48] F. Miao, S. Wijeratne, Y. Zhang, U. Coskun, W. Bao and C.N. Lau, *Science* **317**, 1530 (2007).

[49] V. Milner, J.L. Hanssen, W.C. Campbell and M.G. Raizen, *Phys. Rev. Lett.* **86**, 1514 (2001).

[50] N. Friedman, A. Kaplan, D. Carasso and N. Davidson, *Phys. Rev. Lett.* **86**, 1518 (2001).

[51] S. Sridhar, *Phys. Rev. Lett.* **67**, 785 (1991).

[52] S. Sridhar and W.T. Lu, *J. Stat. Phys.* **108**, 755 (2002).

[53] U. Stoffregen, J. Stein, H.J. Stöckmann, M. Kus and F. Haake, *Phys. Rev. Lett.* **74**, 2666 (1995).

[54] J. Stein, H.J. Stöckmann and U. Stoffregen, *Phys. Rev. Lett.* **75**, 53 (1995).

[55] U. Dörr, H.J. Stöckmann, M. Barth and U. Kuhl, *Phys. Rev. Lett.* **80**, 1030 (1998).

[56] H.J. Stöckmann and J. Stein, *Phys. Rev. Lett.* **64**, 2215 (1990).

[57] C. Dembrowski, H.D. Gräf, A. Heine, R. Hofferbert, H. Rehfeld and A. Richter, *Phys. Rev. Lett.* **84**, 867 (2000).

[58] C. Dembrowski, H.D. Gräf, H.L. Harney, A. Heine, W.D. Heiss, H. Rehfeld and A. Richter, *Phys. Rev. Lett.* **86**, 787 (2001).

[59] C. Dembrowski, H.D. Gräf, A. Heine, T. Hesse, H. Rehfeld and A. Richter, *Phys. Rev. Lett.* **86**, 3284 (2001).

[60] C. Dembrowski, B. Dietz, H.D. Gräf, H.L. Harney, A. Heine, W.D. Heiss and A. Richter, *Phys. Rev. Lett.* **90**, 034101 (2003).

[61] S. Sridhar and W.T. Lu, *J. Stat. Phys.* **108**, 755 (2002).

[62] M.L. Mehta, *Random Matrices and the Statistical Theory of Energy Levels*, Academic Press, New York (1991).

[63] O. Bohigas and M.J. Giannoni, *Lect. Notes Phys.* **209**, 1 (1983).

[64] O. Bohigas, M.J. Giannoni and C. Schmit, *Phys. Rev. Lett.* **52**, 1 (1984).

[65] R.U. Haq, A. Pandey and O. Bohigas, *Phys. Rev. Lett.* **48**, 1086 (1982).

[66] D. Wintgen and H. Friedrich, *Phys. Rev. A* **35**, 1464 (1987).

[67] D. Engel, J. Main and G. Wunner, *J. Phys. A: Math. Gen.* **31**, 6965 (1998).

[68] D. Delande and J.C. Gay, *Phys. Rep.* **183**, 37 (1989).

[69] K. Karremans, W. Vassen and W. Hogervorst, *Phys. Rev. Lett.* **81**, 4843 (1998).

[70] N. Argaman, F.M. Dittes, E. Doron, J.P. Keating, A.Y. Kitaev, M. Sieber and U. Smilansky, *Phys. Rev. Lett.* **71**, 4326 (1993).

[71] J.F. Laprise, O. Blondeau-Fournier, J. Kröger, H. Kröger, P.Y. St.-Louis, L.J. Dubé, E. Endress, A. Burra, R. Zomorrodi, G. Melkonyan and K.J.M. Moriarty, *Phys. Lett. A* **372**, 4574 (2008).

[72] J.F. Laprise, A. Hosseinizadeh, O. Blondeau-Fournier, J. Kröger, H. Kröger, P.Y. St.-Louis, L.J. Dubé and R. Zomorrodi, *Submitted to New J. Phys.* (2010).

[73] M. Robnik, *J. Phys. A: Math. Gen.* **16**, 3971 (1983).

[74] M. Wojtkowski, *Comm. Math. Phys.* **105**, 391 (1986).

[75] E.B. Gregory, S.H. Guo, H. Kröger and X.Q. Luo, *Phys. Rev. D* **62**, 054508 (2000).

[76] J. Kogut, *Rev. Mod. Phys.* **55**, 775 (1983).

[77] X.Q. Luo, S.H. Guo, H. Kröger and D. Schütte, *Phys. Rev. D* **59**, 034503 (1999).

[78] M. Creutz, *Phys. Rev. D* **15**, 1128 (1977).

[79] S.D. Drell, H.R. Quinn, B. Svetitsky and M. Weinstein *Phys. Rev. D* **619**, 19 (1979).

[80] D. Horn and M. Weinstein, *Phys. Rev. D* **30**, 1256 (1984).

[81] D. Horn, M. Karliner and M. Weinstein, *Phys. Rev. D* **31**, 2589 (1985).

[82] C.P. van den Doel and D. Horn, *Phys. Rev. D* **33**, 3011 (1986).

[83] C.P. van den Doel and D. Horn, *Phys. Rev. D* **35**, 2824 (1987).

[84] C.J. Hamer, R.J. Bursill and M. Samaras, *Phys. Rev. D* **62**, 054511 (2000).

[85] C.J. Hamer, *Phys. Lett. B* **224**, 339 (1989).

[86] C.J. Hamer, J. Oitmaa and Z. Weihong, *Phys. Rev. D* **45**, 4652 (1992).

[87] C.J. Hamer, M. Sheppeard, Z. Weihong and D. Schütte, *Phys. Rev. D* **54**, 2395 (1996).

[88] D. Schütte, Z. Weihong and C.J. Hamer, *Phys. Rev. D* **55**, 2974 (1997).

[89] A. Wichmann, D. Schütte, C.M. Bernard and V. Wethkamp, *Phys. Rev. D* **65**, 094511 (2002).

[90] Q. Chen, X.Q. Luo, S. Guo and X. Fang, *Phys. Lett. B* **348**, 560 (1995).

[91] S.H. Guo, Q.Z. Chen and L. Li, *Phys. Rev. D* **49**, 507 (1994).

[92] C.J. Morningstar and M. Peardon, *Phys. Rev. D* **60**, 034509 (1999).

[93] S.A. Chin, C. Long and D. Robson, *Phys. Rev. D* **37**, 3001 (1988).

[94] S.A. Chin, C. Long and D. Robson, *Phys. Rev. D* **37**, 3006 (1988).

[95] T. Banks, R. Myerson and J. Kogut, *Nucl. Phys. B*, **129**, 493 (1977).

[96] S.D. Drell, H.R. Quinn, B. Svetitsky and M. Weinstein, *Phys. Rev. D* **19**, 619 (1979).

[97] G. Bhanot and M. Creutz, *Phys. Rev. D* **21**, 2892 (1980).

[98] V.G. Bornyakov, V.K. Mitrjushkin and M. Müller-Preussker, *Nucl. Phys. B (Proc. Suppl.)* **30**, 578 (1993).

[99] M. Creutz, *Phys. Rev. D* **23**, 1815 (1981).

[100] A.M. Polyakov, *Nucl. Phys. B*, **120**, 429 (1977).

[101] M. Göpfert and G. Mack, *Commun. Math. Phys.*, **82**, 545 (1982).

[102] L. Gross, *Commun. Math. Phys.*, **92**, 137 (1983).

[103] A.C. Irving, J.F. Owens and C.J. Hamer, *Phys. Rev. D* **28**, 2059 (1983).

[104] A.H. Guth, *Phys. Rev. D* **21**, 2291 (1980).

[105] C.J. Morningstar, *Phys. Rev. D* **46**, 824 (1992).

[106] H.W. Lin and S.D. Cohen, *Proceeding for 4th International Workshop On Numerical Analysis And Lattice QCD* New Haven, USA (2007).

[107] G. Burgio, R. De Pietri, H.A. Morales-Técotl, L.F. Urrutia and J.D. Vergara, *Nucl. Phys. B* **566**, 547 (2000).

[108] Wu-Ki Tung, *Group Theory in Physics*, World Scintific (1985).

[109] J. Kogut, *Rev. Mod. Phys.* **51**, 659 (1979).

[110] S. Elitzur, *Phys. Rev. D* **12**, 3978 (1975).

[111] F. Paradis, H. Kröger, X.Q. Luo and K.J.M. Moriarty, *Phys. Rev. D* **71**, 077502 (2005).

[112] D.P. Landau and K. Binder, *A Guide to Monte Carlo Simulations in Statistical Physics*, Cambrige University Press (2005).

[113] S. Boyaval, C. Le Bris, Y. Maday, N.C. Nguyen and A.T. Patera, *Comput. Methods Appl. Mech. Engrg.* (2009).

[114] L.P. Kadanoff, *Physics* **2**, 263 (1966).

[115] N. Metropolis, A.W. Rosenbluth, M.N. Rosenbluth, A.N. Teller and E. Teller, *J. Chem. Phys.* **21**, 1087 (1953).

[116] A. Hosseinizadeh, G. Melkonyan, J. Kröger, H. Kröger and J.F. Laprise *Submitted to Phys. Rev. D* (2010).

[117] H. Kröger, A. Hosseinizadeh, J.F. Laprise and J. Kröger, *The XXVI International Symposium on Lattice Field Theory*, Virginia, USA (2008).

[118] K.G. Wilson and J. Kogut, *Phys. Rep. C* **12**, 75 (1974).

[119] X.Q. Luo, X.N. Cheng and H. Kröger, *Commun. Theor. Phys.* **41**, 509 (2004).

[120] P. Gaspard, *Chaos, Scattering and Statistical Mechanics*, Cambridge University Press, Cambridge (1998).

[121] A.Y. Abul-Magd and M.H. Simbel *Phys. Rev. E* **60**, 5371 (1999).

[122] T.A. Brody, J. Flores, J.B. French, P.A. Mello, A. Pandey and S.S.M. Wong, *Rev. Mod. Phys.* **53**, 385 (1981).

[123] O. Bohigas and M.J. Giannoni, *Ann. of Phys.* **89**, 393 (1975).

[124] M.V. Berry, *Proc. R. Soc. London, Ser. A* **400**, 229 (1985).

[125] M.V. Berry, *Proc. R. Soc. London, Ser. A* **413**, 183 (1987).

[126] M. Sieber and K. Richter, *Physica Scripta* **T90**, 128 (2001).

[127] S. Müller, S. Heusler, P. Braun, F. Haake and A. Altland, *Phys. Rev. Lett.* **93**, 014103 (2004).

[128] J.P. Keating and S. Müller, *Proc. R. Soc. London, Ser. A* **463**, 3241 (2007).

[129] J.M.G. Gómez, R.A. Molina, A. Relano and J. Retamosa, *Phys. Rev. E* **66**, 036209 (2002).

[130] A. Pandey and M.L. Mehta, *Commun. Math. Phys.* **87**, 449 (1983).

[131] D. Poulin, *A Rough Guide to Quantum Chaos*, University of Waterloo (2002).

[132] N. Chernov and R. Markarian, *Chaotic Billiards*, Mathematical Surveys and Monographs, Amer. Math. Soc., Providence, RI , Vol. **127** (2006).

[133] J.P. Bouchaud and A. Georges, *Phys. Rep.* **195**, 127 (1990).

[134] E.R. Weeks and H.L. Swinney, *Phys. Rev. E* **57**, 4915 (1997).

[135] D. Sornette, *Critical Phenomena in Natural Sciences*, Springer (2006).

[136] M.H. DeGroot, *Probability and Statistics*, Addison-Wesley, Massachusetts (1975).

[137] N.G. Van Kampen, *Stochastic Processes in Physics and Chemistry*, Elsewier, The Netherlands (2007).

[138] L.A. Bunimovich and Ya.G. Sinai, *Commun. Math. Phys.* **78**, 479 (1981).

[139] L.A. Bunimovich, Ya.G. Sinai and N.I. Chernov, *Russ. Math. Surveys.* **46**, 47 (1991).

[140] D. Szász and T. Varjú, *J. Stat. Phys.* **129**, 59 (2007).

[141] P. Bálint and S. Gouëzel, *Comm. Math. Phys.* **263**, 461 (2006).

[142] V.M. Alekseev and M.V. Yakobson, *Phys. Rep.* **75**, 290 (1981).

[143] G. Beneti, G. Casati and G. Strini, *Principles of Quantum Computation and Information*, World Scientific (2007).

[144] A. Hosseinizadeh, J.F. Laprise, J. Kröger, H. Kröger and R. Zomorrodi, *Fluctuation Statistics and Transport Properties of 2D Triangular Lorentz Gas: Finite versus Infinite Horizon (to be submitted to Phys. Rev. E).*

[145] A. Courcelle, H. Derrien, L.C. Leal and N.M. Larson, *American Nuclear Society, Proc. of Math and Comp.* (2005).

[146] T.H. Seligman, J.J.M. Verbaarschot and M.R. Zirnbauer, *Phys. Rev. Lett.* **53**, 215 (1984).

[147] P. Gaspard and F. Baras *Phys. Rev. E* **51**, 532 (1995).

[148] J.F. Laprise, A. Hosseinizadeh, J. Lamy-Poirier, J. Kröger, H. Kröger and R. Zomorrodi, *Phys. Lett. A* **374**, 2000 (2010).

[149] P. Gaspard and G. Nicolas, *Phys. Rev. Lett.* **65**, 1693 (1990).

[150] L.A. Bunimovich and Y.G. Sinai, *Commun. Math. Phys.* **78**, 247 (1980).

[151] J. Machta and R. Zwanzig, *Phys. Rev. Lett.* **50**, 1959 (1983).

[152] F. Borgonovi, G. Casati and B. Li, *Phys. Rev. Lett.* **77**, 4744 (1996).

[153] G.P. Morris and L. Rondoni, *J. Stat. Phys.* **75**, 553 (1994).

[154] J.R. Dorfman and P. Gaspard, *Phys. Rev. E* **51**, 28 (1995).

[155] P.M. Bleher, *J. Stat. Phys.* **66**, 315 (1992).

[156] B. Friedman and R.F. Martin, *Phys. Lett.* **105A**, 23 (1984).

[157] J.P. Bouchaud, P.L. Doussal *J. Stat. Phys.* **41**, 225 (1985).

[158] A. Zacherl, T. Geisel, J. Niewetberg, G. Radons, *Phys. Lett. A* **114**, 317 (1986).

[159] S. Sternberg, *Group Theory and Physics*, Cambridge University Press (1994).

[160] M. Creutz, *Phys. Rev. Lett.* **50**, 1411 (1983).

[161] M. Creutz, *Phys. Rev. Lett.* **69**, 1002 (1992).

[162] D.J.E. Callaway and A. Rahman, *Phys. Rev. Lett.* **49**, 613 (1982).

[163] C.F. Baillie, S.L. Johnson, L. Ortiz and G.S. Pawley, *Proceedings of the third conference on Hypercube concurrent computers and applications.*, USA, 1288 (1989).

[164] F.D.R. Bonnet, D.B. Leinweber and A.G. Williams, *J.Comput.Phys.* **1**, 170 (2001).

[165] K.H. Hoffmann, M. Schreiber, *Computational Statistical Physics: From Billiards to Monte Carlo*, Springer (2002).

[166] J.H. Pollard, *A Hnadbook of Numerical and Statistical techniques*, Cambridge University Press (1979).

Index